Numerical Analysis of Arrays of Wave Energy Converters

Aidan Bharath

University of Tasmania
National Centre for Maritime Engineering and Hydrodynamics

Submitted in fulfilment of the requirements for the degree of
Doctor of Philosophy

Australian Maritime College April 2018

Declaration

Declaration of Originality and Authority of Access

This thesis contains no material which has been accepted for a degree or diploma by the University or any other institution, except by way of background information and duly acknowledged in the thesis, and to the best of my knowledge and belief no material previously published or written by another person except where due acknowledgement is made in the text of the thesis, nor does the thesis contain any material that infringes copyright.

This thesis may be made available for loan and limited copying and communication in accordance with the Copyright Act 1968.

Aidan Bharath
April 2018

Statement of Published Work Contained in Thesis

The publishers of the papers comprising Chapters 2 and 5 and appendix 1 hold the copyright for that content, and access to the material should be sought from the respective journals and conference proceedings. The remaining non published content of the thesis, Chapter 3 and 4, are submitted and under review, and may be made available for loan and limited copying and communication in accordance with the Copyright Act 1968.

Statement of Co-Authorship

The following people and institutions contributed to the publication of work undertaken as part of this thesis:

- Aidan Bharath, University of Tasmania **(Candidate)**
- Assoc. Prof. Irene Penesis, University of Tasmania **(Author 1)**
- Dr Jean-Roch Nader, University of Tasmania **(Author 2)**
- Assoc. Prof. Gregor Macfarlane, University of Tasmania **(Author 3)**

Chapter 2 (Paper 2) **Nonlinear Hydrodynamic Effects on a Generic Spherical Wave Energy Converter** Candidate was the primary author and with Author 1, 2 and 3 assisting with refinement and presentation. Candidate: 75% , Author 1: 10% , Author 2: 10% , Author 3: 5%
Chapter 3 (Paper 3) **Numerical Investigation of Generic Submerged Spherical Wave Energy Converter Arrays. Part 1: The Diffraction Problem** Candidate was the primary author and with Author 1, 2 and 3 assisting with refinement and presentation. Candidate: 80% , Author 1: 5% , Author 2: 10% , Author 3: 5%
Chapter 4 (Paper 4) **Numerical Investigation of Generic Submerged Spherical Wave Energy Converter Arrays. Part 2: The Radiation Problem** Candidate was the primary author and with Author 1, 2 and 3 assisting with refinement and presentation. Candidate: 80% , Author 1: 5% , Author 2: 10% , Author 3: 5%
Chapter 5 (Paper 5) **Modelling of a Damped Generic Submerged Spherical Wave Energy Converter in Resonance** Candidate was the primary author and with Author 1, 2 and 3 assisting with refinement and presentation. Candidate: 80% , Author 1: 5% , Author 2: 10% , Author 3: 5%
Appendix 1 (Paper 1) **Non-Linear CFD Modelling of a Submerged Sphere Wave Energy Converter** Candidate was the primary author and with Author 1, 2 and 3 assisting with refinement and presentation. Candidate: 85% , Author 1: 5% , Author 2: 5% , Author 3: 5%

We undersigned agree with the above statements of the proportion of work undertaken for each of the published peer-reviewed manuscripts contributing to this thesis.

Signed:

Signature: ..... Date: Thursday 26th April, 2018

Associate Professor Irene Penesis

Principal Supervisor

National Centre for Maritime Engineering and Hydrodynamics, University of Tasmania

---

Signature: ..... Date: Thursday 26th April, 2018

Dr Jean-Roch Nader

Co-Supervisor

National Centre for Maritime Engineering and Hydrodynamics, University of Tasmania

---

Signature: ..... Date: Thursday 26th April, 2018

Associate Professor Gregor Macfarlane

Co-Supervisor

National Centre for Maritime Engineering and Hydrodynamics, University of Tasmania

---

Abstract

A wave energy converter (WEC) has the potential to become a viable technology for clean, renewable energy production. This technology may prove invaluable to meet the growing demands for electrical power and the apparent changing climate conditions. WEC designs and power output rely heavily on the sea conditions and bathymetry surrounding their deployment sites and require extensive testing prior to the deployment of a commercially operating device. With the challenges and high costs of prototype testing in wave tanks at model scale and in open ocean conditions, numerical studies have been employed extensively to study the performance and estimate potential power-take-off (PTO) capabilities of WECs. Much of the numerical work however, is based on linear wave theory which has the capability of validating the potential of a design and modelling it's performance in various sea states but lacks the capability to capture complex, nonlinear behaviour such as viscous, turbulent or wave breaking dynamics.

With model and full scale WECs being tested, there is now a growing need to understand their dynamics beyond the capabilities of linear modelling. It is necessary to understand their combined interaction when positioned in close proximity to each other, as the diffracted waves from one WEC to another can influence the hydrodynamic forces for better or worse and influence the overall power generated. This problem has largely been addressed using linear modelling techniques providing optimised array configurations for various WECs and sea conditions. These studies are however limited by the linear wave assumptions.

This work aims to fill this knowledge gap by applying fully nonlinear modelling techniques to assess the validity of linear modelling methods. In this sense the notion of superposition used in constructing linear models of WECs is held by modelling the diffraction and radiation problems separately. This method ensures no coupling between the nonlinear effects generated in each problem allowing for the detailed study of the nonlinearities caused solely from either the WECs presence in a wave field or its contribution to the wave field. This represents a novel approach to the problem of modelling a wave energy converter and offers a unique perspective into the dynamics of a WEC.

The method of applying computational fluid dynamics (CFD) to the diffraction and

radiation problems of WEC modelling offers the benefit of computational speed to simulations which are a major limiting factor in it's applications. In combination with linear modelling techniques, device performance can be predicted quickly across a wide range of conditions allowing further focussed studies to be carried out with CFD. The effects of high order waves, viscosity, turbulence and free surface interaction on the hydrodynamic coefficients near the WECs resonance are quantified. The same methods and principles are then applied to array configurations of WECs.

The method of superposition of the hydrodynamic diffraction and radiation components developed and applied here allows for detailed predictions of device performance and optimisation of any WEC type, and a means of analysing complex WEC dynamics efficiently through the reduction of long simulation times. By using a generic WEC device to study these hydrodynamic behaviours we have highlighted important factors that effect the performance of a WEC which are not captured by linear methods.

Table of Contents

List of Figures

List of Tables

Nomenclature

α	Volume Fraction
C_{FL}	Courant-Friedrichs-Lewi Number
d	Wave Energy Converter Diameter
Γ	Excitation Force Coefficient
η	Wave Amplitude
F	Real Total Hydrodynamic Force
f	Complex Total Hydrodynamic Force
F^d	Hydrodynamic Force from Diffraction
F^r	Hydrodynamic Force from Radiation
g	Gravitational Constant
H	Waveheight
i	Imaginary Constant
K_{pto}	Restoring Force Coefficient
λ_{pto}	Power Take Off Damping
λ	Wavelength
M	Total Mass
m	Wave Energy Converter Mass
M_c	Mesh Characteristic

μ	Viscosity of the Effective Flow
P	Pressure Field
Φ	Real Velocity Potential
ϕ	Complex Velocity Potential
q	Q-Factor
Z	Radiation Impedance Coefficient
ρ	Fluid Density
S_{ij}	Mean Strain Rate Tensor
S_s	Wave Energy Converter Separation
t	Time
τ	Wave Period
τ_{ij}	Reynolds Stress Tensor
T_r	Transition Region Ratio
$U_{i(j)}$	Time-Averaged Velocity
$u'_{i(j)}$	Fluctuating Velocity Term
V	Volume
ω	Angular Frequency
X	Real Wave Energy Converter Displacement
x	Complex Wave Energy Converter Displacement
X_c	Cells per wavelength
$\dot{x}$	Complex Velocity
Z_c	Cells per waveheight

Chapter 1

Introduction

1.1 Background

The benefits to any type of renewable source of electricity are well understood with many initiatives and production targets being set in countries all over the world [58]. Ocean resources have the potential to become a major contributor to clean energy market with areas of substantial energy density around the world [63, 27]. The wave resource around Australia is discussed in detail in Hemer *et al.* [29], highlighting the potential of Australian coasts. Despite the abundance of ocean energy it remains the least developed renewable energy sector, particularly when compared to wind or solar. This can mainly be attributed to the infancy of the sector, relatively high development costs for devices and the economic viability in the current energy market. Research and development however has led to several successfully demonstrated prototype devices which have been connected to commercial power grids. Along with Wave Energy Converter (WEC) prototype development, numerical studies are applied largely to optimise the designs in various sea states as the cost of experimental testing can be prohibitively large. The outcomes of these numerical studies are of paramount importance when determining a WECs economic viability and survivability. For this reason it is important to obtain accurate and detailed information on a WEC dynamics in the ocean environment.

The numerical approaches to modelling any type of WEC is highly dependent on how it generates it's power. Over time several differing concepts have appeared to harness the ocean wave energy resource and are summarised in [32]. As summarised in Chenari *et al.* [15] we can categorise various designs as either an oscillating water column (OWC), overtopping and point absorbers type devices, each with their own benefits and drawbacks. The OWC operates by enclosing the oscillating water surface inside an air chamber to produce reciprocating airflows which drive a turbine. The OWC can be installed on

either bottom-mounted or floating systems or in breakwaters giving them a large amount of versatility and active area of research, [47, 45]. Several techniques have been applied to improve the performance of this technology. The device from Wave Swell Energy described in Fleming *et al.* [24] is designed to capture energy on only one airflow direction. Extensive tank testing has shown that this design gives significant improvements in performance and allows the use for more efficient single direction turbines as a PTO system.

Overtopping type devices generate power by allowing waves to break into a reservoir during their peak and generate power as the water flows downward through a Power Take Off (PTO) system. An example of this type of device is the Wave Dragon [4] designed in Denmark. Another approach to harnessing power from overtopping waves is under development at the Okinawa Institute of Science and Technology under project Sea Horse. This method uses the natural wave breaking caused by near shore bathymetric variations to drive in-stream turbines. Development of overtopping wave energy technology can be viewed as transforming wave motion to a directional flow which is then used for power generation.

Point absorber technology has no shortage of concepts to capture energy from the oscillating motion of the waves [32]. These devices can be designed to operate in deep water and near shore conditions and can be designed to extract energy from heave, surge or sway wave motions. In deep water, concepts such as the Wavebob or Powerbuoy [36] operate by generating power via the relative motion between two vertically stacked moving bodies. The point absorber type WEC, comprising a large portion of active research is the main focus of the present study.

Companies, such as Carnegie Clean Energy, have begun to realise the potential of point absorber devices and are developing this WEC technology for the Australian coast [40]. The successful Garden Island project saw the deployment of three CETO 5 point absorber type WECs which operated in close proximity. Having WECs in tightly spaced arrays reduce infrastructure costs for parts such as subsea cables and potentially allow for shared mooring systems as described by Wu *et al.* [60]. The work in Harris *et al.* [28] examines the suitability of various mooring systems for use with WECs and highlights which designs are of interest for WEC station keeping. These systems require an accurate understanding of the loading they will experience in normal operating and extreme conditions. The experimental work in Martinelli *et al.* [41] shows a strong influence to the mooring loads from high-order waves in shallow water. Including the added loads from diffracted high-order waves from adjacent WECs is an important but non-trivial problem. Analyzing the excitation forces occurring due to high-order wave diffraction is a key component in answering the WEC placement and mooring questions. However,

all preliminary studies of these devices begin with simple, linear analytical or numerical methods.

Several linear and weakly non-linear numerical approaches are commonly used to model WEC devices with various levels of detail but the advantage of speed over the the fully non-linear CFD approach. To separate inertial and drag or the Froude-Krylov forces, several linear models have been extended to incorporate these as in Giorgi *et al.* [26] and Penalba *et al.* [52], which give accurate approximations of the drag on one or more devices in various wave fields. Weak scattering and fully non-linear approaches have been investigated in Letournel *et al.* [34] which highlight the high-order wave dynamics that are lost when using linear potential flow models. Understanding non-linear forces and wave dynamics is achievable by extending potential flow approaches but in essence are all still limited by it's underlying assumptions. Even though this limitation is well understood these approaches have been successfully applied to WEC studies extensively.

Budal and Falnes [13] used an analytical method to approximate the power output of floating bodies in waves by applying the point absorber approximation which considers the horizontal extent of a WEC to be much smaller than the length fo the incident wave. The optimal power output for a WEC system can then be determined, given that the device operates at resonance with an optimised damping mechanism via PTO system. Applying this approach, a set of theoretical added mass and damping coefficients for a floating cylinder was first presented by Yeung [61] where an eigen-functions approach was used to calculate the added mass and damping coefficients for heave, sway and rolling motions.

The point absorber approximation was then extensively used to calculate the PTO of single devices as in Eriksson *et al.* [21] who modelled a linear generator as a viscous damper exposed to monochromatic and real ocean wave states. PTO estimates for the device were presented with particular focus on the near resonance characteristics. A two-body WEC system was also studied following the point absorber approach in Berggren and Johansson [7] where the relative motion between a floating buoy and submerged plate are used to extract energy. The relative influence of the changing hydrodynamic coefficients from each body onto the other were calculated. WEC array interactions have also been studied by combining the single-body dynamics and the multiple scattering method to account for interference effects between devices in Mavrakos and Kalofonos [42]. Analytical techniques thus provide efficient and quick performance estimates of WECs but require simplified geometries in order to be applicable as suggested by Li and Yu [35]. When considering more complicated geometries, alternative numerical approaches must be employed to calculate the hydrodynamic coefficients for a given WEC.

With increasing complexity in WEC designs and the need for more accurate estimates

of the hydrodynamic coefficients, numerical techniques such as the Boundary Element Method (BEM) and Finite Element Method (FEM) are largely applied for WEC studies. Payne *et al.* [51] apply a BEM model to a sloped heaving buoy WEC design and analyse the response under various damping conditions. This study maintains linearised boundary conditions throughout the model. Other devices such as the OWC type WEC have been studied using the BEM to determine the long term efficiency as in Delaure *et al.* [19] in various offshore sea states. More complex models including shore-based WECs have also be modelled with the BEM. Brito *et al.* [12] investigated a shore-based WEC including bathymetric and topological aspects of the surroundings in the model. Extending to WEC arrays, investigations analysing the total PTO for various WEC spacings and incident wave angles have been studied as in Balitsky [6]. The outcomes provide recommendations for an array configuration based on a WEC geometry.

FEM studies have also been utilised for WEC development. Nader *et al.* [48], applied a FEM model to a floating, moored OWC and showed that a proper choice of the mooring restoring forces and PTO damping can increase the overall device efficiency. These FEM studies have also investigated the interaction of multiple OWCs. Nader *et al.* [49, 47] showed that device spacing has a significant influence on the power capture efficiency of a WEC array and must be considered during the array development phase.

These BEM and FEM studies all employ linearised boundary conditions, in particular on the free surface. The assumptions can become largely inaccurate particularly for large WEC motions which can occur near a devices resonant frequencies [35]. Nonlinear free surface boundary conditions can be applied to BEM and FEM models allowing for higher order waves. Second-order wave theory was applied by Nader [50] and showed an important inconsistency against a fully nonlinear model from Luo *et al.* [38]. The discrepancy was in the wave energy transfer between wave orders leading to an over prediction of the OWC efficiency from the second order model. Fully nonlinear free surface boundary conditions can be solved in the time domain. Bai and Taylor [5] studied the interaction between an impulse wave and an oscillating cylinder and Ferrant *et al.* [23] investigated the nonlinear diffraction fields around a surface piercing structure over a wide range of incident wave frequencies. With an FEM model, Ma *et al.* [39] also studied the interaction between fully nonlinear waves and vertical, surface piercing cylinders. Although these models can implement nonlinear, steep waves, the irrotational, incompressible and inviscid flow limitations remain which exclude viscous and turbulent effects. These methods however, while limited in their capabilities continue to have the advantage of speed over more complex and computationally expensive CFD approaches which have the potential to incorporate viscous and turbulent effects.

The work of Agamloh *et al.* [1] applied the Volume Of Fluid (VOF) technique to simulate one and two inline heaving buoy WECs in a wave flume. This study successfully captured the interaction between multiple devices but was restricted in scope due to the computational time requirements for simulations. The VOF method was again utilised by Yu and Li [62] in a two-body heaving buoy system showing significant nonlinear interactions between both components of the WEC. These Computational Fluid Dynamics (CFD) studies show the importance of nonlinear effects on WEC performance but due to the computational requirements and the relative complexity of CFD modelling, this approach is not commonly used. The benefit of the CFD approach however is the loss of the potential flow restrictions allowing for flow physics to propagate via the closure schemes applied in the models. The CFD approach can then produce state-of-the-art WEC designs that are optimised for real-sea conditions thus producing the most energy possible from any location.

With the steadily increasing availability of the computational resources needed for CFD and the steadily improving solver algorithms, large scope CFD studies of single and multiple WECs are becoming possible. The configuration of WEC arrays has been studied using optimisation techniques in [60, 17, 18]. A hill-climber method was applied to frequency domain linear results in [60] based on the model described in [57]. Several optimising iterations were performed in order to improve the total array efficiency and the importance of constructive interference between devices was seen. With methods for optimised array configurations in development it is becoming possible to find preferable situations which can then be analysed in detail using CFD methods. First however it is necessary to validate and understand the capabilities of a large scale CFD simulation designed to model a full array.

Validating CFD is most easily done with comparisons to experimental findings. The CFD WEC investigation applied in this work assumes that the diffraction and radiation problems are separable and treatable independently, as is the case for linear models. With this it is possible to analyse the wave height and oscillation amplitude effect on both the excitation force and radiation damping coefficients essential to predicting WEC performance. This work serves as a direct extension of the experiments on submerged spherical WECs performed in the wave basin at the Australian Maritime College. Preliminary results from which are presented in Penesis *et al.* [53] and Nader *et al.* [46]. The experimental conditions remain within linear theory applicability allowing the results to be scaled in the absence of significant nonlinear behaviour. The work presented in this thesis aims to investigate the onset of nonlinear dynamics on submerged heaving and surging spherical WEC arrays in open water. Experimental results from those presented in [53, 46] are used

to validate and quantify the error in linear FEM and nonlinear CFD modelling for the base single WEC case.

1.2 Methodology and Theory

1.2.1 Water Waves

Linear wave-body interaction modelling is based on the irrotational, incompressible and inviscid flow giving a velocity potential, $\Phi(x, y, z, t)$, such that,

$$\nabla^2\Phi = 0, \tag{1.1}$$

which describes the flow field valid everywhere in the computational domain.

By considering small wave amplitudes the linearized mean surface boundary condition can be written as,

$$\frac{\partial\Phi}{\partial z} + \frac{1}{g}\frac{\partial^2\Phi}{\partial t^2} = 0. \tag{1.2}$$

Considering that the systems are linear, Eqn. (1.2) can be solved for a given incident wave frequency making a solution for more complicated sea states obtainable via the superposition principal. Given that individual frequencies can be treated independently, the velocity potential can be written in the complex domain as,

$$\Phi = \Re\{\phi(x, y, z)e^{-i\omega t}\}, \tag{1.3}$$

where i is the complex unit and ω the angular frequency.

This is the basis for analytical, BEM and FEM linear frequency domain models when studying WEC performance in a particular environment. This approach however becomes inadequate in describing the wave profiles once the wave amplitude increases or the water depth shallows. Linear solutions can be extended to include higher order terms from the Taylor expansion to account for this.

Introducing these nonlinear, high-order terms following the wave conditions illustrated in Fig. 1.1, quickly increases the model complexity. Furthermore, these methods continue to neglect the effects of viscosity and turbulence between the device and the environment. For clarity in what follows, nonlinear effects refer to viscous and turbulent flow properties and lose all association with wave descriptions. Large amplitude, previ-

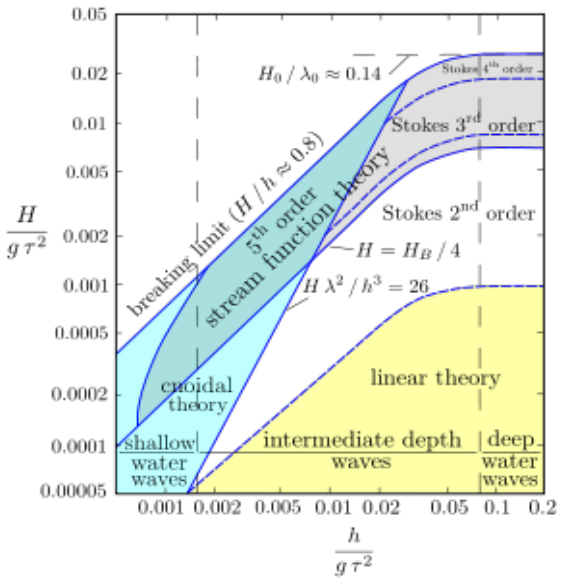

Fig. 1.1 Wave theory applicability as described in [33].

ously 'nonlinear' waves will be referred to as high-order waves.

1.2.2 The Equation of Motion for a Wave Energy Converter

A heaving or surging point absorber type WEC is excited via the incoming waves from the environment. The motions of a WEC of this type are described following the equations of motion given a displacement X_i with $i = 1,2,3$ for surge, sway and heave motions respectively,

$$M\frac{d^2X_i}{dt^2} + \lambda_{pto}\frac{dX_i}{dt} + K_{pto}X_i = F_i, \tag{1.4}$$

where M is the WEC mass, λ_{pto} is the damping induced by the PTO system, K_{pto} is the restoring force coefficient including PTO and mooring effects and F_i is the hydrodynamic force which can include nonlinearities such as viscous, turbulent or free surface interactions. If F_i is linear however, the equation of motion Eqn. (1.4) can be readily solved using BEM or FEM numerical methods.

The Hydrodynamic Coefficients

When considering the problem of a submerged spherical WEC with linear potential flow theory, the total hydrodynamic force can be separated into both the diffraction and

radiation components,

$$F_i = F_i^d + \sum_{j=1}^{n} F_{ij}^r, \tag{1.5}$$

where F_i^d represents the hydrodynamic force from diffraction and F_{ij}^r the force from radiation. Nader *et al.* [47, 45] explains the physical meaning of F_i^d as the force a WEC would experience if held stationary in oncoming waves and F_{ij}^r as the force on the WEC as it oscillates in still water. Following the phenomenological theory outlined by Falnes [22] the general expression for the equations of motion of each WEC in an array with incident wave amplitude η_o in the complex plane is given by,

$$(\gamma_i + Z_{ii})\dot{x}_i = \Gamma_i \eta_o - \sum_{i=0, j\neq i}^{n} Z_{ij}\dot{x}_j, \tag{1.6}$$

with,

$$\gamma_i = \lambda_{pto,i} + \frac{i}{\omega} K_{pto,i} - i\omega m, \tag{1.7}$$

which includes the effects of PTO damping $\lambda_{pto,i}$, restoring force $K_{pto,i}$ and WEC mass m. The complex excitation coefficient Γ_i and radiation impedance coefficient Z_{ij} are related to the linearly separable diffraction and radiation forces as,

$$||\Gamma_i|| = \frac{|F_i^d|}{\eta_o} \quad \text{and,} \quad ||Z_{ij}|| = \frac{|F_{ij}^r|}{||\dot{x}_j||}, \tag{1.8}$$

with phase angles θ,

$$\theta_{\Gamma_i} = \theta_{F_i^d} - \theta_{Reference} \quad \text{and,} \quad \theta_{Z_{ij}} = \theta_{F_{ij}^r} - \theta_{x_j} + \frac{\pi}{2}. \tag{1.9}$$

The excitation force coefficients $||\Gamma_i||$ described in Bharath *et al.* [10] are here found through linear FEM, CFD and experimental means. When comparing $||\Gamma_i||$ for each device in an array to that of same number of independents WEC $||\Gamma_o||$, we can calculate the array excitation force $||\Gamma^m||$ defined in Eqn. 1.10. These values describe the potential energy gains or losses brought about by the specific array configuration.

$$||\Gamma^m|| = \frac{\sum_{i=1}^{n} ||\Gamma_i||}{n||\Gamma_o||}. \tag{1.10}$$

We can determine the power output of a single or array of WECs with,

$$P_i = \frac{1}{T}\int_0^T F_{i,j}\dot{X}\,dt = \frac{1}{2}\Re\{f_i\dot{x}_i\} = \frac{1}{2}\Re\{\gamma_i\}||\dot{x}_i||^2 = \frac{1}{2}\lambda_{pto,i}||\dot{x}_i||^2, \tag{1.11}$$

given in Childs *et al.* [56, 16], where f_i is the complex force amplitude. Upon determining the power generated from each device in the array we can define the q-factor which similar to $||\Gamma^m||$ relates an array to the performance of multiple isolated devices as,

$$q = \frac{\sum_{i=1}^{n} P_i}{nP_o}. \tag{1.12}$$

This quantity q from Eqn. 1.12 illustrates the device interaction within an array configuration implying that an array with $q > 1$ has constructive interference while those with $q < 1$ are destructive. The coefficients can be calculated for a given configuration quickly and efficiently excluding nonlinear effects on the forcing parameters F_i. The CFD approach follows the same linear methodology to determine the hydrodynamic coefficients but now include effects from viscosity, turbulence and other nonlinear effects.

The notation associated with radiation impedance coefficients described in the following apply throughout this work. Forcing or oscillation axis (x, y, z) correspond to surge, sway and heave with positive surge and heave taken along the direction of wave propagation and upward in the water column. Positive sway follows via the standard coordinate orientation. The active WEC is denoted with A and the subsequent WECs are denoted as $1, 2, 3$ depending on the array under consideration. Radiation impedance coefficients are thus denoted as Z^k_{minj} where $m, n = x, y, z$ and $i, j = A, 1, 2, 3$ and is interpreted as the radiation impedance in the mth direction on the ith device due to nth motion from the jth device with k WECs in the array. The subscripts n, j are dropped in the cases when $k = 1$.

Considering then, a single device Eqn. (1.6) reduces to,

$$\dot{x}_A = \frac{\Gamma_1 \eta_o}{\lambda_{pto,A} + \frac{i}{\omega} K_{pto,A} - i\omega m + Z_A}, \tag{1.13}$$

which allows for a simple determination of the optimum PTO damping for the WEC as,

$$\lambda_{pto,A} = || - \frac{i}{\omega} K_{pto,A} + i\omega m - Z^1_{mA}||. \tag{1.14}$$

It should be noted that $\lambda_{pto,1}$ does not represent the optimum damping value for each device in the array, rather acts as a minimum bound that with further optimisation can increase the arrays performance. For the present study we are interested in using CFD to study Z^k_{minj} and for the arrays considered in this study shown in Section 4.2.1 we note that the reciprocity relation is valid in that $Z^k_{minj} = Z^k_{njmi}$. As the array placement is symmetric

we can assign the forces to various locations in the Z^k_{minj} matrices.

$$Z^2_{minj} = \begin{bmatrix} Z_{mAnA} & Z_{mAn1} \\ Z_{mAn1} & Z_{mAnA} \end{bmatrix}$$

$$Z^4_{minj} = \begin{bmatrix} Z_{mAnA} & Z_{mAn1} & Z_{mAn2} & Z_{mAn3} \\ Z_{mAn1} & Z_{mAnA} & Z_{mAn3} & Z_{mAn2} \\ Z_{mAn2} & Z_{mAn3} & Z_{mAnA} & Z_{mAn1} \\ Z_{mAn3} & Z_{mAn2} & Z_{mAn1} & Z_{mAnA} \end{bmatrix}$$

The Linear Finite Element Model

The FEM model used in this study is described in detail in [48, 49, 47, 45] and is adapted to accommodate the spherical WEC. In this model the fluid domain is separated into two parts with the same matching, external surface and radiation condition. The main difference is the boundary condition on the body for the different problems. For the diffraction and radiation problems the incident wave potential ϕ_{inc} and WEC surface boundary condition ϕ_b with k the wave number defined as: for the diffraction problem,

$$\phi_{inc} = \frac{-ig}{\omega}\frac{H}{2}\frac{cosh(k(z+h))}{cosh(kh)}e^{ikx}, \tag{1.15}$$

$$\frac{\partial \phi_b}{\partial n_N} = 0, \tag{1.16}$$

and the radiation problem for motion i,

$$\phi_{inc} = 0, \tag{1.17}$$

$$\frac{\partial \phi_b}{\partial n_N} = u_i \cdot n_N, \tag{1.18}$$

where $\partial/\partial n_N$ is the derivative in the direction of the unit vector N_N normal to the surface of the sphere pointing outward of the fluid. This type of boundary condition was previously tested and validated for a heaving OWC device [48].

The mesh was generated using ANSYS ([3]) meshing tool (Fig. 1.2) and exported into Matlab to apply the model. Tetrahedral elements with vertex nodes and the middle of each edge as well as quadratic shape functions were used. Half of the domain was modelled, taking advantage of the problem symmetry and the element size refined around the sphere and free surface. Element sizes were taken as invariable throughout the volume of the

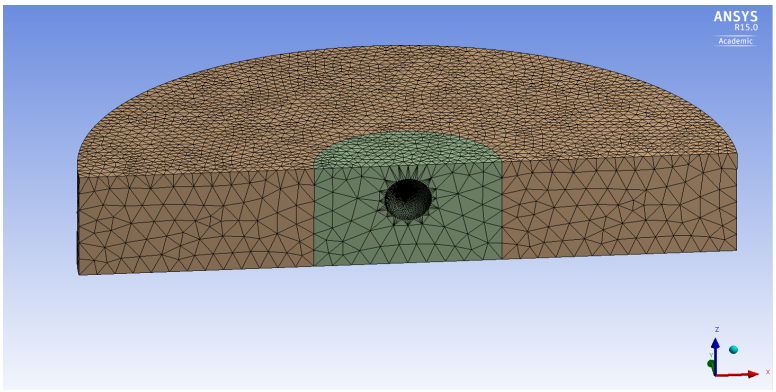

Fig. 1.2 ANSYS meshing for the FEM model of the single model.

domain and adjusted to have at minimum ten elements per wavelength. A typical mesh, as the one presented in Fig. 1.2 contains approximately 180000 nodes and 130000 elements.

RANS VOF Method

The Reynolds averaged Navier-Stokes (RANS) simulations were conducted using the commercial CFD software CD-Adapco STAR-CCM+ version 10.02.012. The incompressible RANS equations were discretised in the fluid domain using the finite volume method while capturing the free surface via the VOF method. Turbulence closure was achieved by means of the Menter shear stress transport model (SST) [44]. The development of the numerical models used for this work follows below.

Reynolds averaging involves decomposing the instantaneous velocity and pressure fields into mean and fluctuating components. Using the time-averaged forms of the non-dimensionalised continuity and momentum equations creates the basis of the RANS model,

$$\frac{\partial U_i}{\partial x_i} = 0, \tag{1.19}$$

$$S_{ij} = \frac{1}{2}\left(\frac{\partial U_i}{\partial x_j} + \frac{\partial U_j}{\partial x_i}\right), \tag{1.20}$$

$$\rho\left(\frac{\partial U_i}{\partial t}\right) + \rho\frac{\partial}{\partial x_j}(U_i U_j) = \frac{\partial P}{\partial x_i} + \frac{\partial}{\partial x_j}(2\mu S_{ij} + \rho\tau_{ij}), \tag{1.21}$$

where,

$U_{i(j)}$ = Time-averaged velocity

P = Pressure field

μ = Viscosity of the effective flow

ρ = Density of the effective flow

S_{ij} = Mean strain rate tensor

$\tau_{ij} = -\overline{u_i' u_j'}$ = Reynolds stress tensor

$u'_{i(j)}$ = Fluctuating velocity term

The stress tensor (S_{ij}) in this formulation remains an unknown. To close RANS equations, various parametric turbulence models can be applied. This study solves the stress tensor by means of the SST turbulence model. In this the kinematic eddy-viscosity values are constrained to allow the propagation of shear stresses. The SST approach applies the $k-\epsilon$ turbulence model in the far-field away from boundaries while using the $k-\omega$ method to resolve near wall flows.

The VOF method tracks the distribution of each phase on every given time-step with reference to a given volume [14]. The volume fraction α_i of a given fluid i is defined in a closed volume V as:

$$\alpha_i = \frac{V_i}{V} \tag{1.22}$$

Applying this fluid discretization, Star-CCM+ models the density as,

$$\rho = \sum_i \alpha_i \rho_i, \tag{1.23}$$

leading to a simplified form of the mass conservation law,

$$\int_S (v \cdot n) dS = \sum_i \int_V \left(s_{\alpha_i} - \frac{\alpha_i}{\rho_i} \frac{D\rho_i}{Dt} \right) dV, \tag{1.24}$$

with S the surface area, n the surface normal and v the velocity.

1.2.3 Overset Mesh Motions

Throughout this work, the 6 degrees of freedom modeling capabilities of Star-CCM+ are use to govern and restrict the motions of the WECs. In the diffraction studies, these methods are not employed as there is no motion in the WECs. For the radiation studies

both vertical and horizontal oscillating motions are governed by specifying the time dependent velocity of the WEC via Eqn. 1.25,

$$U_{WEC} = -\omega A \sin(kx - \omega t). \tag{1.25}$$

It was quickly found that a WEC must begin at a zero velocity within the radiation simulations in order to prevent instabilities leading to run failures.

For the fully active WEC studies presented in Chapter 5, the motions of the WEC are restricted to the vertical only with a linear restoring force and damper applied to model the mooring and PTO respectively. The values applied to the restoring and damping forces are described further in Chapter 5. The weight of the WEC was prescribed equal to weight of the water it displaces to achieve the neutrally buoyant state.

1.2.4 Thesis Organisation

The body of this thesis develops the models to study array interaction starting from a single device and building to small arrays.

Firstly, a study of an isolated heaving and surging WEC is presented in Chapter 2. The hydrodynamic coefficients are investigated in each case along with an analysis of the flow profiles surrounding the WEC. The final results suggest that the impact of the WEC design on the surrounding wave field has a non-negligible impact on the forcing dynamics which are ultimately used to generate energy.

The work in Chapter 3 analyses the diffraction problem for generic WEC arrays of both two in a row and four in a square configurations at various device spacings. Incident wave frequency and amplitudes are altered to study the excitation force on each WEC in the array near the linearly predicted wave-WEC interaction resonance. This work is then compared to linear FEM results. The outcomes of this work show the excitation force on the combined array and the effect a WEC has on the environment and it's subsequent impact throughout the array.

Chapter 4 discusses the radiation impedance on an array of devices occurring from the WEC motions in both heave and surge from an active WEC in calm water. Results show the comparisons of the findings from both linear and nonlinear approaches and combine with results from the diffraction problem the estimates of the power output potential are calculated. The free surface behaviour due to the radiating sphere is presented and discussed and the outcomes of this work suggest the variation of the array performance of WECs when incorporating nonlinear effects. A fully active single WEC restricted to move in heave is then examined in Chapter 5 giving insight into the nonlinear coupling between

the diffraction and radiation problems.

The end results of this work offer a validated approach useful for studying WEC arrays nonlinearly and efficiently. The numerical design applies linear methodology to solve for the parameters needed to calculate the power take off of a WEC separating excitation and radiation, thus decoupling the nonlinear effects between these motions. This allows for a more detailed analysis of the inherently complicated nonlinear behaviour and gives significant insight into the factors driving WEC dynamics. The outcomes of this work are important to future design of CFD studies in that they can be more focused and thus more meaningful to companies aiming to determine in detail the potential of their technology and what can be expected in terms of a return on investment.

Chapter 2

Nonlinear Modelling of a Single Generic Wave Energy Converter

This chapter is accepted for publication and is in press for the Journal of Renewable Energy at the time of writing. The journal publication here has been edited, altering the introduction, theory and conclusion sections but is otherwise unchanged from the original article:

Bharath A., Nader J-R., Penesis I., Macfarlane G., Nonlinear hydrodynamic effects on a generic spherical wave energy converter. (2018) *Renewable Energy*, 118(Supplement C):56-70.

2.1 Abstract

Analytical and numerical modelling techniques have been used extensively to predict the performance and power output of these devices using linear, inviscid and irrotational theory with the knowledge that nonlinear effects become relevant in extreme cases. This study applies Reynolds averaged Navier-Stokes (RANS) computational fluid dynamics (CFD) model to simulate the diffraction and radiation problems for a single submerged spherical WEC operating in both heave and surge. Wave and device oscillation amplitudes from 30mm to 60mm and frequencies from 0.8Hz to 1.2Hz are employed to examine the fluid dynamics near the spherical WEC as the hydrodynamics deviate away from the linear regime. Results of the hydrodynamic coefficients from wave basin experiments are used to validate linear finite element and CFD models for small wave amplitudes. The nonlinear CFD model is then extended to model larger amplitudes. The hydrodynamic coefficients are here found to be amplitude dependent with free surface interactions being a key component of the deviation from linear theory. The rate of these deviations from low

wave height, linear values via increasing wave heights is also found to vary with frequency. The outcomes highlight limitations in the linear approach and address the factors most important to WEC performance.

2.2 Introduction

The novel CFD WEC investigation applied here assumes the diffraction and radiation problems are separable and treatable independently, as is the case for linear models. With this method it is possible to analyse the wave height and oscillation amplitude effect on the excitation force and radiation damping coefficients which are essential to predict WEC performance. This work serves as a direct extension of the experiments on submerged spherical WECs performed in the wave basin at the Australian Maritime College. Preliminary results from which are presented in Penesis *et al.* [53] and Nader *et al.* [46]. The experimental conditions remain within linear theory applicability allowing the results to be scaled in the absence of significant nonlinear behaviour. The current study aims to investigate the onset of nonlinear dynamics on a submerged heaving and surging spherical WEC in open water. Experimental results presented in [53, 46] are used to validate and quantify the error in linear and nonlinear modelling. Firstly, a study of the diffraction problem is presented followed by the radiation problems for both heaving and surging WECs. The hydrodynamic coefficients are investigated in all three cases along with an analysis of the flow profiles surrounding the WEC. The final results suggest that the impact of the WEC design on the surrounding wave field has a non-negligible impact on the forcing dynamics which is ultimately used to generate energy.

2.3 The CD-Adapco Star-CCM+ Model and Computational Mesh Development

2.3.1 Numerical Wave Tanks

This study consists of two independent 3D numerical wave tanks (NWTs) shown in Fig. 2.1. Both NWTs contain a 250mm diameter sphere with the still centre positioned 395mm vertically up from the tank floor. The still water level in each case is 600mm. The diffraction study NWT, Fig. 2.1a, considers a still sphere in regular waves. The NWT for the diffraction study uses a rectangular tank placing the sphere 20 sphere diameters (SD) from the numerical velocity inlet and 40 SD from a numerical pressure outlet. The side wall is placed 16 SD parallel to the direction of wave propagation. This model takes advantage of

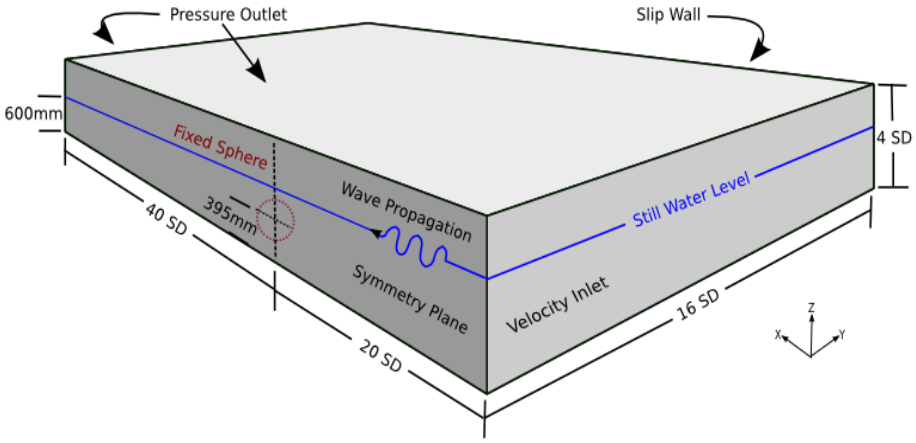

(a) The diffraction study NWT.

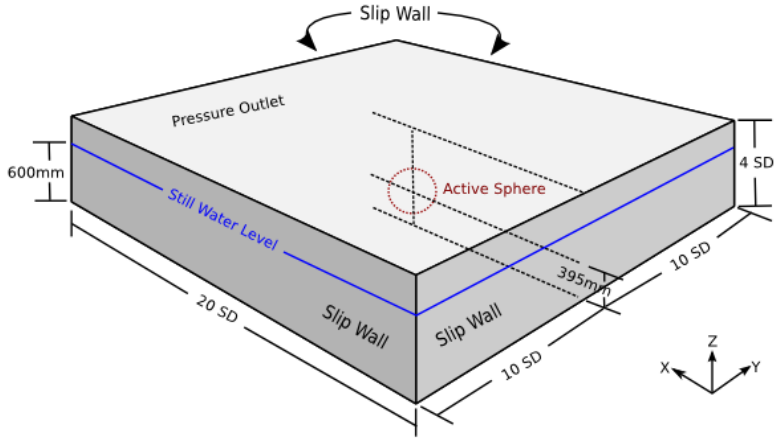

(b) The radiation study NWT.

Fig. 2.1 NWTs used to study the diffraction and radiation problems for a submerged spherical WEC. The sphere diameter (SD) for this study is 250mm.

the problem symmetry as in the linear case where the computational domain is divided in two applying a numerical symmetry plane through the center of the sphere.

The radiation study, Fig. 2.1b, contains an oscillating sphere in calm water. The numerical wave tanks used for the radiation study are square tanks with the domain edges 10 SD from the sphere. The overset meshing technique was used to allow for sphere motion. The full domain was modelled in this case owing to meshing difficulties deriving from the sphere motion within the numerical symmetry plane. In both cases, simulation run times were chosen to neglect wave reflections. Numerical wave propagation was tested by varying the free surface resolving mesh size. Sphere surface resolution and mesh boundary layers were tested to minimise pressure force variation. The overset mesh

region size was studied in order to ensure minimal error in fluid flow due to inaccuracies generated from the data interpolation between regions. The following sections show the results from these mesh studies.

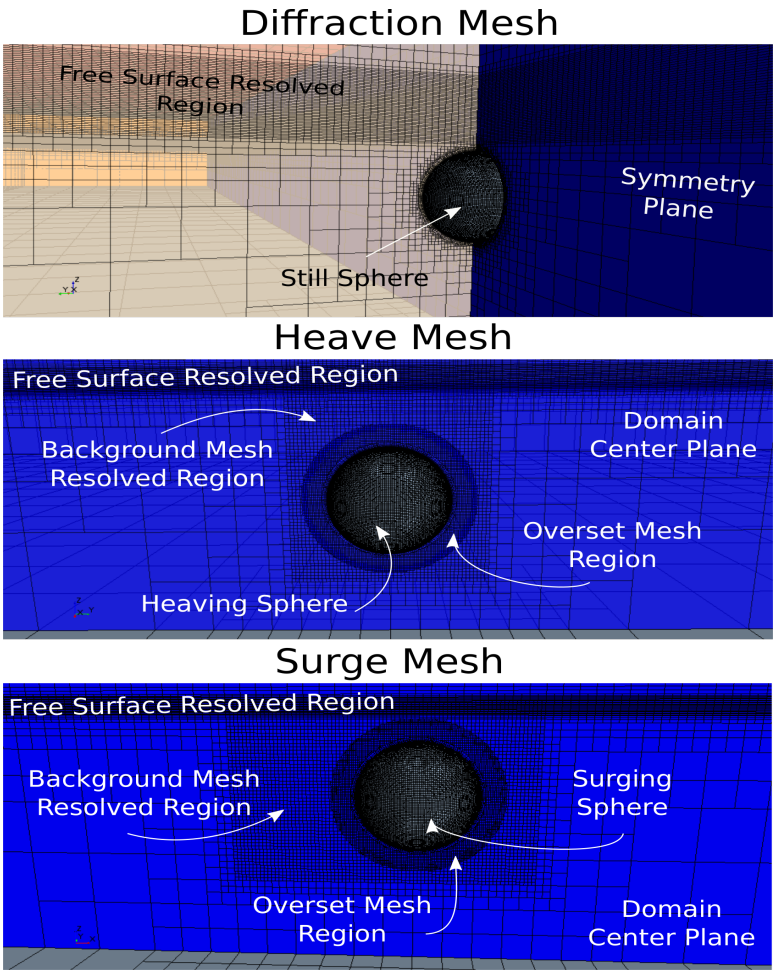

Fig. 2.2 The computational mesh set ups associated with each study.

2.3.2 Plane Wave Propagation

The Courant-Friedrichs-Lewi condition $C_{FL} < 1$ is a common criteria used to apply limits to the maximum computation mesh size defined as,

$$C_{FL} = \frac{U_0 \Delta t}{\Delta x} + \frac{U_0 \Delta t}{\Delta z}. \tag{2.1}$$

For plane waves propagating along the x-axis with the vertical along the z-axis, we can define $U_0 = 2\pi f A$ in terms of the wave parameter and represent C_{FL} as,

$$C_{FL} = C_{FL}^{x} + C_{FL}^{z} = \frac{\omega \Delta t}{2}\left(\frac{k(X_c)A}{\pi} + Z_c\right), \tag{2.2}$$

where X_c and Z_c represent the number of computational cells per wavelength (λ) and wave height (H) respectively. Guidelines to begin mesh development were obtained from the International Towing Tank Conference (ITTC) proceedings [31] which states $X_c = 40$ and $Z_c = 20$. Waves were generated in intermediate depth water ($d/\lambda = 0.1$) introduces non-linear components to the propagating wave according to [43] and so the second order Stokes wave is used for CFD wave comparisons. Percentage errors for X_c and

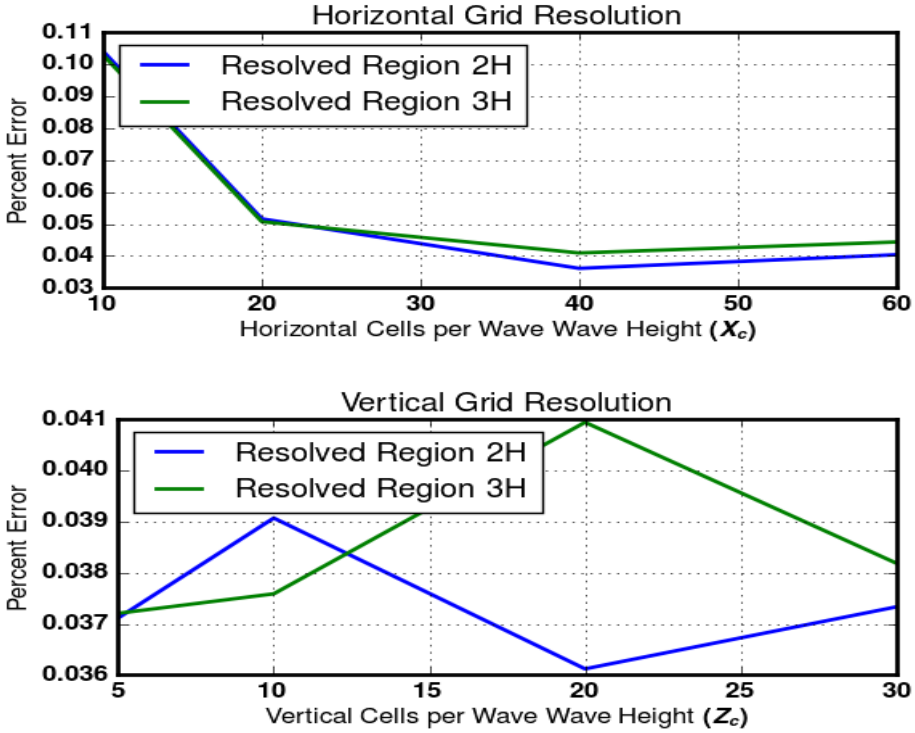

Fig. 2.3 Percentage errors versus expected wave amplitude for both X_c (top) and Z_c (bottom) mesh variations at 10m from the domain inlet.

Z_c variations are shown in Fig. 2.3 with a fixed numerical time step $\Delta t = 0.001$ s. The wave height errors variations are found to rely largely on X_c. For values $X_c < 10$, CFD wave heights begin to drop quickly once created at the inlet and were found to attenuate to negligible levels after 5 periods of propagation. For $10 \leq X_c < 25$ wave heights stabilise throughout the numerical tank but the non-linear nature of the wave profiles was lost

resulting in phase inaccuracies along the direction of propagation. Correct profiles and phases were seen with $X_c \geq 30$ to an error level of 4% with only marginal improvement coming from further increases in X_c.

Z_c was found to have a minor impact on the overall wave propagation for values

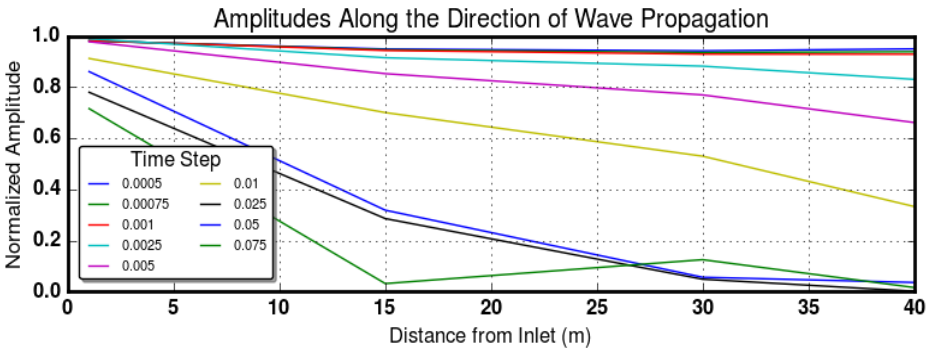

Fig. 2.4 Wave heights along a numerical tank with various solver time steps.

$Z_c > 15$. Variations in the wave errors were < 1% for simulations with $X_c \geq 30$ and did not appear to influence the accuracy of the waves if X_c was too low. It was observed however that for values of $Z_c < 10$, simulations suffered from wave diffusion as they did with $X_c < 10$ and attenuated quickly after their initial creation.

Time step size also has an effect on the C_{FL} value and wave propagation accuracy. Figure 2.4 shows the CFD wave heights measure from simulations with $X_c = 40$ and $Z_c = 20$ with various second-order discrete time step values. It can be seen in Fig. 2.4 that attenuation minimums are reached with $\Delta t < 0.001$ s and remain at a constant maximum error value of 4% against the expected wave amplitude throughout the length of the numerical tank. Time step values an order of magnitude large lead to rapid wave height attenuation as Fig. 2.4 shows > 50% loss for $\Delta t > 0.025$ within 2 periods of propagation. From this work on mesh and time step dependence we can conclude that the mesh values proposed in [31] are sufficient for accurate wave propagation combined with $\Delta t \leq 0.001$ giving C_{FL} limits of $C_{FL}^x < 0.0002$ and $C_{FL}^z < 0.0328$ to further studies.

Sphere Surface Mesh

The spherical shape resolution and the influence on measured forces were study for this investigation. Surface mesh sizes in the Star-CCM+ surface remesher were restricted to values of total sphere surface area divided by single cell sizes of 19.64, 26.18, 39.27, 78.54, 98.17. The peak forces measured and the variation in the time series data are given in Table 2.1.

We can see that there is minimal change to the apparent force on the sphere with

Table 2.1 Cell size resolution of the submerged sphere.

Cell Size	Peak Force (N)	σ	Discrete Difference (mm^2)
19.64	1.17	0.14	11.870
26.18	1.18	0.15	24.260
39.27	1.17	0.15	89.660
78.54	1.24	0.18	137.540
98.17	1.19	0.13	345.320

Table 2.2 The forces appearing on the sphere surface with various y^* values and cell size ratio 39.27.

y^*	Heave Force Amplitude (N)	Surge Force Amplitude (N)
166	2.135	2.828
83	2.117	2.824
42	2.119	2.816
28	2.087	2.811
21	2.017	2.810

the variation in surface cell size. The differences in surface area of the discrete sphere and the theoretical values given in Table 2.1 would offer an insignificant correction to the measured force values and are neglected. Focusing on a surface resolution of 39.27 we can study the force variation with increased first cell wall distance.

In the absence of turbulent modelling parameters the wall distance will be given as y^*, the sphere diameter divided by first cell distance from the sphere surface. The values analyzed in this study were $y^* = 166, 83, 42, 28, 21$. Table 2.2 presents the peak for amplitudes in the heave and surge orientations. From Table A.1 we can see an increase in the measure forces with increasing y^*. For the heave forces an apparent peak amplitude variation of 0.116 N constituting 5.5% change in measured forcing. The variability in the measured values is small across the studied meshes. The surface meshes used further in this study had a surface cell size of 39.27 and y^* of 83.

2.3.3 Computational Meshes

Three separate and unique mesh configurations where used in this work to model the diffraction and radiation wave fields emanating from the submerged sphere. Examples of each mesh configurations are depicted in Fig. 2.2. The mesh constructed for the diffraction case contained a highly resolved mesh region surrounding the free surface which was established in each case to ensure complete coverage of the waves. The surface meshing on the sphere was also resolved in order to minimize numerical variability associated with the mesh sizing.

The meshes used to simulated the heave and surge radiation fields both make use of the overset meshing capabilities available in Star-CCM+. The overset and background mesh regions for both configurations are shown in Fig. 2.2 with the spheres in both cases positioned at their respective oscillation extrema. The sizes of the overset regions were tested in this work to minimize errors associated with the inter-region interpolation inherent in the overset method. The mesh variability studies associated with the current study's development follow in the following sections.

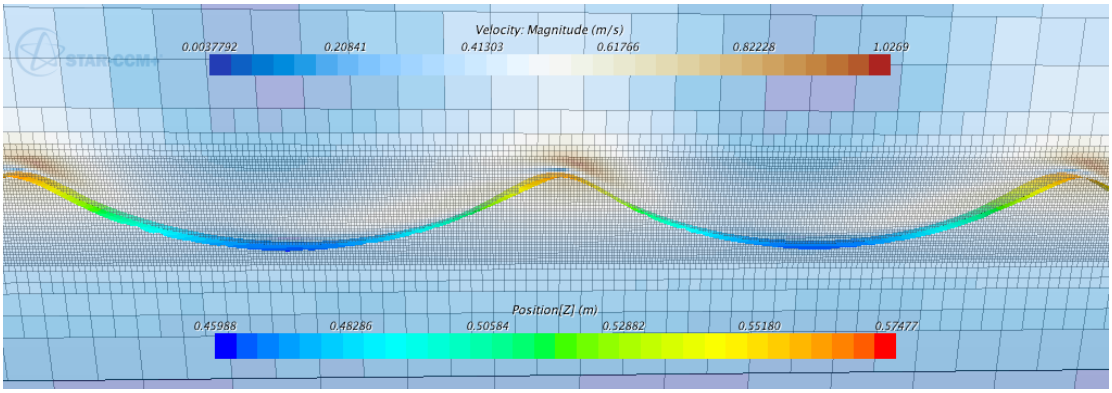

Fig. 2.5 An example of a propagating wave with $M_c = 2$.

The Monochromatic Wave

A monochromatic VOF 5^{th}-order Stokes wave is created using the built-in velocity and volume fraction boundary conditions in Star-CCM+. The dissipation of wave energy is largely dependent on free surface mesh resolution. As a starting point for free surface mesh development, the International Towing Tank Conference [31] recommends no less than $X_c = 40$ computational cells per wavelength λ and $Z_c = 20$ cells per wave height H.

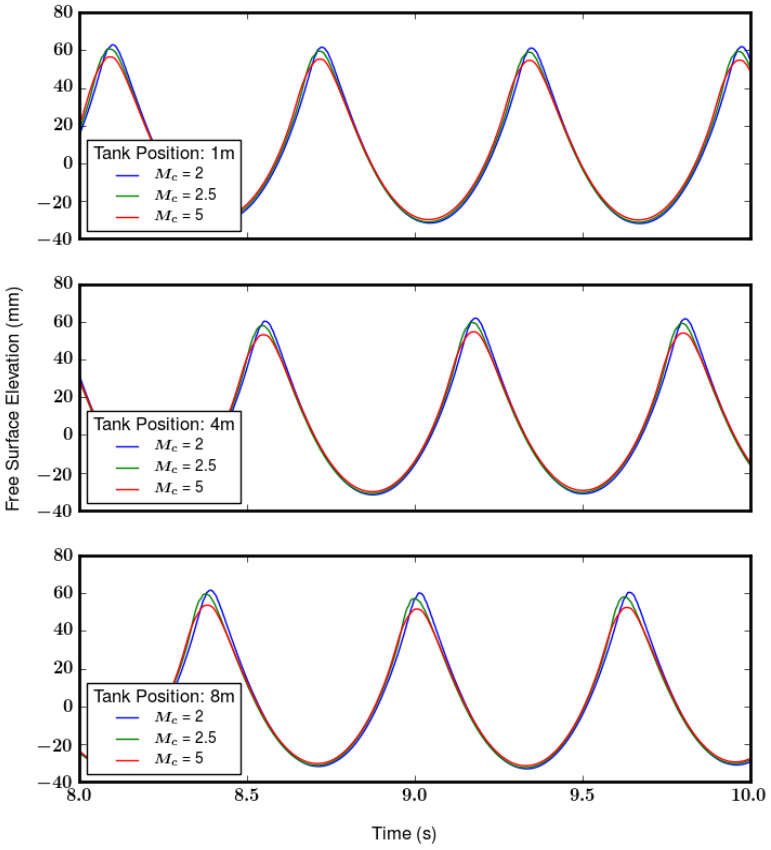

Fig. 2.6 Free surface elevation along the NWT: 1m top, 4m center, 8m bottom, for various values of M_c and constant Z_c.

Here we quantify free surface meshes as the mesh characteristic,

$$M_c = X_c / Z_c = \frac{Cells}{\lambda} \cdot \frac{H}{Cells}. \tag{2.3}$$

and vary M_c to analyze wave propagation.

Fig. 2.5 gives an example of a left to right propagating wave through a NWT with the computational mesh displayed. The vertical slice showing velocities indicates a point of relatively fast fluid motion in the air region. With insufficient mesh resolution this area of high velocities tends to grow and erodes the peak elevation of the wave. Fig. 2.6 shows free surface elevations along the NWT for various M_c values with fixed Z_c. We see the mesh effects on the wave peaks. For $M_c = 5$ there is a consistent drop in peak elevation compared to lower values which occurs < 1m after the wave is produced at the inlet.

Table 2.3 shows the wave amplitudes normalised by the linear wave amplitude values

Table 2.3 High-order wave propagation through a NWT. High-order CFD wave amplitudes are normalised by theoretical linear values.

Position	**Normalised Amplitudes**		
(m)	$M_c = 2$	$M_c = 2.5$	$M_c = 5$
1	1.22	1.18	1.10
4	1.21	1.16	1.06
8	1.20	1.16	1.04

Table 2.4 The heave forces appearing on the sphere surface for various transition region distances and cell size ratio 39.27.

Transition Region Ratio	**Heave Force Amplitude (N)**
1.12	7.28
1.28	7.55
1.44	7.31
1.6	6.38

for the various meshes tested. We can see that the CFD waves propagating in meshes $M_c = 2$ and 2.5 that there is minimal wave height reduction over an 8m length reducing by $\approx 1\%$. In coarser meshes however, $M_c = 5$, the initial wave height is considerably lower in comparison reducing by $\approx 5\%$ over 8m of propagation. This diffusion is also largely effected by the simulation time step, which is discussed in detail in Bharath *et al.* [9] and here chosen to be a second-order discretization with a 0.001s step size. From this investigation, meshes with $M_c \leq 2.5$ are used in all NWTs and due to cut-cell meshing restrictions within Star-CCM+ this is used as a minimum requirement. Adhering to these conditions we ensure the intended numerical wave appears on the WEC.

Overset Mesh

The overset meshing technique available in Star-CCM+ allows for a moving sphere within the model without requiring mesh deformation or remeshing processes during simulations. This allows for greater control of surface and boundary layer mesh sizing and eliminates the error associated with interpolating results to remeshed domains. However, fluid flow must still be interpolated between the overset and background mesh regions. The errors associated with this interpolation are proportional to the cell size in the transition region. When testing various overset mesh configurations, the focus was on the variations of measured pressure forces on the heaving sphere. The transition region was placed further from the sphere surface and the cell sizing was varied in the overset region. The transition region distance from the sphere surface is given by the transition region ratio T_r defined as the radius of the overset region divided by the sphere radius. Two

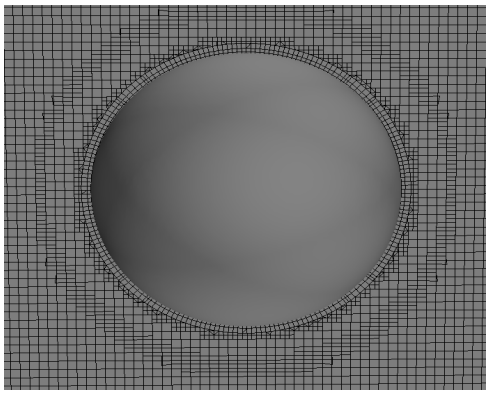

(a) $T_r = 1.28$ and overset interior cell size 10mm^3.

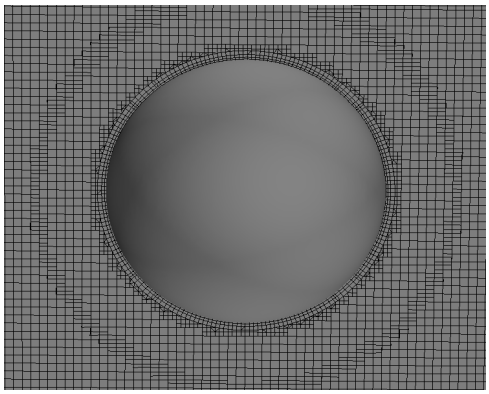

(b) $T_r = 1.6$ and overset interior cell size 10mm^3.

Fig. 2.7 Overset meshes with $T_r = 1.28$ and 1.6 and overset interior cell sizes of 10mm^3. The transition region between the background and overset regions can be seen in the grid line overlap.

examples of the tested overset mesh regions are shown in Fig. 2.7.

Examples of the force on and velocity field normalised by the oscillation amplitude and frequency $A\omega$ around a heaving sphere are depicted in Fig. 2.8. The effects on these quantities due to the transition region placement (in this case $T_r = 1.28$) is quite clear. False high frequency variations appear in the force values which are induced by high variability in the flow field. This effect is attributed to the interpolation algorithm attempting to interpolate complex shear flows near the sphere surface across the transition region. This effect was not observed with $T_r = 1.6$ producing relatively lower force amplitude values shown in Table 2.4. This lead to the use of a transition ratio equal to 1.6 for all radiation simulations in this work.

2.4 Results and Discussion

Here the results from each modelling method of the submerged WEC are discussed. CFD wave and WEC oscillation amplitudes are 30mm, 40mm, 50mm and 60mm with frequencies of 0.8Hz, 1.0Hz and 1.2Hz. The experiments conducted in the model test basin at the Australian Maritime College presented in [53, 46] mirror the CFD model in terms of the WEC sizing, position, frequency and water depth however incident wave heights were restricted to 30mm to ensure linear interaction. The data gathered during the experiments are then comparable to low amplitude CFD results without the influence of model scale effects. Thus experimental results are here used to validate the forcing

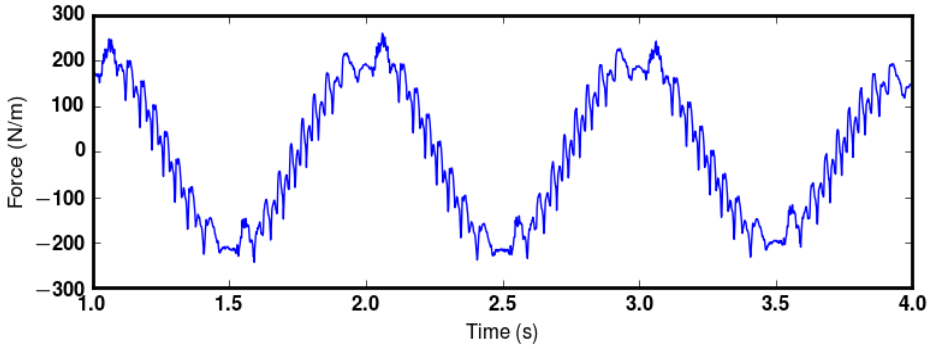

(a) Heave force F_h, appearing on the submerged WEC with $T_r = 1.28$.

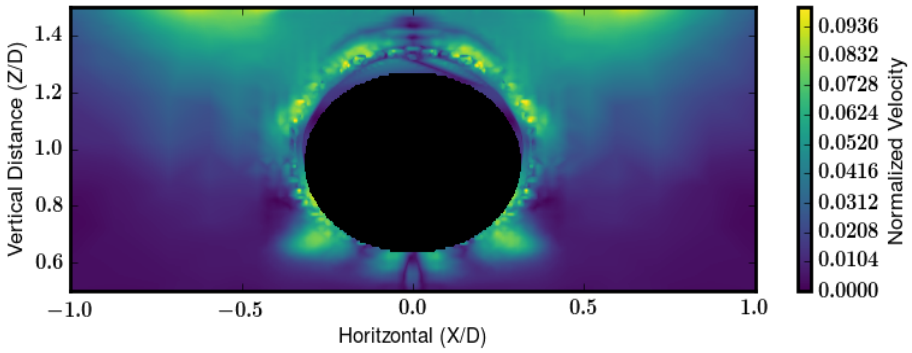

(b) Instantanious flow field appear around the submerged WEC with $T_r = 1.28$.

Fig. 2.8 Heave force F_h and velocity flow fields $U/A\omega$ resulting from an insufficient overset mesh with $T_r = 1.28$.

amplitudes produced through both FEM and CFD models. Root mean square (RMS) errors for both the CFD and experimental data are considered against linear values.

2.4.1 Diffraction: Stationary WEC in Waves

The force on a WEC from the incident waves are the driving mechanism for the entire system. Fig. 2.9 shows the diffraction heave and surge excitation force coefficient Γ_i for various incident wave frequencies from experiments, linear FEM model and 30mm wave amplitude CFD simulations. Experimental RMS values are found to be $17.08 N/m$ and $12.79 N/m$ for heave and surge respectively with maximum differences of $33.59 N/m$ and $29.54 N/m$. The larger differences between experimental results and linear FEM appear near the peak point of interaction which from the statements in [35] is expected. The CFD results for the 30mm amplitude incident waves have RMS values for $9.40 N/m$ and $2.32 N/m$ for heave and surge respectively, positioning them more inline with the linear

theory, however for heave we note that the results near the peak forcing aligns with the trends of the experimental results. Extending the CFD model we can produce high-order incident waves which are outside of the linear regime. The transition to high-order wave profiles can be seen with the normalised wave amplitudes ($H/g\tau^2$) given in Table 2.5.

In Fig. 2.10 we see the force time-series associated with both heave and surge at

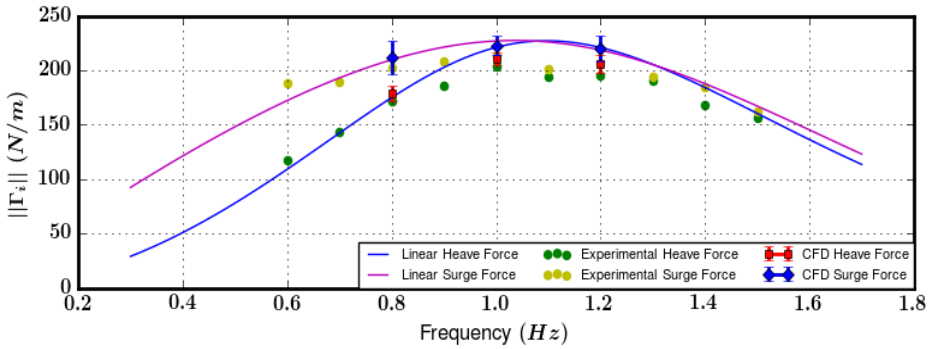

Fig. 2.9 The FEM, CFD and experimental excitation force coefficient Γ_i on a still submerged WEC in waves of various frequencies.

Table 2.5 High-order wave amplitudes produced in the CFD NWT. The values shown below can be cross referenced with Fig. 1.1.

$\frac{h}{g\tau^2}$	**Amplitudes** ($\frac{H}{g\tau^2}$)			
0.0391	0.00391	0.00521	0.00652	0.00782
0.0611	0.00611	0.00815	0.01019	0.01223
0.0880	0.00880	0.01174	0.01467	0.01761

frequencies, 0.8Hz, 1.0Hz and 1.2Hz and amplitudes 30mm, 40mm, 50mm and 60mm. In heave, Fig. 2.10(i), we can see a variation in the form of the forcing oscillation with increasing incident wave amplitude. At 0.8Hz, Fig. 2.10a increasing wave amplitude tends to slow the build up toward positive forcing and in turn shows a sharp decrease in the downward direction. This effect is lessened at higher frequencies but can still be seen in the force variations. Larger amplitudes appear to increase this effect. This peak shifting effect is quantified in Table 2.6 giving the percentage of a single period in the transition from the extreme upward to downward forcing. We can see that the transition time at all frequencies decreases with amplitude and the effect is more distinct at low frequencies. In surge, Fig. 2.10(ii), this extrema shifting is still visible but not as pronounced as in the heave case. The faster transition in this case occurs from upstream to downstream

Table 2.6 Percentage of time per period spent in the transition from upward to downward heave force at various amplitudes and frequencies.

Frequency (Hz)	**Transition Percentage** Amplitude (mm)			
	30	40	50	60
0.8	47.53	44.93	42.17	39.31
1.0	47.24	46.84	42.84	41.31
1.2	48.42	46.77	45.16	43.67

Table 2.7 Percentage of time per period spent in the transition from upstream to downstream surge force at various amplitudes and frequencies.

Frequency (Hz)	**Transition Percentage** Amplitude (mm)			
	30	40	50	60
0.8	49.76	48.55	46.92	46.32
1.0	47.19	46.61	48.13	47.95
1.2	48.91	48.11	47.54	45.37

force extrema with a more gradual opposite transition. Table 2.7 shows the transition percentages for the surge forcing.

Apart from the changes in the force oscillations, the excitation force coefficient amplitude differences are of great importance to WEC design. The variations in normalised force amplitude with increasing wave amplitudes are shown in Fig. 2.11. At an incident wave frequency of 0.8Hz, Fig 2.11a, the CFD results show distinct variations in force amplitude with increasing wave amplitudes. Upward heave shows a near linear increase in peak forcing, while the reverse is true for the downward case. In surge there appears to be a small imbalance between upstream and downstream forcing at low amplitudes which decreases with amplitude. In each case linear FEM results are in good agreement with CFD across the wave amplitude range and the mean amplitude RMS error values are given in Table 2.8.

In Fig. 2.11b we see the force amplitudes on the sphere from a wave of 1.0Hz which is

Table 2.8 Mean peak and trough Γ_i RMS error against linear values.

	Wave Amplitude (mm)			
	30	**40**	**50**	**60**
Heave	9.40	23.60	25.49	28.75
Surge	2.31	13.94	13.10	13.72

near the resonant frequency of the system. The trends in CFD results at this frequency are dissimilar to the previous case in Fig. 2.11a. FEM shows near identical values for both heave and surge orientations but while CFD downstream surge results follow FEM predictions closely, upstream values diminish with amplitude. The heave results are

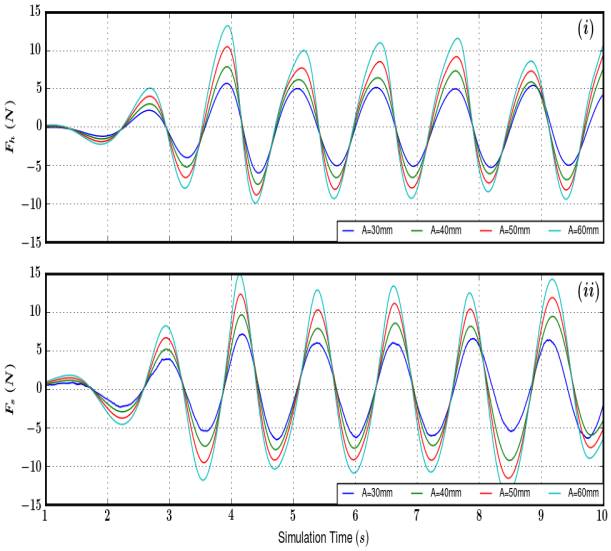

(a) Heave (i) and surge (ii) force time-series acting on the still WEC in 0.8Hz incident waves.

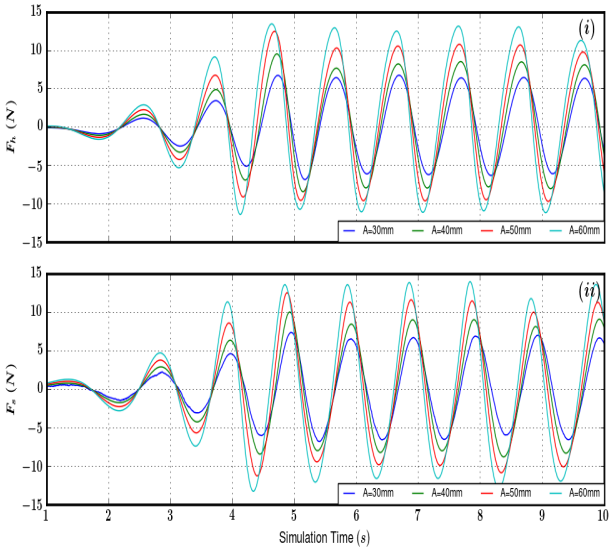

(b) Heave (i) and surge (ii) force time-series acting on the still WEC in 1.0Hz incident waves.

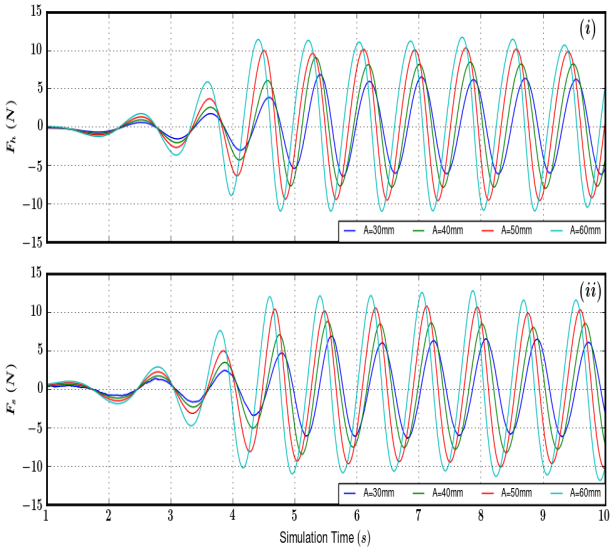

(c) Heave (i) and surge (ii) force time-series acting on the still WEC in 1.2Hz incident waves.

Fig. 2.10 Heave and surge force time series on a still submerged sphere in (a) 0.8Hz, (b) 1.0Hz and (c) 1.2Hz incident waves.

consistently below what FEM predicts. The upward forcing tends to remain constant over all amplitudes but there appears to be a near linear drop in downward forcing. This can be described as an increase in the drifting forces on the sphere with high order incident waves. The sphere forcing in this case is highly dependent on wave amplitude and will

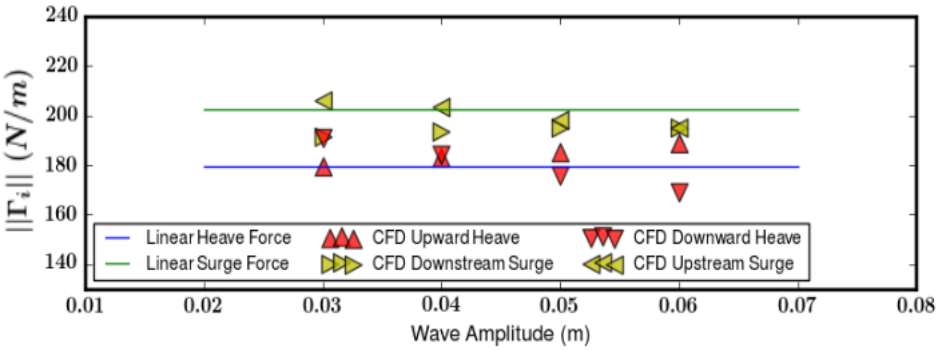

(a) Excitation force coefficient amplitudes for incident wave frequency 0.8Hz.

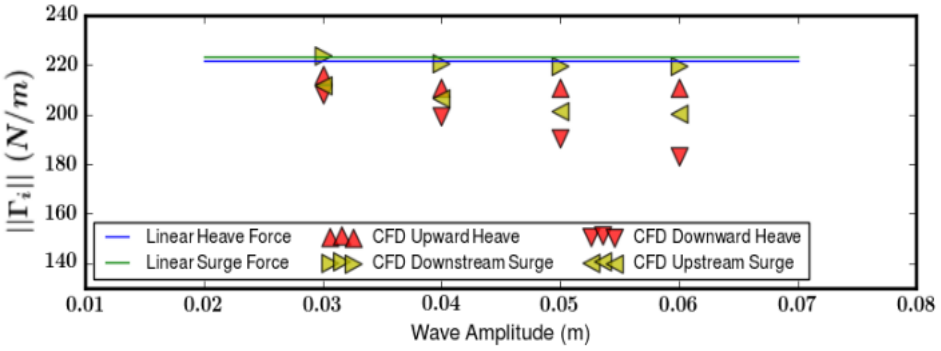

(b) Excitation force coefficient amplitudes for incident wave frequency 1.0Hz.

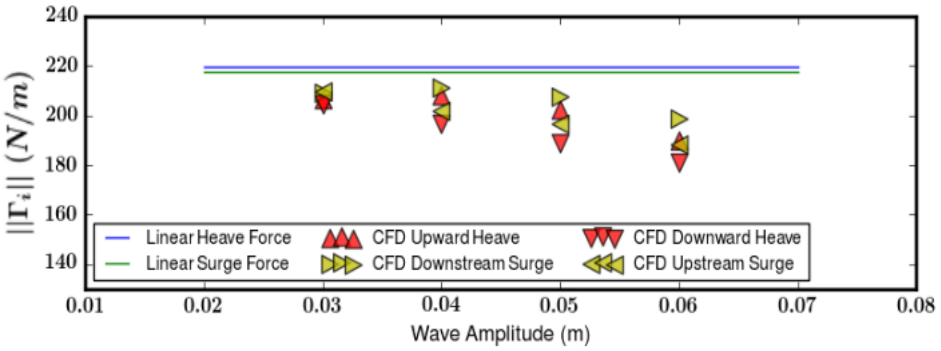

(c) Excitation force coefficient amplitudes for incident wave frequency 1.2Hz.

Fig. 2.11 Comparisons of FEM and CFD heave and surge excitation force coefficients on a single submerged WEC with increasing incident wave amplitudes.

react differently due to the variations in the excitation force.

Fig. 2.11c shows the force amplitude values on the sphere for a 1.2Hz incident wave frequency. The variations seen in this case show results in contrast to the previous two cases. While both heave and surge force values are below FEM predictions at all

amplitudes, we see a decrease in the peak forcing with increasing wave amplitudes in both orientations. This represents an overall drop in forcing with increased wave amplitude at a frequency above the system resonance. Of note, the spread between the forcing extrema do not appear to diverge as they do in the 1.0Hz case suggesting smaller drift forces produced from this frequency.

These excitation force variations with wave amplitude may be linked to the resonance frequency of the system. The incident wave frequencies of 0.8Hz, 1.0Hz and 1.2Hz were chosen to straddle the FEM predicted resonance frequency of the system and we see that CFD forces tend to show differing trends above near and below this regime. More work is needed however to show if there is any generality to the forcing trends around the system resonance and these effects would be largely device dependent. With CFD however, we are able to analyze in more detail the interactions the sphere has with the environment in order to better understand the deviations from linear predictions.

The interaction between the free surface and the sphere is clearly affected by the wave amplitude. At high amplitudes a breaking wave appears above the sphere during the trough period of the wave. The development of this breaking wave is shown in Fig. 2.12. This free surface effect is a likely candidate for the variations in sphere forcing seen at large amplitudes. At low amplitudes the interaction with the free surface is minimal and so the linear description of the excitation force is adequate as shown in Fig. 2.11, however if applying linear results at large amplitudes, a point of error will be the breaking wave on the sphere which cannot be captured by a linear model. Of note are the flows generated between the sphere and free surface as the wave passes. These flow speeds exceed the maximum orbital velocities of the passing waves and could be utilised in a constructive way.

2.4.2 Summary: Diffraction Problem

The results from the diffraction study have shown the limitations of the linear modelling approach when compared to CFD and experimental results. Experiments show particularly near the FEM predicted peak forcing, distinctly lower values which also appear in CFD heave forcing results. As the wave amplitude increases however, the variation in the force appearing on the sphere is also dependent on the wave frequency complicating any performance study and requires more work to discover general trends near the FEM predicted system resonance. It was observed that the transition time between forcing extrema is also affected by the wave amplitude. A breaking wave may be a contributor to this effect, largely dependent on the WEC geometry and not simply a result of the inclusion of viscosity or turbulence in the model. From Fig. 2.12 we can see that the flows

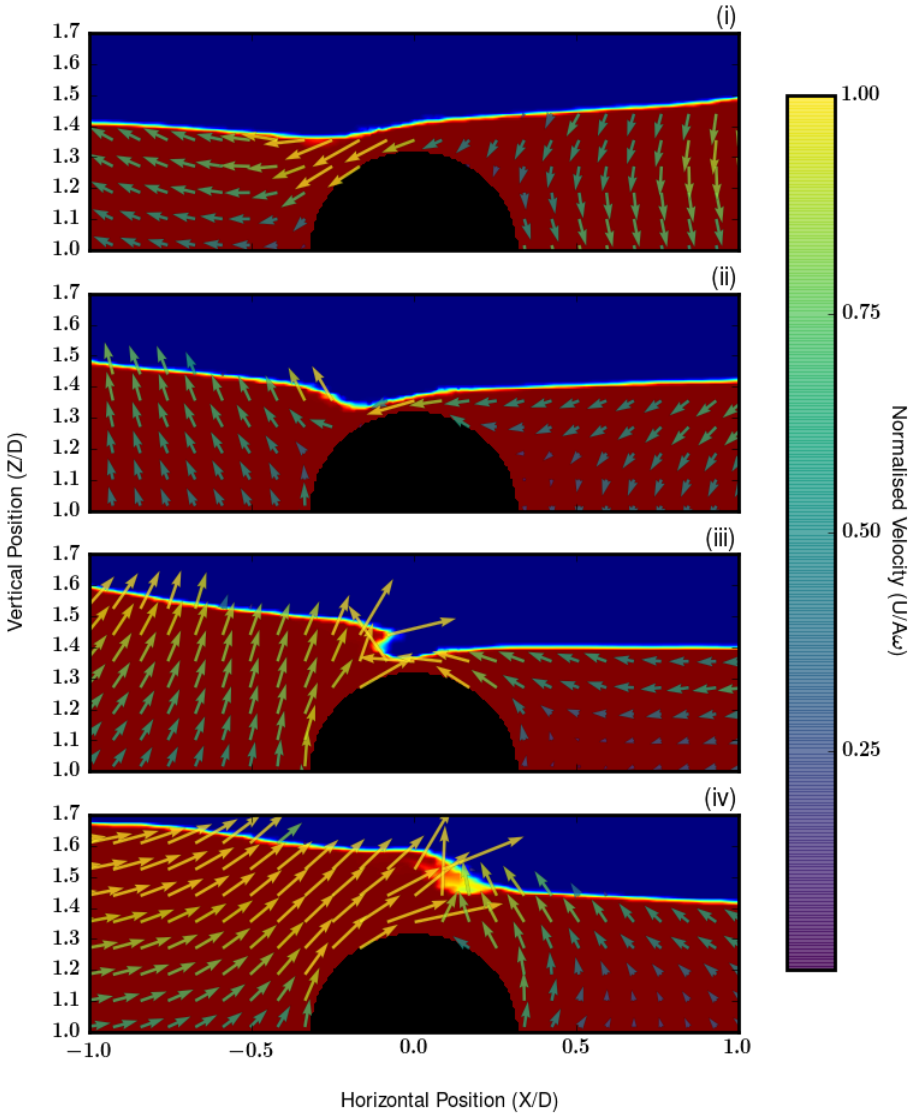

Fig. 2.12 The breaking wave produced near the sphere with a 60mm amplitude incident waves. Corresponding times of each snapshot are $(i) = 0.0s$, $(ii) = 0.1s$, $(iii) = 0.2s$ and $(iv) = 0.3s$.

generated over the WEC are dictated by the shape of the WEC suggesting that this effect would be subject to Froude scaling. This breaking wave behaviour would thus be present for full scale devices in the appropriate wave fields. Considering the effect of viscosity with the Keulegan-Carpenter number we would see a decrease in its importance due to the inverse WEC length scale dependence.

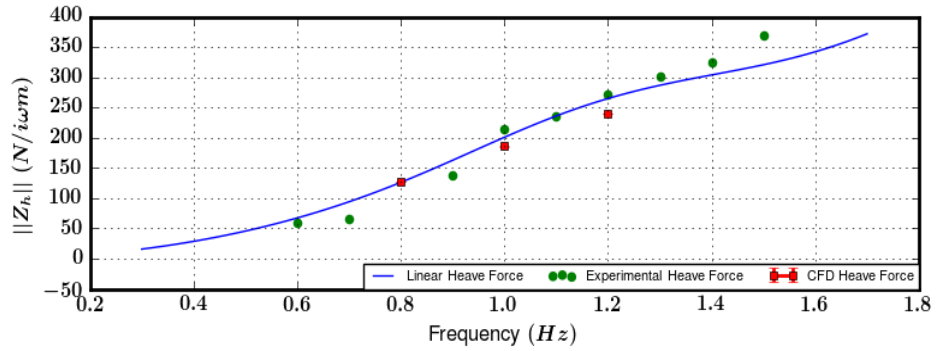

Fig. 2.13 FEM, CFD and experimental heave radiation impedance coefficients on a heaving WEC in calm water.

From these results we can argue that linear modelling performs well for spherical WECs when the wave amplitudes are indeed small, capturing the hydrodynamics forcing trends over the specific frequency range. There is however inaccurate force amplitude predictions near resonance which is expected. For small incident wave amplitudes, CFD shows results more similar to measured experimental values and extending to high amplitude waves shows free surface interactions which would occur at full scale.

2.4.3 Radiation: Heaving Spherical WEC in Calm Water

The radiation impedance coefficient Z_{ij} is linked to the added mass and radiation damping coefficients which are necessary when calculating the performance of a WEC. In this section we analyze the radiation impedance from a heaving WEC and it's variation with increasing oscillation amplitudes. The WEC is forced to heave at frequencies of 0.8Hz, 1.0Hz and 1.2Hz with oscillation amplitudes of 30mm, 40mm, 50mm and 60mm in CFD and 30mm in experiments. Unlike the diffraction case, Section 2.4.1, the oscillations remain sinusoidal and do not include high-order frequency components present in high-order waves. In this way we continue to mimic the linear FEM and experimental approaches.

Fig. 2.13 shows all predictions for Z_{hA} from FEM, low amplitude CFD and experi-

Table 2.9 Mean peak and trough radiation impedance coefficient amplitude RMS error against linear values.

	Oscillation Amplitude (mm)			
	30	**40**	**50**	**60**
Heave	14.65	5.09	10.40	18.64

Table 2.10 Percentage of time per period spent in the transition from upward to downward heave force at various amplitudes and frequencies.

Frequency (Hz)	**Transition Percentage** **Amplitude** (mm)			
	30	40	50	60
0.8	45.73	43.34	39.46	34.76
1.0	49.35	42.20	39.17	38.45
1.2	46.09	45.78	42.13	39.55

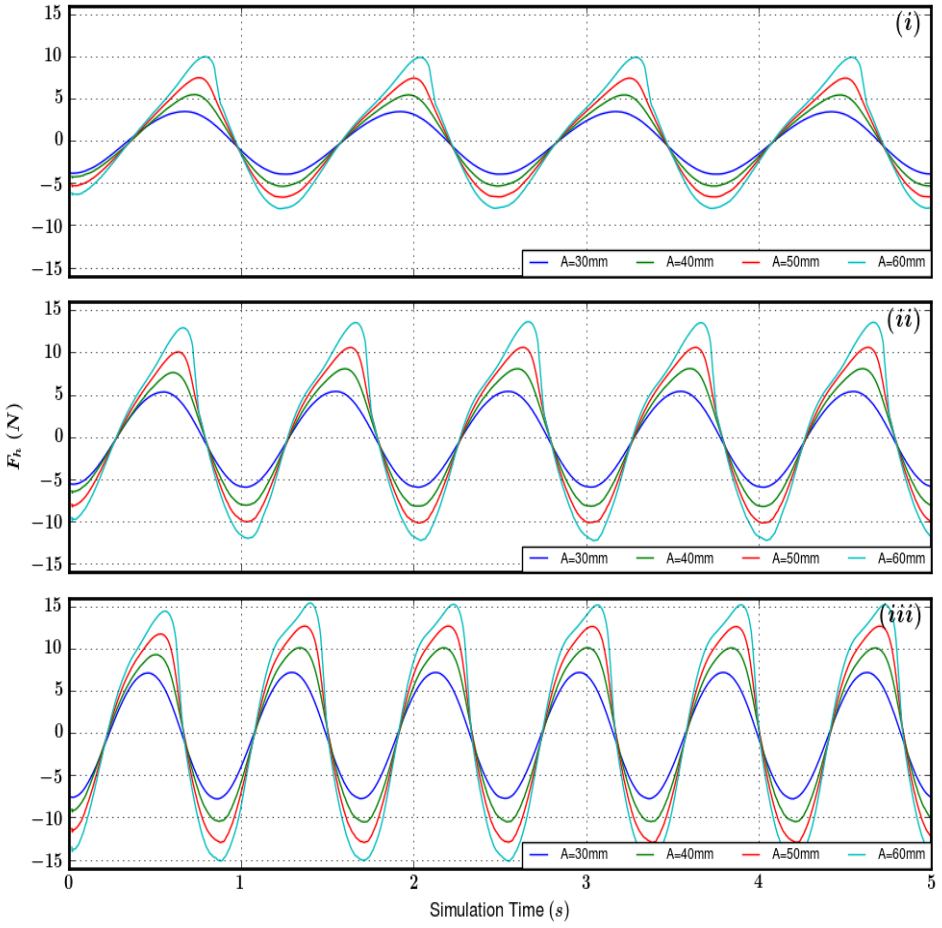

Fig. 2.14 Heave force time-series for the heaving WEC in calm water. Oscillation frequencies are (i) 0.8Hz, (ii) 1.0Hz and (iii) 1.2Hz.

mental modelling techniques. Overall there is close agreement between each method of modelling the heaving WEC with the RMS error for experimental results being $22.69 N/m$ with the RMS values for CFD given in Table 2.9. The time-series, Fig. 2.14 shows a consis-

tent fluctuation in the peak upward forcing at all frequencies as the total force increases due to increasing oscillation amplitude. As in the diffraction case this causes a change in the transition time between peak upward and downward forcing. Table 2.10 shows the transition percentage for the forcing on the heaving sphere. We can see that low frequencies are affected the most by this fluctuation similar to the results from the diffraction study.

Fig. 2.15 shows the force extrema at various frequencies and oscillation amplitudes. At 0.8Hz, Fig. 2.15a we can see the steady increase in the upward forcing which coincides with the fluctuation seen in Fig. 2.14. The downward force however is a consistent match with the linear amplitude independence trend. Similar findings appear at 1.0Hz, Fig 2.15b. The peak upward forcing shows a steady increase with amplitude while the downward force remains constant and in agreement with linear amplitude independence. Between these two oscillation frequencies we note that the upward forcing at low amplitudes is below FEM predictions. A similar result is seen at 1.2Hz, Fig. 2.15c. The upward forcing does not continue to increase with amplitude however, as was the case in the previous two cases. The downward forcing continues to closely agree with the linear trends while the upward forcing results from CFD are consistently below FEM predictions.

As with the diffraction case we can attribute the forcing fluctuations to the interaction between the heaving WEC and the free surface. We can see consistently for the heaving WEC that as the oscillation amplitudes increase it begins to influence the deformation of the free surface, drawing it into contact with the WEC. This void is rapidly filled by fluid as the WEC moves deeper creating a jet of fluid moving upward. A vertical profile of this process is shown in Fig. 2.16 with the velocity field $U/A\omega$. As the WEC moves downward from the peak elevation of the motion fluid is drawn past itself and the free surface momentarily contacts it's surface. Quickly, the fluid surrounding the WEC flows inward to fill the void and once filled residual fluid momentum forces the small jet. This is a clear nonlinear effect and is likely the main contributor to the behaviour seen in the force time-series in Fig. 2.14. For the heaving WEC, CFD shows that this free surface interaction which cannot readily be captured with linear modelling techniques or quantitatively measured in experimental testing but is an important dynamic generated by the motion of the WEC.

2.4.4 Summary: Heaving Radiation Problem

The results from the study of a heaving WEC have shown aspects of the problem which are not captured by linear modelling. At low oscillation amplitudes, CFD produces results which are in agreement with linear FEM predictions but show differences between upward and downward forcing characteristics with increasing oscillation amplitudes. CFD down-

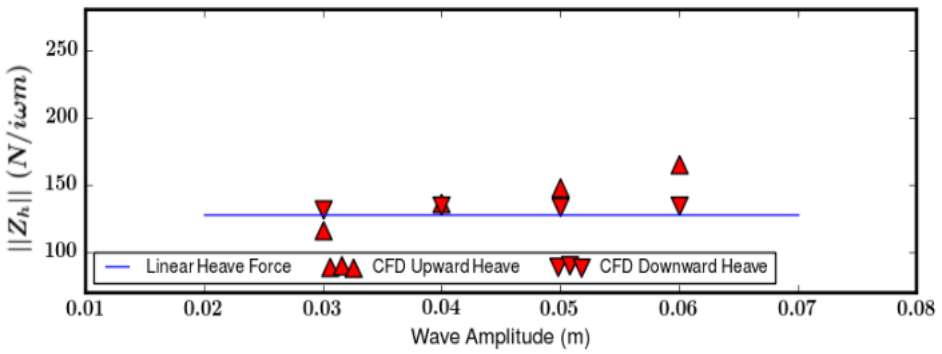

(a) Radiation impedance coefficient amplitudes for heaving frequency 0.8Hz.

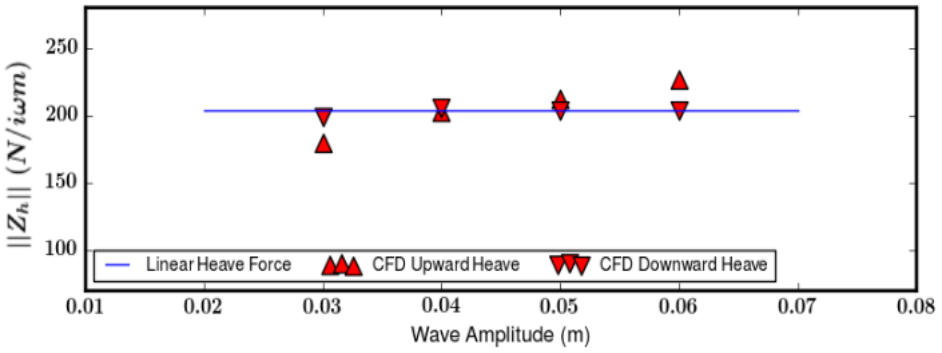

(b) Radiation impedance coefficient amplitudes for heaving frequency 1.0Hz.

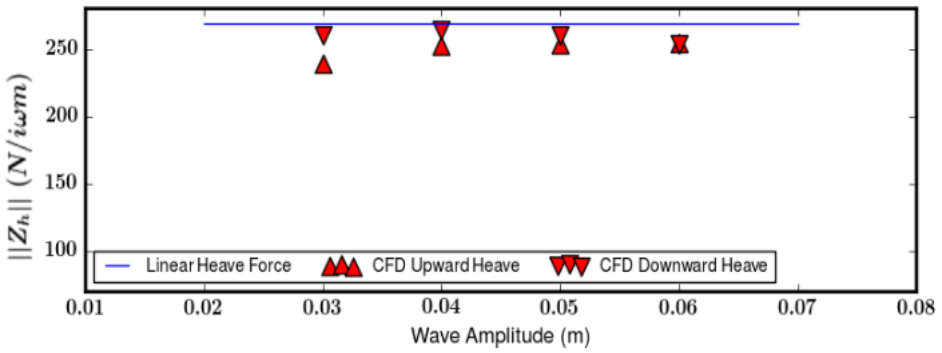

(c) Radiation impedance coefficient amplitudes for heaving frequency 1.2Hz.

Fig. 2.15 Comparisons of FEM and CFD radiation impedance coefficient on a single submerged heaving WEC with various oscillation amplitudes.

ward forcing match closely with FEM at all oscillation amplitudes and frequencies while upward forcing shows distinct deviations due to the interaction between the WEC and the free surface. This interaction is, like the diffraction case dependent on the dimensions of the WEC itself, which would make it scale to full size devices and similar fluid jets have

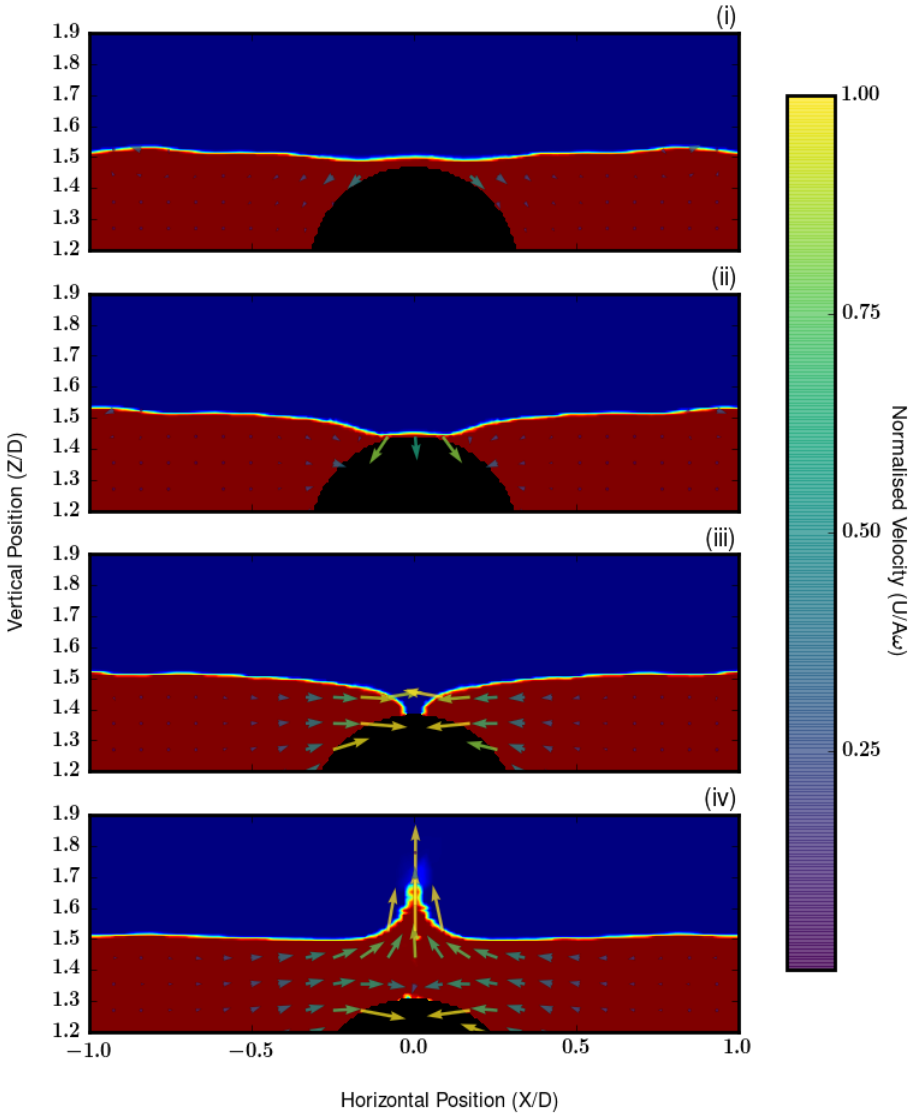

Fig. 2.16 Free surface interaction with the heaving WEC of oscillation amplitude of 60mm and frequency 1.0Hz. Corresponding times of each snapshot are $(i) = 0.0s$, $(ii) = 0.08s$, $(iii) = 0.16s$ and $(iv) = 0.25s$.

been reported in experiments of fully active devices [54], however with the WEC actively moving in waves the influence due to the coupling between diffraction and radiation makes it's origin less clear. This study shows the importance of free surface interactions which directly effect the added mass and radiation damping values and ultimately PTO characteristics.

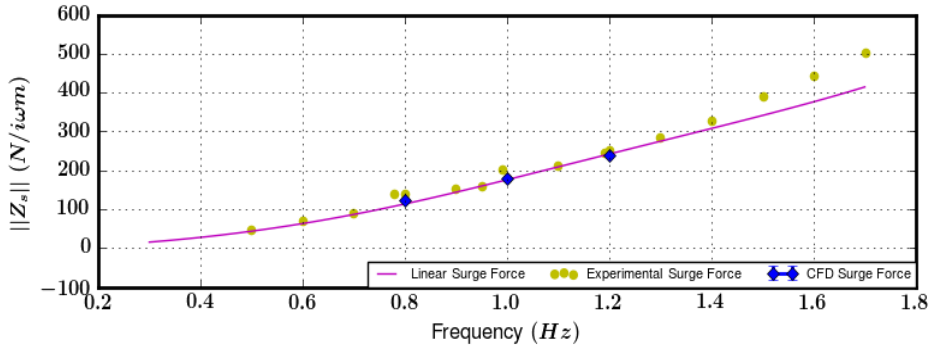

Fig. 2.17 FEM, CFD and experimental surge radiation impedance coefficient on a surging WEC in calm water.

2.4.5 Radiation: Surging Spherical WEC in Calm Water

In this section we analyze the radiation problem for a surging WEC. The WEC is forced to surge at frequencies 0.8Hz, 1.0Hz and 1.2Hz with oscillation amplitudes of 30mm, 40mm, 50mm and 60mm in CFD and experimentally with an amplitude of 30mm. This study mirrors that done for the heaving sphere differing only by the orientation of the oscillation.

Fig. 2.17 shows the 30mm amplitude CFD and experimental results against the FEM model. We can see that CFD produces results which are in agreement with the FEM model, where the RMS errors are given in Table 2.11. The RMS for experimental results is $33.45 N/m$, however from Fig. 2.17 we can see that for high frequencies beyond what was tested in CFD there is a general divergence of the force amplitude results between FEM and experiments. Excluding the results for 1.5Hz+ experimental values we have a considerable drop in the RMS error to $11.26 N/m$. The surging WEC forcing results then show significantly close agreement between each form of modelling compared to the heave case. Fig. 2.18 shows the time-series for the CFD forces at various frequencies

Table 2.11 Mean peak and trough force amplitude RMS error against linear values.

	Oscillation Amplitude (mm)			
	30	**40**	**50**	**60**
Surge	5.43	5.63	6.14	7.07

and amplitudes. For this motion we do not see any clear deformation of the sinusoidal nature of the force oscillation which is reflected in consistent transition percentages shown in Table 2.12. In Fig. 2.19 we can see across all frequencies and amplitudes that there is consistent agreement with FEM forcing trends and from this we can argue that

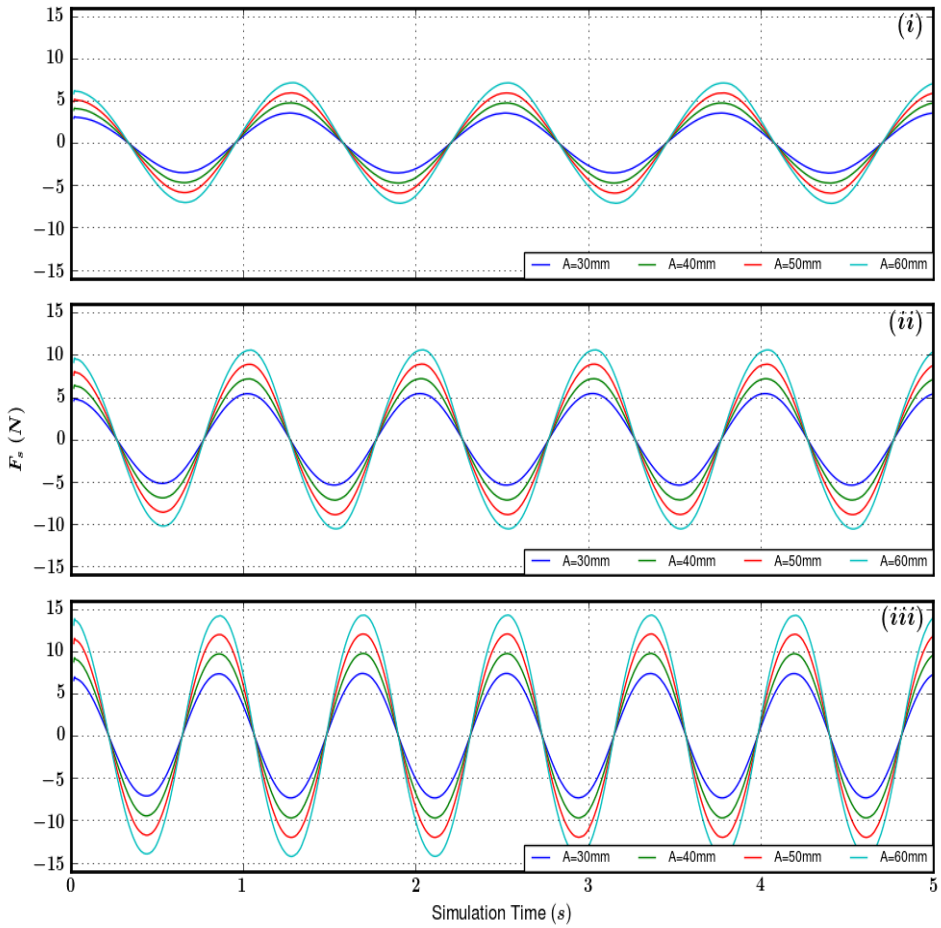

Fig. 2.18 Surge force time-series for the surging WEC in calm water. Oscillation frequencies are (i) 0.8Hz, (ii) 1.0Hz and (iii) 1.2Hz.

Table 2.12 Percentage of time per period spent in the transition from upstream to downstream surge force at various amplitudes and frequencies.

Frequency (Hz)	**Transition Percentage** **Amplitude** (mm)			
	30	40	50	60
0.8	50.55	49.53	49.80	50.16
1.0	51.07	51.71	49.10	51.74
1.2	50.01	49.77	50.47	49.27

the radiation problem for a surging WEC remains within the linear regime for all cases studied here.

Fig. 2.20 shows an example of velocity fields, $U/A\omega$ around the surging sphere for an oscillation amplitude of 60mm and 1.0Hz frequency. We can see that for the surge motion the free surface does not interact with the WEC as dramatically as it does in the diffraction or heaving WEC cases. This emphasises the impact of the free surface on the WEC forcing and why the results in this case conforms well to linear trends. The source of the nonlinear behaviour from the diffraction and heaving radiation cases were prominently free surface effects and so in the surge case the forcing tends to behave in a linear manner as there is minimal free surface interaction. No breaking waves or otherwise irregular behaviour appears at the free surface disrupting the fluid flows causing irregularities in the forcing. At low frequencies then, linear modelling aligns well with experimental and CFD predictions of the forcing and fluid behaviour surrounding the WEC.

2.4.6 Summary: Surging Radiation Problem

The CFD results for the radiation from a surging WEC have shown that the conditions studied here are well represented by linear models. The forces appearing on the WEC are consistent with the FEM model and experimental results and show little variation with increased oscillation amplitude. There is minimal interaction between the WEC and free surface which induce irregular forcing in both the diffraction and heaving radiation cases. Under the CFD conditions studied here, the surging sphere remains well within the capabilities of linear modelling.

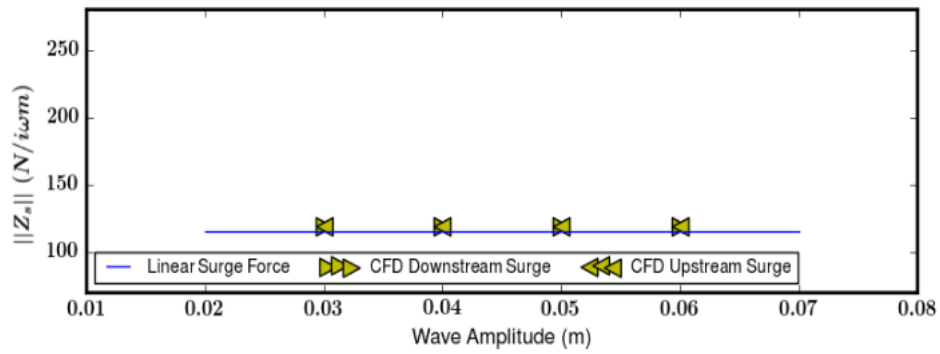

(a) Radiation impedance coefficient amplitudes for surging frequency 0.8Hz.

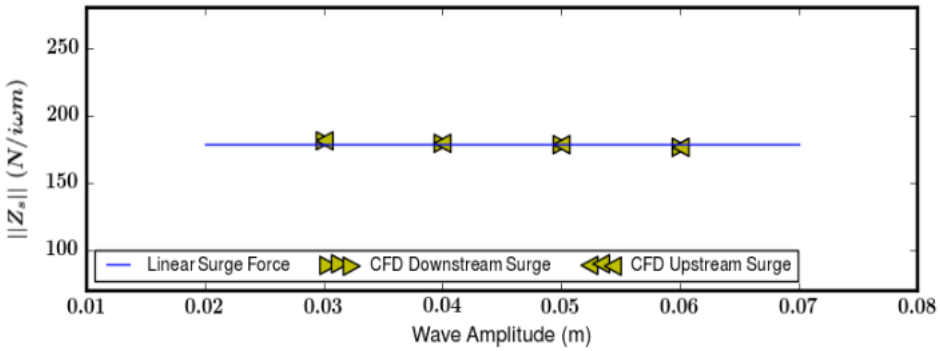

(b) Radiation impedance coefficient amplitudes for surging frequency 1.0Hz.

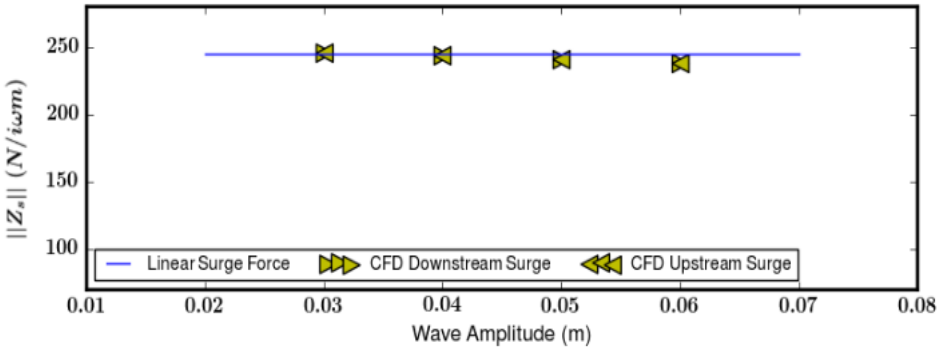

(c) Radiation impedance coefficient amplitudes for surging frequency 1.2Hz.

Fig. 2.19 Comparisons of FEM and CFD radiation impedance coefficient on a single submerged surging WEC with various oscillation amplitudes.

2.5 Conclusion

This work applies a 3D nonlinear, turbulent RANS VOF model to simulate a single submerged spherical WEC operating in both heave and surge. Four regular incident waves and sphere oscillation amplitudes of 30-60mm with frequencies of 0.8-1.2Hz were con-

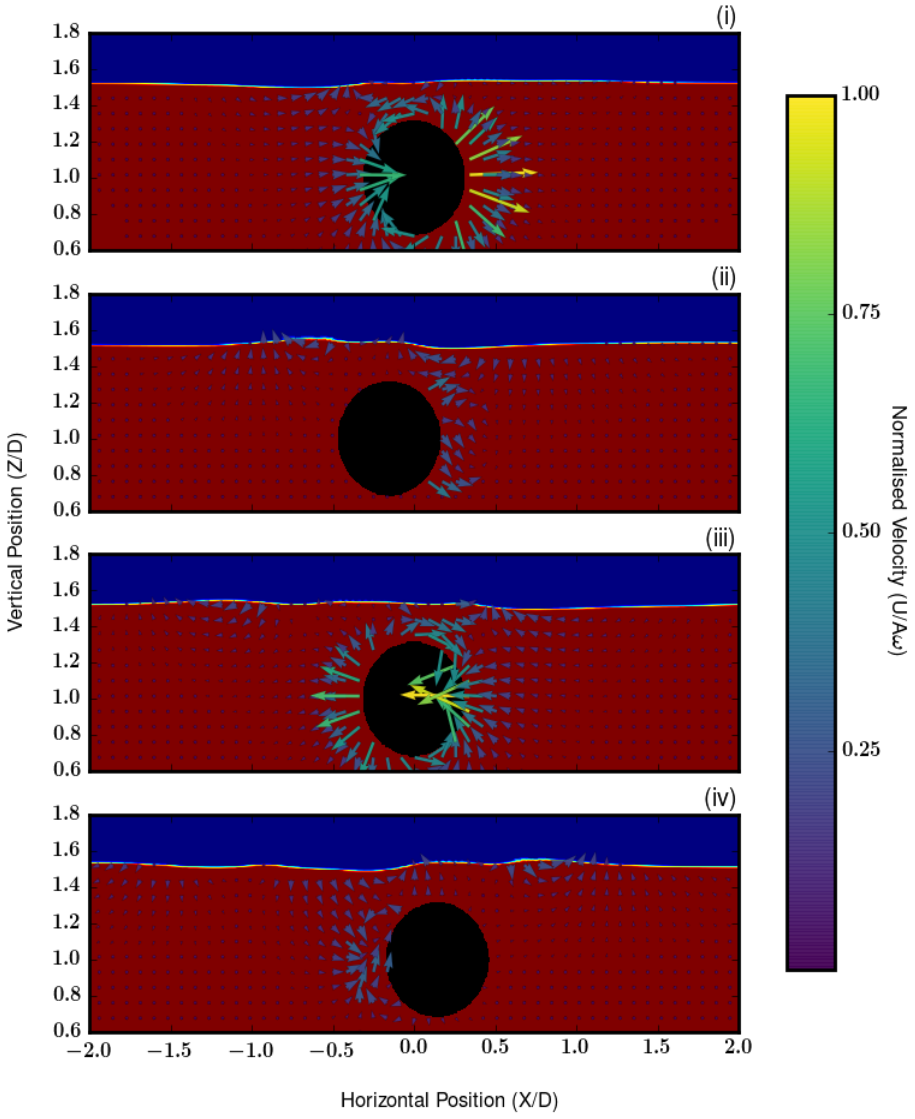

Fig. 2.20 Velocity fields, $U/A\omega$ around the sphere at various points in the oscillation period.

sidered in CFD. A linear FEM model was adapted to the problem of a generic submerged spherical WEC and results for the hydrodynamic coefficients are presented. Experiments performed at the AMC [53, 46] mirroring the cases studied in both CFD and FEM were used to validate and quantify the errors in numerical values. This novel approach to the study of the hydrodynamics of a WEC by invoking the linear separability of the problem has highlighted free surface effects as a key contributor to nonlinear effects on a submerged WEC. These effects have been seen in full scale numerical testing and could be predicted

by applying Froude scaling for a spherical WEC, however would be largely dependent on a WEC design under consideration.

Chapter 3

Nonlinear Modelling of the Diffraction Problem for Arrays of Generic Wave Energy Converters

This chapter is under review for publication and is in press for the Journal of Renewable Energy at the time of writing. The journal publication here has been edited, altering the introduction, theory and conclusion sections but is otherwise unchanged from the original article.

3.1 Abstract

The knowledge and understanding of individual wave energy converter (WEC) performance is steadily advancing to the point where full scale WECs are being deployed in various testing grounds around the world. A lesser understood aspect of this technology is their combined interactions when positioned in close proximity to each other. In a situation such as this, the diffracted waves from one WEC to another can influence the excitation forces for better or worse effecting the overall power generated. This problem has largely been addressed using linear modelling techniques giving optimised array configurations for various WECs and sea conditions. These studies are all limited by the linear wave assumptions and neglect the non-linear effects of viscosity and turbulence. The current study applies a fully non-linear CFD model to investigate WEC array performance. The approach applied here assumes solution superposition to analyze the diffraction and radiation forces independently. The following work shows the solution for the diffraction problem for arrays of two and four fully submerged spherical WECs. CFD findings are compared against linear model results for validation and a clear depiction of

nonlinearities. This work shows the onset of free surface interactions and the changes to WEC excitation forces which greatly influence performance, mooring and configuration stability. The outcomes show the limitations of linear modelling and highlight the need for more detailed analysis.

3.2 Introduction

This work extends the CFD model employed to study both the heaving and surging WECs presented in [9, 10] which modelled both the diffraction and radiation problems for a complete description of a single generic WEC. In the diffraction case, breaking waves were found to form as the amplitude of the incident wave increased. These breaking waves were found to alter the sinusoidal behaviour of the excitation forces in both heave and surge. The onset of breaking waves was found to be dependent on the proximity of the WEC to the free surface and tended to occur for lower incident wave frequencies. The results however show that the normalised excitation force decreases with incident wave amplitude meaning that less of the power available in the wave is translating onto the WEC and that a linear description of the systems is inaccurate.

The present study extends the work on a single device and analyses generic spherical WEC arrays of both two in a row and four in a square configurations at various spacings between devices. Incident wave frequency and amplitudes are altered to study the excitation force on each WEC in the array. The outcomes from this work are compared to linear FEM results and show the excitation force on the combined array in various array configurations.

3.3 The CD-Adapco Star-CCM+ Model and Computational Mesh

3.3.1 The Numerical Wave Tank

The CFD numerical wave tanks (NWT)s used in the present study all make use of the problem symmetry thus eliminating half of the fluid domain and the benefit of shorter simulation times. The NWTs are an extension of those using in Bharath *et al.* [10] expanded to include multiple spheres. As this work focuses on the diffraction problem, the WECs remain still throughout the study presented in this chapter as described in Section . Comparisons of the results from CFD to measured experimental values in diffraction showed < 8% RMSE giving significant confidence in the NWT developed. Wave breaking overtop of the WEC seen qualitatively in experiments was also well represented in CFD outputs. The sphere diameter (SD) for all cases are 250mm. For the simulations of two spheres in a row, the sphere separations (S_s) are 500, 750 and 1000mm shown in Fig. 3.1a. A numerical symmetry plane cuts the spheres along the center axis with a 16 SD distance to the side wall of the NWT. A wave damping zone is applied 16 SD downstream of the

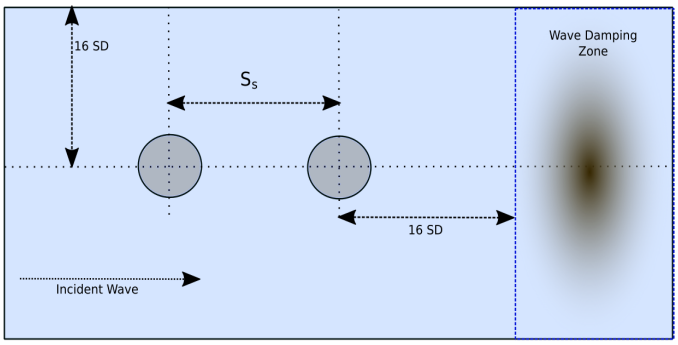

(a) The configuration of the two WECs in a row wave tank.

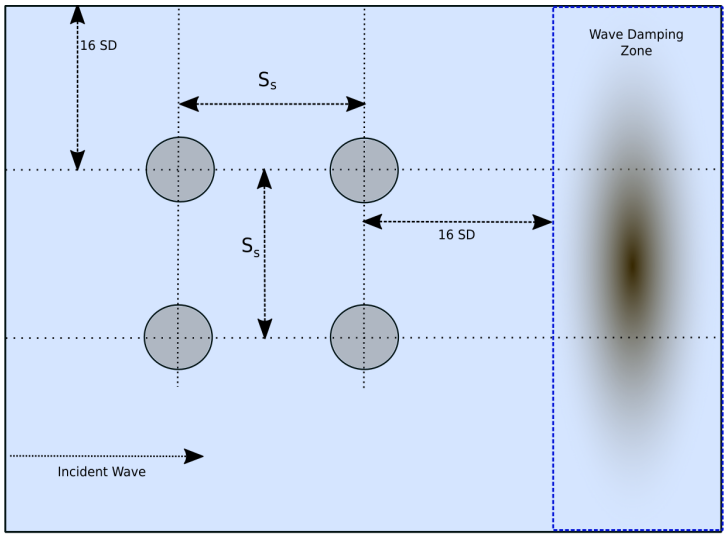

(b) The configuration of the four WECs in a square wave tank.

Fig. 3.1 The two and four WEC array configurations studied in this work.

second sphere, shifting in each simulation to be a distance $S_s + 16$ SD downstream on the first sphere in all cases.

The four spheres in a box configuration is constructed in a similar fashion to the two in a row case. The symmetry plane however is placed a distance $(1/2)S_s$ from the centerline of the spheres. The sidewall and the wave damping zone are placed in the same fashion as the previous case.

3.3.2 The Computational Meshes

The computational meshes used in this study are an extension of the ones developed in [9, 10] as the meshes applied here follow the same restrictions and sizing. The mesh characteristic $M_c \leq 2.5$ for each wave condition is used to ensure accurate wave propaga-

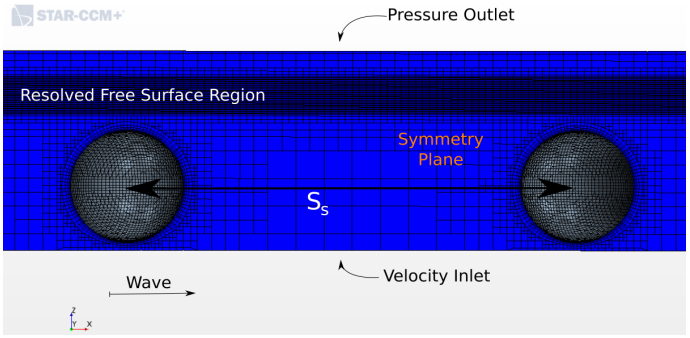

(a) A side view of the numerical mesh in the two WEC NWT.

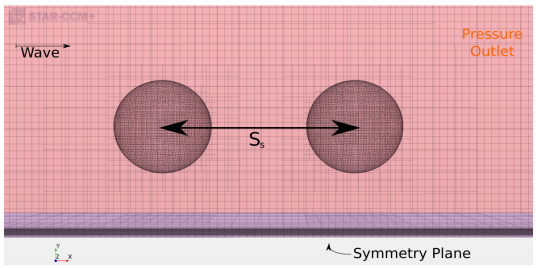

(b) A top down view example of the numerical mesh used in the four WEC NWT.

Fig. 3.2 Examples of the numerical meshes used in this study.

tion. Examples of the two and four sphere meshes are given in Fig. 3.2. For both domains numerical velocity inlets are used on the NWT base, upstream boundary and sidewall parallel the symmetry plane which divides the domain. The downstream boundary and NWT top are set as numerical pressure outlets. The boundary conditions are set using the VOF wave functionality within Star-CCM+ generating the time dependent hydrostatic pressure, volume fraction and component velocity values.

The symmetry plane in the two WEC case, Fig. 3.2a divides the domain down the center line of the WECs. This reduces the computational requirements considerably and the cell counts for these simulations are at most 6.5 million, varying slightly with the separation of the WECs. In the four WEC case the symmetry plane is place a distance of $(1/2)S_s$ away from the center line of the WECs. This allows for all four WECs to be simulated while still reducing the computational domain and requirements. Due to the increased area in the domain, the computational cells in the four WEC simulations are at most 9 million, which varies with the value of S_s.

3.4 Results and Discussion

3.4.1 Two Wave Energy Converters

In this section we investigate the excitation force amplitude Γ_i and interaction between two submerged WECs in a row. Both WECs are identical in size and depth. The S_s used here are 1000mm, 750mm and 500mm with incident wave frequencies of 1.0-1.6Hz.

In Figs. 3.3 and 3.4 the linear, amplitude independent FEM predictions of Γ_i of the two in a row WEC array and the single WEC case are shown. It can be seen that in each case there are force amplitude gains on the downstream WEC while there are losses on the upstream WEC with a noticeable increase in variability at high frequencies. For Γ_s we can see a distinct shift in resonance to higher frequencies compared to the single WEC case. For Γ_h a resonance frequency shift is not as apparent while it is clear that the presence of two WECs give a distinct increase to the forcing experience by the downstream sphere.

Nonlinear Excitation Forces

Γ_i for any WEC system is what drives energy conversion and therefore are important in estimating the performance of a WEC system. In this section we investigate Γ_i on two spherical WECs in a row as shown in Fig. 3.1a. Figures 3.3 and 3.4 show the heave and surge excitation forces, Γ_h and Γ_s for the linear FEM model of a single and two WECs in a row along with the CFD results for the two WEC array at all wave heights. Γ_i calculated from CFD in general show similar values compared to FEM but show particular differences in particular cases. Root mean square errors calculated between linear and CFD values for each wave amplitude are shown in Appendix Table. B.1 for heave and Table B.2 for surge.

For the WEC separation of 500mm, the Γ_h for a 60mm wave height shows a similar trend to that from linear modelling. Larger forcing appears on the downstream WEC consistently with increasing frequency although not the increase linearly expected. With increasing wave height, CFD shows a decrease in Γ_h appearing on the downstream sphere. For wave heights of 80mm and 100mm (Fig. 3.3d and 3.3g) we note that Γ_h on both WECs is similar at each frequency. The standard deviation of the peak Γ_h values from CFD show an increase toward higher frequencies as well as a notable decrease with wave height particularly on the down stream WEC. Γ_s for WECs with $S_s = 500$mm shows distinctly different behaviour compared to linear results. At $f = 1.0$Hz, (Figs. 3.4a,3.4d and 3.4g), we see opposite behaviour to that expected from linear modelling where larger Γ_s values appear on the upstream WEC consistently at all wave heights with relatively large variability on both WECs. High frequencies $f = 1.4$ and 1.6Hz, CFD shows not

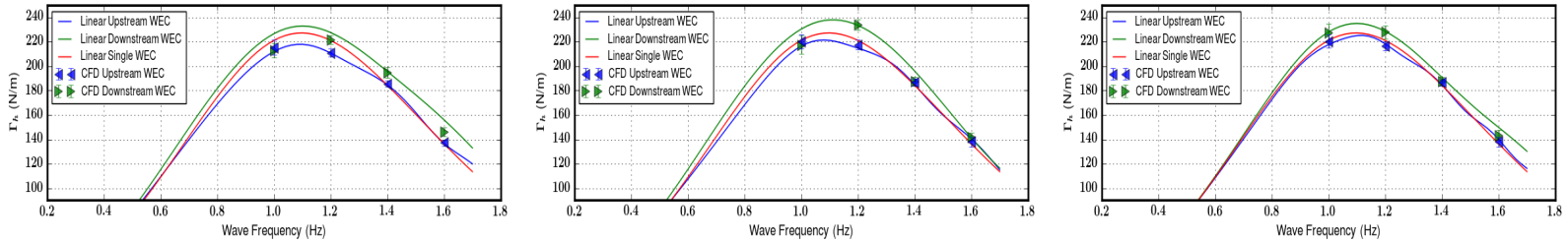

(a) H=60mm and S_s =500mm.

(b) H=60mm and S_s =750mm.

(c) H=60mm and S_s =1000mm.

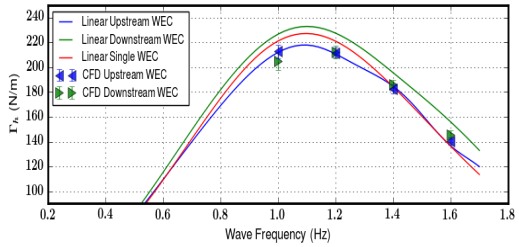

(d) H=80mm and S_s =500mm.

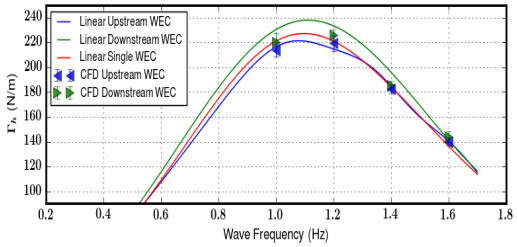

(e) H=80mm and S_s =750mm.

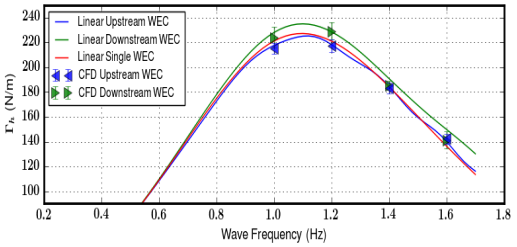

(f) H=80mm and S_s =1000mm.

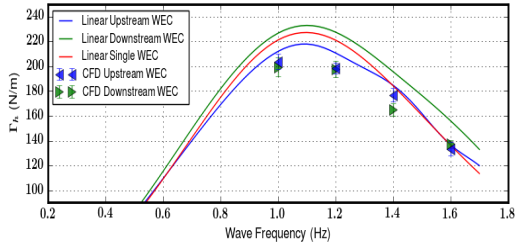

(g) H=100mm and S_s =500mm.

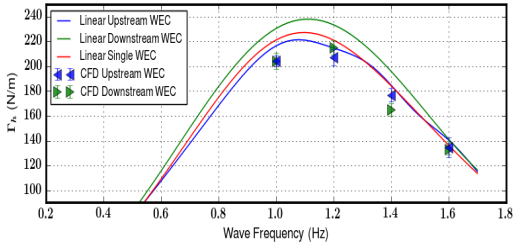

(h) H=100mm and S_s =750mm.

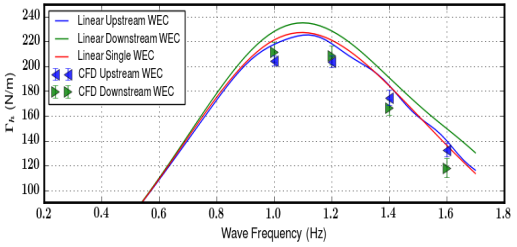

(i) H=100mm and S_s =1000mm.

Fig. 3.3 Comparisons of linear FEM and CFD heave Hydrodynamic forcing on two submerged spheres in a row with various incident wave heights and separations.

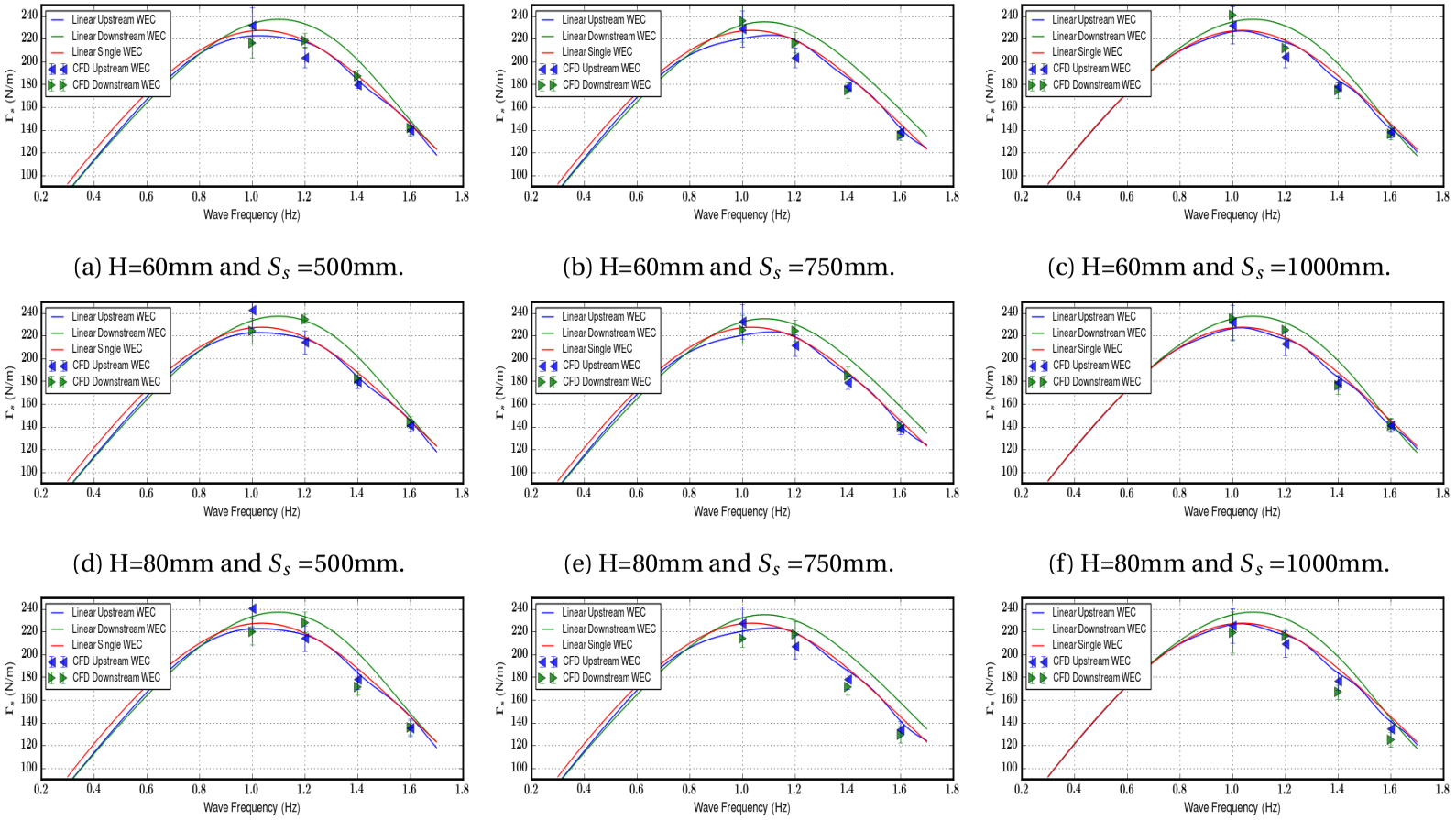

(a) H=60mm and S_s =500mm. (b) H=60mm and S_s =750mm. (c) H=60mm and S_s =1000mm.

(d) H=80mm and S_s =500mm. (e) H=80mm and S_s =750mm. (f) H=80mm and S_s =1000mm.

(g) H=100mm and S_s =500mm. (h) H=100mm and S_s =750mm. (i) H=100mm and S_s =1000mm.

Fig. 3.4 Comparisons of linear FEM and CFD surge forcing on two submerged spheres in a row with various incident wave heights and separations.

appreciable difference between Γ_s while they both follow the upstream and single WEC values from the linear model. Again we see a decrease in Γ_s values at higher frequencies with increasing wave height. The incident wave frequency of 1.2Hz shows larger Γ_s values on the downstream WEC, which is expected from on linear results but of note is that the magnitudes are lowest with a 60mm wave height. The CFD results for WEC separations of 500mm clearly shows wave height dependence on the heave excitation force which is expected considering the findings from 2, [10] on a single sphere. Γ_s however shows results which are in contrast to linear results which are amplitude independent. The unsteady behaviour of Γ_i captured through CFD produces an unexpected result where larger variability appears at lower, more linear wave heights. A deeper investigation into these results will follow in this work.

For a WEC separation of 750mm, the CFD forcing results are given against linear FEM model. For Γ_h (Figs. 3.3b, 3.3e and 3.3h), we see a similar trend in the results to the previous case with a small WEC separation. Larger Γ_h appears on the downstream WEC which reduce in magnitude with increasing wave height. Of note is the outlying results seen in Fig. 3.3h at f = 1.4Hz. In this case Γ_h appearing on the downstream sphere drops significantly below linear values and CFD upstream WEC results. This is a unique outcome which does not have a clear cause from just Γ_h results. For Γ_s (Fig. 3.4b,3.4e and 3.4h), we do not see the peak force reversal at 1.0Hz that was seen in the 500mm array at all wave heights but it is evident that this tend is amplitude dependent. The reversal happens at H =100mm and the transition is evident as the wave height increases. From this result it may be suggested that this effect is both WEC separation and amplitude dependent.

For a WEC separation of 1000mm, Figs. 3.3c,3.3f and 3.3i, Γ_h shows a large amount of variation on the downstream WEC for high incident wave frequency. The larger mean values of Γ_h on the downstream WEC in all cases for incident wave frequencies of 1.0Hz and 1.2Hz is expected from linear theory but this behaviour reverses for higher frequencies. For Γ_s, Figs. 3.4c,3.4f and 3.4i we see similar behaviour with increasing incident wave frequency. However we can see the steep drop in Γ_s on both upstream and downstream WECs with increasing wave frequency particularly for the downstream WEC. From all Γ_i results presented here it is clear that downstream WEC is adversely effected by the presence of the upstream WEC. The flow dynamics between the WECs creates a significant impact on the Γ_i results which cannot be resolved by linear modelling and are discussed in detail in the following section.

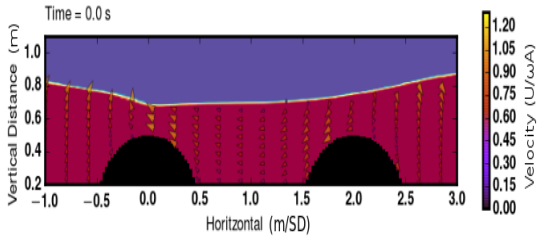

(a) H=60mm, f =1.0Hz and S_s =500mm.

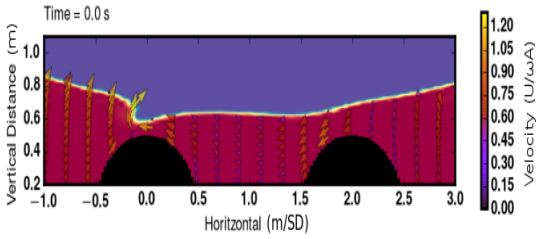

(b) H=100mm, f =1.0Hz and S_s =500mm.

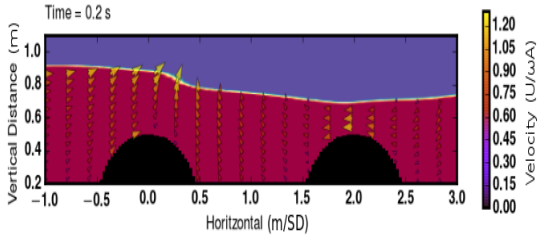

(c) H=60mm, f =1.0Hz and S_s =500mm.

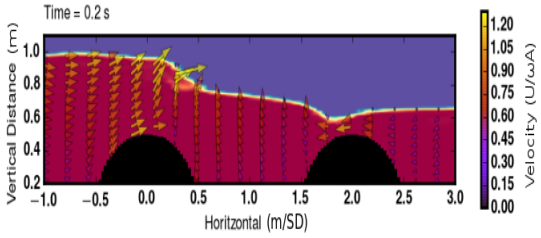

(d) H=100mm, f =1.0Hz and S_s =500mm.

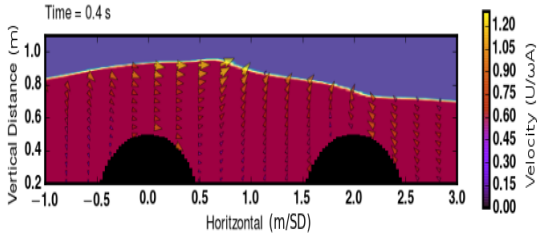

(e) H=60mm, f =1.0Hz and S_s =500mm.

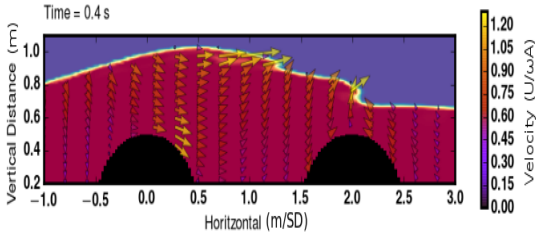

(f) H=100mm, f =1.0Hz and S_s =500mm.

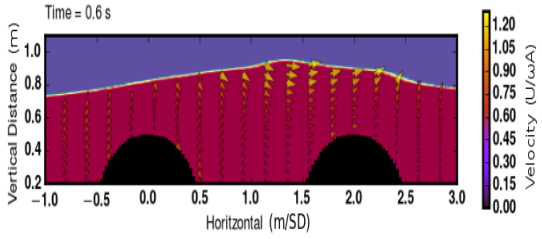

(g) H=60mm, f =1.0Hz and S_s =500mm.

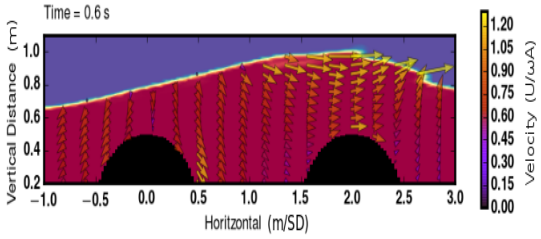

(h) H=100mm, f =1.0Hz and S_s =500mm.

Fig. 3.5 Comparisons of vertical free surface timeseries for 60mm and 100mm incident wave heights and frequency 1.0Hz

Free Surface Behaviour

The variations in Γ_i from CFD against linear FEM can be attributed to the nonlinear setup of the numerical domain. From previous work, [10], the free surface interaction with the

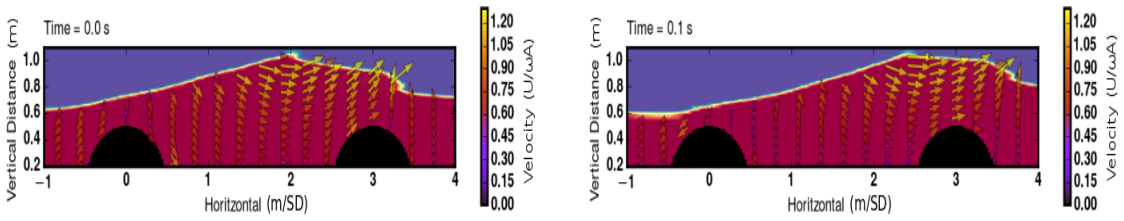

(a) H=100mm and S_s =750mm.

(b) H=100mm and S_s =750mm.

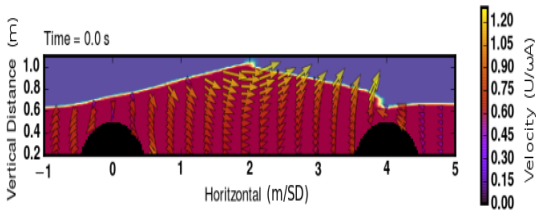

(c) H=100mm and S_s =1000mm.

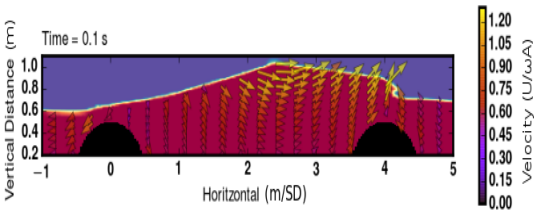

(d) H=100mm and S_s =1000mm.

Fig. 3.6 The 1.0Hz breaking wave form for S_s =750mm and 1000mm.

WECs was the largest contributor to Γ_i variations. With the introduction of a second WEC we compound the problem where free surface disturbances are produce by both WECs. Figure 3.7 shows a comparison between the wave interaction with the two, $S_s = 500$mm WEC array with 60 and 100mm incident waves. It can be immediately seen that the high amplitude waves break as they pass over both WECs. The form of the free surface in both the low and high wave height show very similar forms where the main difference is simply the breaking wave produced with a large incident wave height. The impact of the breaking wave generated by the upstream WEC, in Fig. 3.5f creates a steep front which is still evident as the wave peak passes over the downstream WEC.

In Fig. 3.6 we see a similar process with the upstream WEC breaking wave but note that the point where the wave is dissipating occurs before the downstream WEC. This makes the wave front incident on the downstream WEC less steep and less irregular which can contribute to the variations in Γ_i. Higher frequency incident waves see the breaking wave diffuse further ahead on the downstream WEC diminishing this effect.

Figure 3.7 shows the phase averaged [25], free surface amplitudes in the region surrounding the WECs in each configuration for an incident wave height of 60mm and frequency 1.0Hz. Large free surface amplitudes produced by the upstream WEC are seen to interact with the downstream WEC when they are closely spaced (Fig. 3.7a). The wave wake from the downstream WEC in Fig. 3.7a appear to have a different form compared

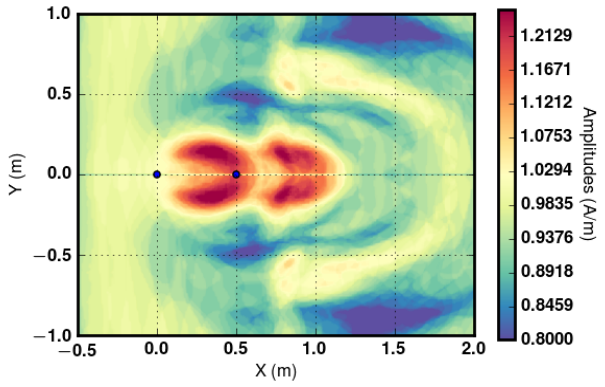

(a) H=100mm, f=1.0Hz, S_s =500mm.

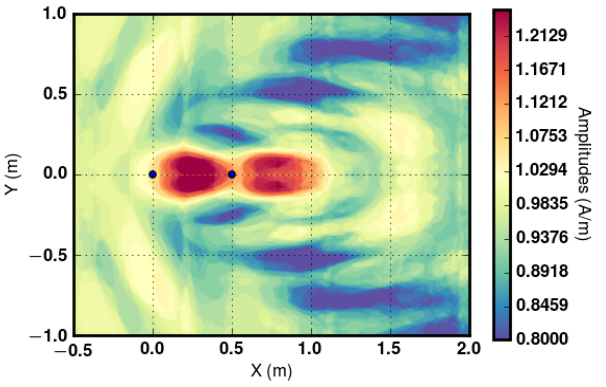

(b) H=100mm, f=1.4Hz, S_s =500mm.

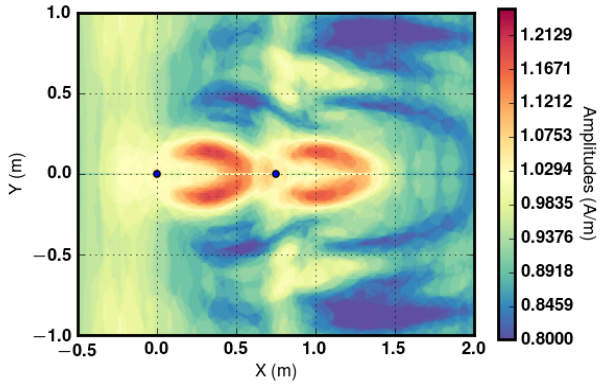

(c) H=100mm, f=1.0Hz, S_s =750mm.

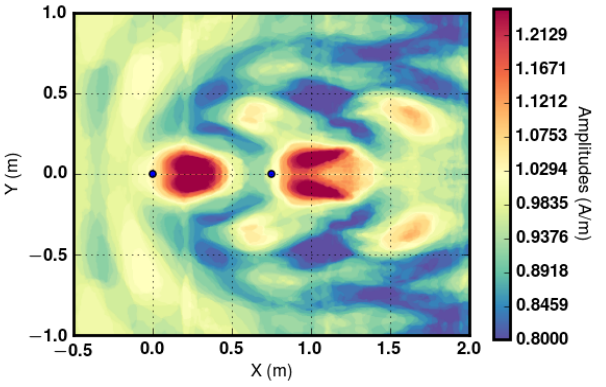

(d) H=100mm, f=1.4Hz, S_s =750mm.

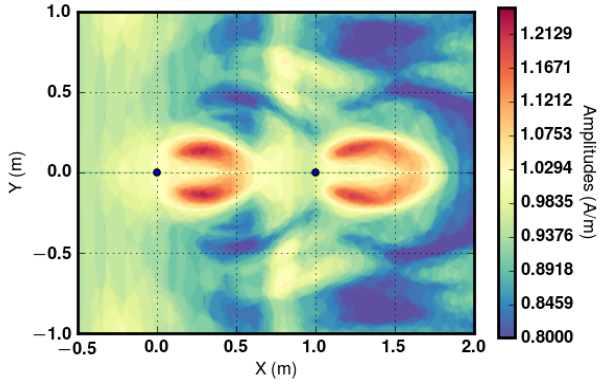

(e) H=100mm, f=1.0Hz, S_s =1000mm.

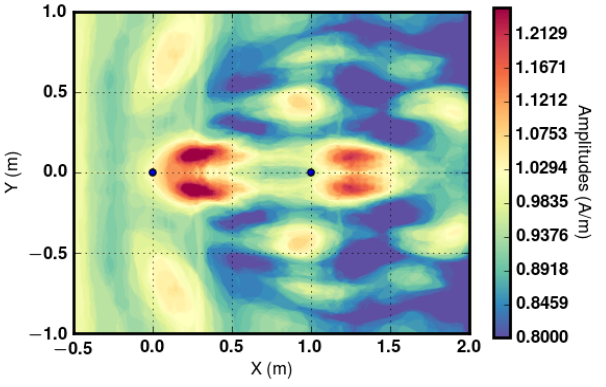

(f) H=100mm, f=1.4Hz, S_s =1000mm.

Fig. 3.7 Free surface phase averaged wave amplitudes for incident wave height of 100mm and frequencies of 1.0Hz and 1.4Hz.

to that seen in Figs. 3.7c, 3.7e which is evidence of the upstream WECs impact on the downstream WEC. The frequency of the incident wave determines the form of the shape

of the wave wakes. Figures. 3.7b, 3.7d and 3.7f show the diffraction field for an incident wave frequency of 1.4Hz. For a 1.4Hz incident wave frequency we can see that the large free surface amplitudes generated by the upstream WEC do not overlap the downstream WEC (Fig. 3.7b) which would imply that the wave at high amplitudes has broken before passing the downstream WEC. As the WECs are placed farther apart (Figs. 3.7d, 3.7f), the wave breaking would have diffused prior to the wave passing the downstream WEC but variations in the wave wakes from both WECs with separation suggest that the proximity impacts the form of the breaking wave.

Summary

This section has analyzed the nonlinear effects on the excitation force Γ_i appearing in the diffraction problem for two WECs in a row. Results for Γ_i from Section 3.4.1 shows good agreement against linear modelling on the upstream WEC for low incident wave heights while significant variation is seen on the downstream WEC. The deviations in Γ_i seen at low incident wave height is unexpected as this represents a more linear regime case. The stability of the wave interference between the two WECs could be brought into question as a cause for the large variability for low incident wave heights. Considering Fig. 3.3b, we see that the linear forcing results are within the CFD predicted variability. Assuming the wave interference is not stable however, it is plausible that a periodic increase and decrease in Γ_i from CFD would occur as there would be a periodic increase and decease in wave amplitudes. In general, CFD predicts a decrease in Γ_i and its associated variability with increased incident wave height in all cases. This is similar to the results found in [10]. The clear benefit of the array configuration toward improved WEC PTO predicted by linear modelling is not seen in CFD. The wave breaking would contribute to this result and time dependent wave interference stability may play an important role in the overall array performance characteristics.

3.4.2 Four Wave Energy Converters

In this section we investigate Γ_i and the wave interaction between four submerged spherical WECs in the square array shown in Fig. 3.1b. The WEC dimensions, depths and separations are identical to that in the previous case with the WEC center line distance from the symmetry plane being set as $(1/2)S_s$.

The amplitude independent FEM results for Γ_i on the upstream and downstream WECs are presented in Figs. 3.8, 3.9 and 3.10 along side results from a single WEC for comparison. Results are only given for one upstream and one downstream WEC owing to the

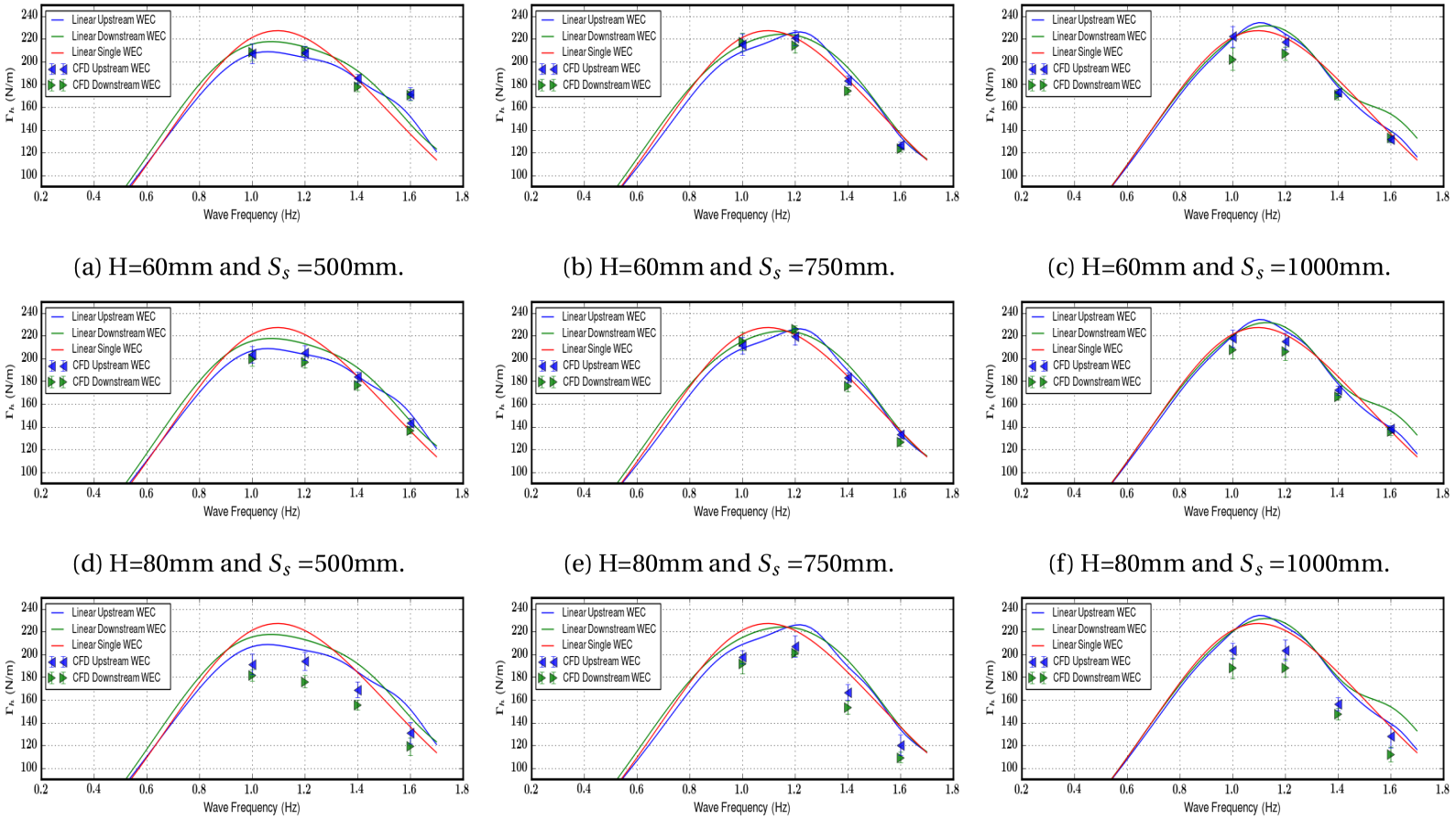

(a) H=60mm and S_s =500mm. (b) H=60mm and S_s =750mm. (c) H=60mm and S_s =1000mm.

(d) H=80mm and S_s =500mm. (e) H=80mm and S_s =750mm. (f) H=80mm and S_s =1000mm.

(g) H=100mm and S_s =500mm. (h) H=100mm and S_s =750mm. (i) H=100mm and S_s =1000mm.

Fig. 3.8 Comparisons of linear FEM and CFD heave forcing on four submerged WECs in a square with various incident wave heights and separations.

problem symmetry. Linear results show a noticeable change in Γ_i on the upstream WEC particularly for S_s = 750mm, 3.8b, 3.8e and 3.8h. In this configuration Γ_h on the upstream WEC becomes greater than that on the downstream WEC which was not observed in the previous case. Figure 3.10 shows the linear forcing results for sway which is generated via waves radiating perpendicular to the direction of propagation. The resulting Γ_w is linearly predicted to be an order of magnitude lower than that seen in heave and surge and constitutes a small component of the total Γ_i experienced by the WEC. What follows is a detail description of the CFD results for the four WECs in a square with S_s =500mm, 750mm and 1000mm.

Nonlinear Excitation Forces

The values for Γ_h, Γ_s and Γ_w predicted by CFD are given in Figs. 3.8, 3.9 and 3.10 with the associated RMSE values against linear given in Appendix Tables B.3, B.4 and B.5. Γ_h for the S_s =500mm array (Figs. 3.8a, 3.8d, 3.8g) shows a decreasing trend with increasing wave height. For a low wave height, results for frequencies of 1.0Hz and 1.2Hz are in good agreement with linear predictions with notable increased variability on the downstream WEC, while higher frequencies show unexpected behaviour where CFD Γ_h exceeds linear values. The impact of wave height is strongly felt by the downstream WEC where Γ_h drops significantly below that appearing on the upstream WEC in direct contrast to linear results. For an array with S_s =750mm there is excellent agreement between linear and CFD results for the upstream WEC for wave heights of 60mm and 80mm while the mean values on the downstream WEC tend to fall below linear values with large variability. One overall CFD outcome is that the downstream WEC is consistently below the upstream WEC in contrast to the relatively equal forcing values predicted from FEM. For a separation of S_s =1000mm, the decrease in Γ_h on the downstream WEC is even more apparent. Even for low incident wave heights the Γ_h on the downstream WEC is consistently below linear model predictions while the upstream WEC continues to show good agreement. In particular, the shift in Γ_h trends on the downstream WEC from linear models at high wave frequencies is not captured in CFD. Of note as well, for all wave heights this increase sits outside of the variations of Γ_h captured by CFD.

Γ_s shown in Fig. 3.9, has significant differences compared to linear FEM results. The main observation is that Γ_s on the downstream WEC is consistently below that seen on the upstream WEC with a large amount of variability. This would suggest that there is significant nonlinear interaction between the WECs effecting the flow on and or below the free surface. Apart from low Γ_s on the downstream WEC, the upstream WEC is also consistently below linear results with high variability for all incident wave heights. From

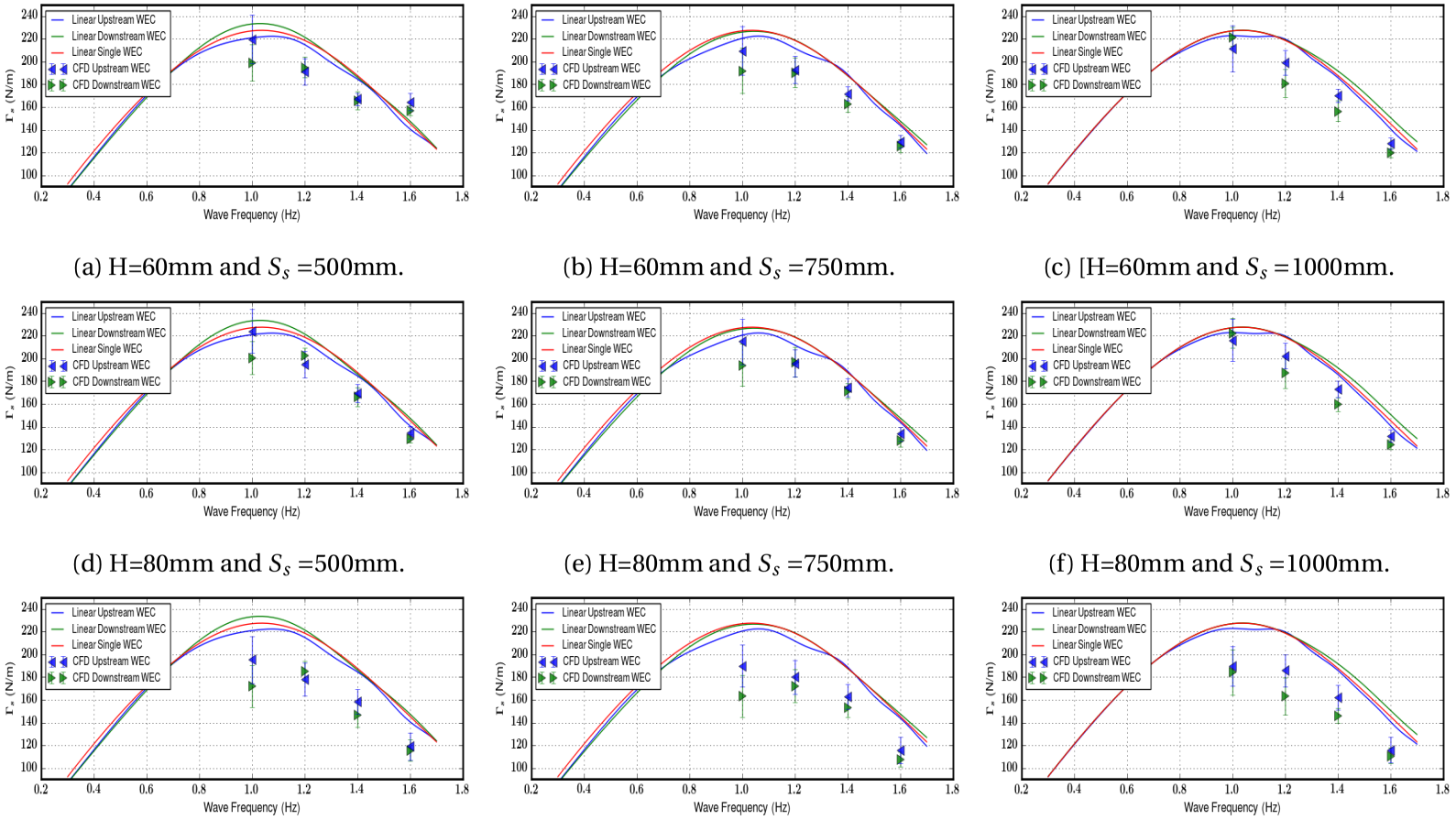

(a) H=60mm and S_s =500mm. (b) H=60mm and S_s =750mm. (c) [H=60mm and S_s =1000mm.

(d) H=80mm and S_s =500mm. (e) H=80mm and S_s =750mm. (f) H=80mm and S_s =1000mm.

(g) H=100mm and S_s =500mm. (h) H=100mm and S_s =750mm. (i) H=100mm and S_s =1000mm.

Fig. 3.9 Comparisons of linear FEM and CFD surge forcing on four submerged WECs in a square with various incident wave heights and separations.

previous results it is expected that there is a forcing decrease with increasing wave height, however the decreases seen here for Γ_s are more substantial that previously seen in heave and the two in a row array case. Of note are the mean Γ_i values between linear model and CFD results. Through linear modelling in general there are larger forces appearing on the downstream WEC while from CFD this is rarely the case, only occurring with S_s =1000mm and low incident wave heights. The apparent cause of these losses is not easily quantified but the free surface and flow fields may provide clues and are discussed in the following section.

The Γ_w on the upstream and downstream WECs are shown in Fig. 3.10. As Γ_w is produced purely by the diffracted wave from the WEC values for Γ_w are an order of magnitude lower than Γ_h or Γ_s. In the tight array, S_s =500mm, Figs. 3.10a, 3.10d and 3.10g, we can see that we have excellent agreement between CFD and linear model results particularly for low incident wave amplitudes. This result shows the capability of the CFD model in capturing the propagating diffracted wave and the interaction between the WECs. Increasing the wave height, we see a drop in the Γ_w for a 1.0Hz and 1.6Hz incident wave. For a separation S_s =750mm we see that the trends for Γ_w with incident wave frequency captured in the linear results is reproduced in CFD. Between the frequencies of 1.0Hz and 1.2Hz we see a peak force amplitude shift from the downstream to the upstream WEC, however the magnitudes predicted by CFD are consistently lower than that expected from linear results. Of note are the CFD Γ_w results for an incident wave of 1.4Hz. Here for all wave heights CFD shows approximately equal force on the up and downstream WECs while FEM predicts this to occur closer to 1.5Hz. For an array with S_s =1000mm the Γ_w trends are again consistent between linear and CFD modelling. These results provide strong validation for the CFD model as it is correctly capturing the small Γ_w amplitudes. Of note here is that there appears to me minimal impact on Γ_w with increasing incident wave height. This would suggest that the wave diffracted perpendicular to the propagating wave would tend to remain linear regardless of wave breaking or strong free surface effects.

Free Surface Behaviour

The propagating wave inline with the WECs for incident wave frequencies of 1.0Hz and 1.6Hz are shown in Fig. 3.11. For the 1.0Hz incident wave we can compare the form of the propagating wave with that for the two in a row WEC case shown in Fig. 3.5. We can see a similar breaking wave form in the two cases, however some differences are clear. Interaction between the WECs and free surface appear to be reduced when compared to the two WEC array in that the breaking wave is not as pronounced and the wave peak passing over the downstream WEC is relatively flat. This is a recurring result over multiple

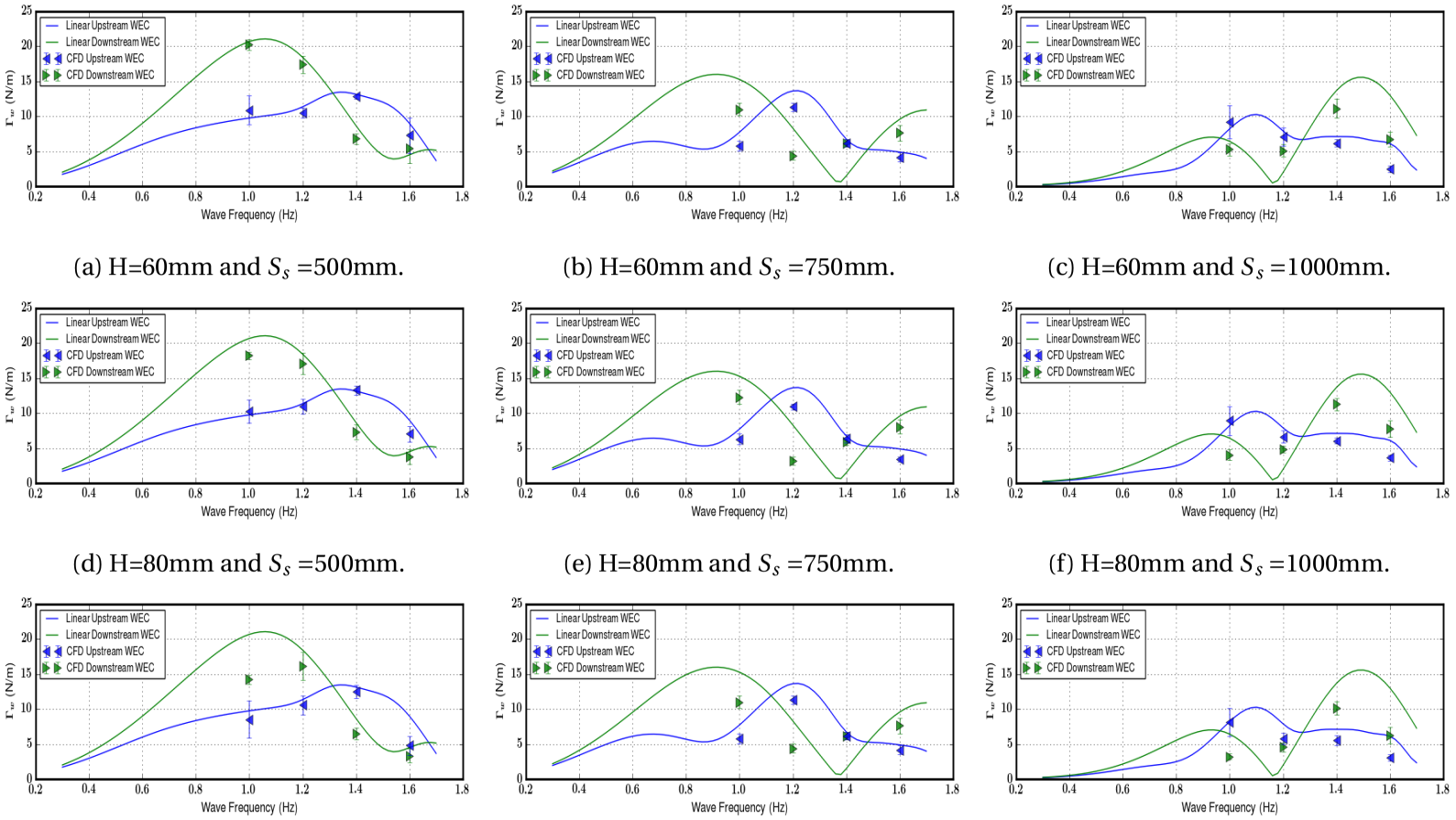

(a) H=60mm and S_s =500mm. (b) H=60mm and S_s =750mm. (c) H=60mm and S_s =1000mm.

(d) H=80mm and S_s =500mm. (e) H=80mm and S_s =750mm. (f) H=80mm and S_s =1000mm.

(g) H=100mm and S_s =500mm. (h) H=100mm and S_s =750mm. (i) H=100mm and S_s =1000mm.

Fig. 3.10 Comparisons of linear FEM and CFD sway forcing on four submerged WECs in a square with various incident wave heights and separations.

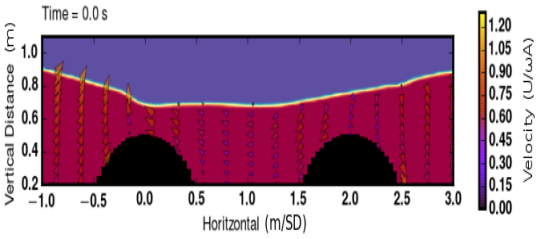

(a) H=100mm, f =1.0Hz and S_s =500mm.

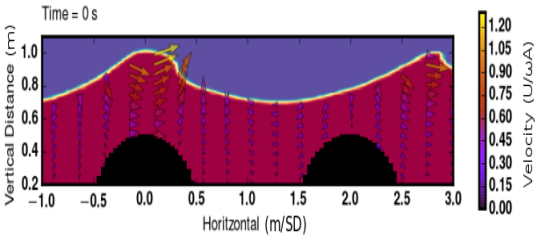

(b) H=100mm, f =1.6Hz and S_s =500mm.

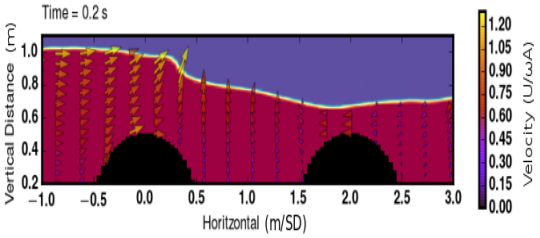

(c) H=100mm, f =1.0Hz and S_s =500mm.

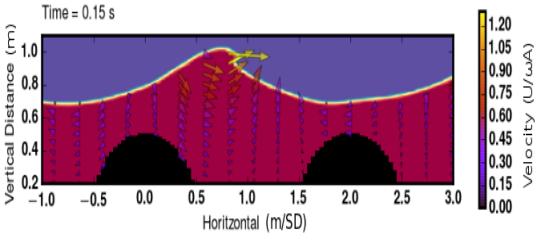

(d) H=100mm, f =1.6Hz and S_s =500mm.

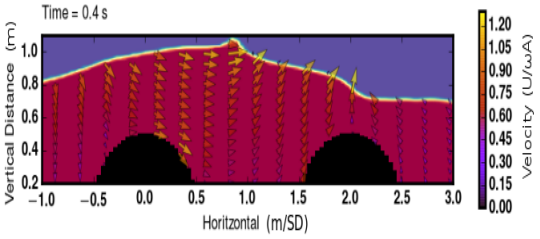

(e) H=100mm, f =1.0Hz and S_s =500mm.

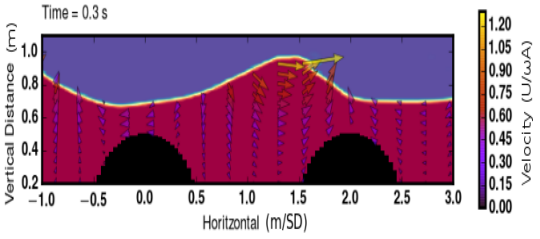

(f) H=100mm, f =1.6Hz and S_s =500mm.

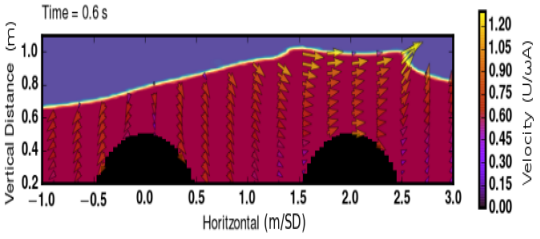

(g) H=100mm, f =1.0Hz and S_s =500mm.

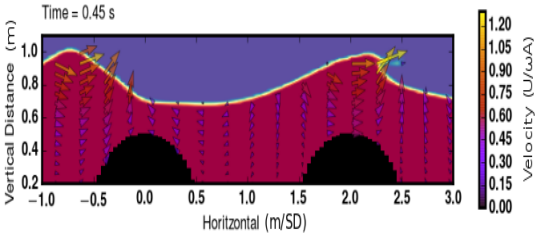

(h) H=100mm, f =1.6Hz and S_s =500mm.

Fig. 3.11 Examples of free surface timeseries for incident wave heights of 100mm and frequency 1.6Hz.

periods in the simulations. Reducing the onset of the breaking wave would suggest more linear results but from the previous section, we know the downstream WEC continues to experience substantial losses in Γ_i. This flattening however indicates that energy and

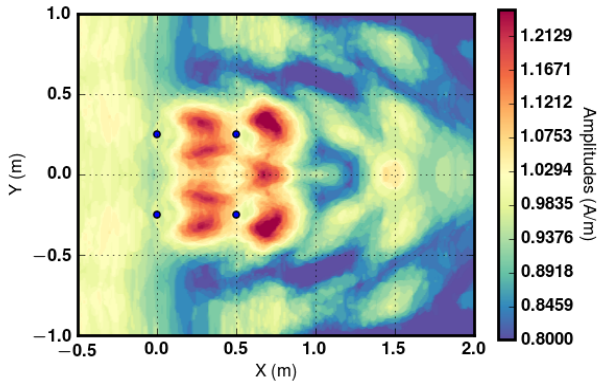

(a) H=100mm f =1.0Hz, S_s =500mm.

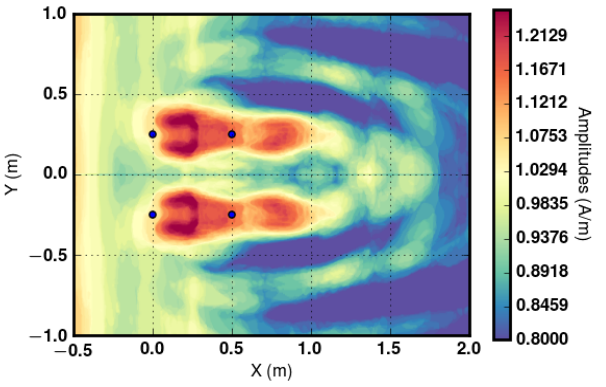

(b) H=100mm f =1.2Hz, S_s =500mm.

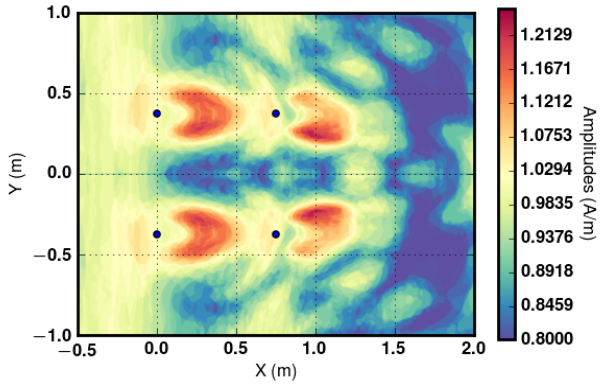

(c) H=100mm f =1.0Hz, S_s =750mm.

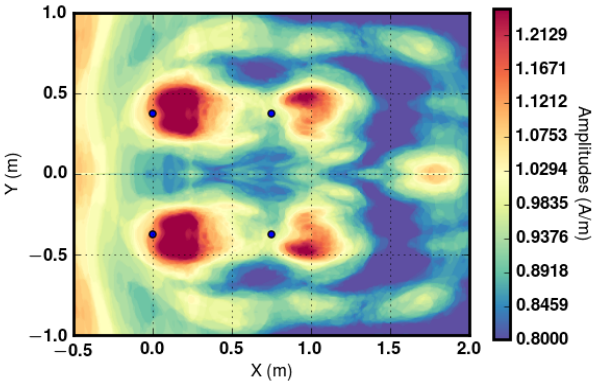

(d) H=100mm f =1.2Hz, S_s =750mm.

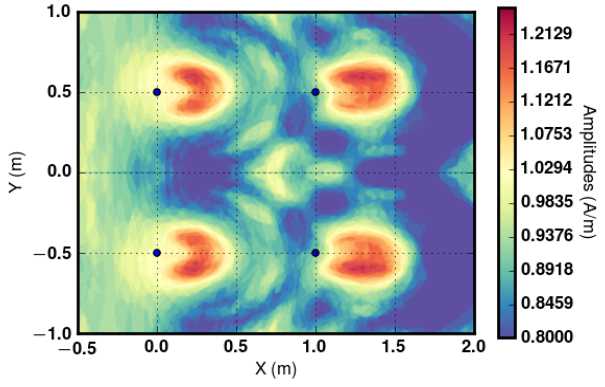

(e) H=100mm f =1.0Hz, S_s =1000mm.

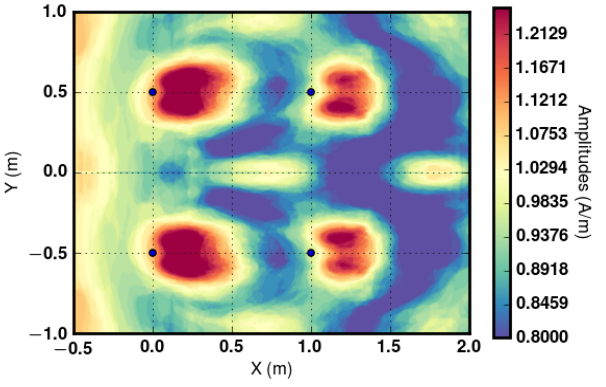

(f) H=100mm f =1.2Hz, S_s =1000mm.

Fig. 3.12 Free surface phase averaged wave amplitudes for incident wave height of 100mm and frequencies of 1.0Hz and 1.2Hz.

subsequently wave height is lost in the propagating wave. Through the calculation of Γ_i, if this is the case, we would expect such low values for Γ_i as the excitation force experienced

by the downstream WEC is due to a wave of a smaller wave height. For the 1.6Hz incident wave (Figs. 3.11b,3.11d,3.11f and 3.11h), The nonlinear form of the wave causes less free surface interaction with the WEC due to shallower wave troughs, however it is clear that the upstream WEC forces the wave to break regardless, altering the wave passing over the downstream WEC. The free surface interaction is shown to be reduced compared to the two WEC case while the effect on the hydrodynamic forcing is larger.

The free surface variations for 100mm wave height incident wave with frequencies of 1.0Hz and 1.2Hz are shown in Fig. 3.12. For the 1.0Hz incident wave (Figs. 3.12a,3.12c and 3.12e) we can immediately see a difference in the wave wakes compared to the two WEC array. For all WEC separations the wave wakes are no longer symmetric about the center line of each row and, particularly on the downstream WECs the point of peak wave amplitude is shifted either inword or outward of the array. This would only be caused by the diffracted waves propagating through the array. The downstream WECs see the largest impact from this diffraction as with large separations the upstream WEC wave wakes begin to appear symmetric. The close separation S_s =500mm also appears to show a peak wave height reduction over the downstream WECs compared to two WEC array which would explain the losses in the hydrodynamic forcing. For the 1.2Hz incident wave we again see the increased wave heights appearing over top of the downstream WECs indicating force gains, however the results from the previous section show this to be a highly variable particularly for large incident wave amplitudes. The asymmetry in the peak wave heights is again dependent on the separation.

Summary

This section has analyzed the nonlinear effects appearing in the diffraction problem for four WECs in a square configuration. Γ_i shown in Section 3.4.2 are substantially different to those predicted through linear theory. Γ_w in particular is far below linear values and the expected increases on the downstream WEC are rarely seen, only occurring with low incident wave amplitudes and large WEC separations. As in the two in a row case, large variability in Γ_h and Γ_s appear on the downstream WEC. The stability of the interference wave field with nonlinear interactions may contribute to this behaviour. In general Γ_h and Γ_s well below that predicted in linear theory, however in Γ_w there is excellent correlation with minimal variation brought about by an increasing incident wave height. As in the two in a row WEC array case the benefit of the array configuration predicted through linear models does not appear in CFD. Free surface interaction would be a strong contributor, effecting interaction stability and reducing the overall energy available for capture by the downstream WEC devices.

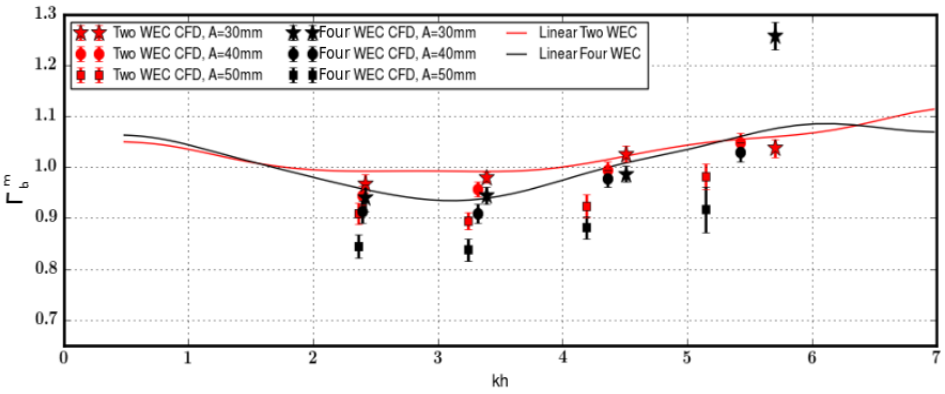

(a) Normalised heave excitation force for S_s =500mm.

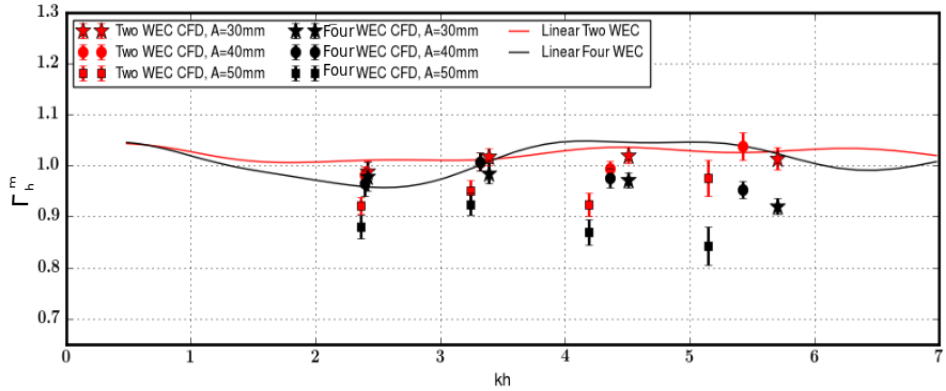

(b) Normalised heave excitation force for S_s =750mm.

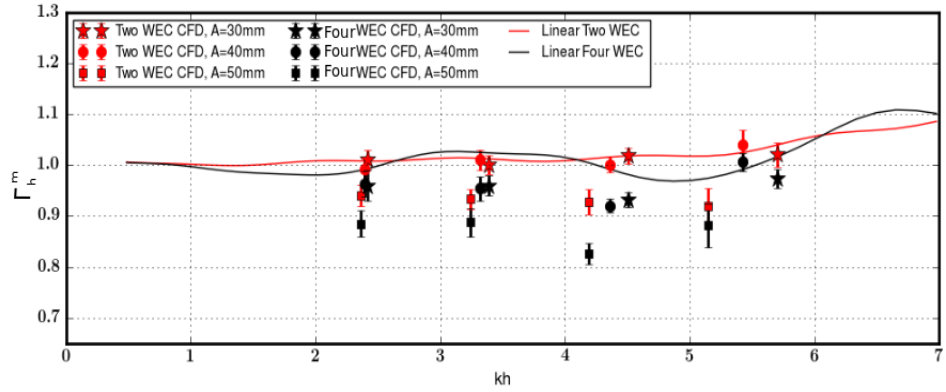

(c) Normalised heave excitation force for S_s =1000mm.

Fig. 3.13 Comparisons of the average WEC excitation forces for heave and surge from linear FEM and CFD models.

3.5 Array Excitation Force

The main goal of this work is to understand the total PTO performance of the WEC arrays. Normalising the mean Γ_i of the two in a row and four in a square arrays by the Γ_i of a single WEC we can clearly see if the array benefits appear with the introduction of nonlinear effects. Figure 3.13 shows the normalised mean heave excitation forces for each array configuration and WEC separation where k is the wavenumber and h is the water depth. In Fig. 3.13a we can see the comparisons for a WEC separation of S_s =500mm. Lower incident wave heights show excellent agreement with linear predictions showing the same excitation force benefits for large kh values. The outlier for the square array case from CFD corresponds the over-predicted heave excitation force values shown in Fig. 3.8a. Interestingly this dramatic increase occurs near the excitation force peak predicted in the linear model. For increasing wave heights which has the effect of diminishing kh values through intermediate depth wave speed variations, we see the expected drop in array efficiency but is limited to $\approx$ 10% for each frequency. In Fig. 3.13b we have good agreement between low wave height CFD and linear models for the two in a row array. The square array however does not exhibit the behaviour expected from linear predictions. The excitation force increase between kh =3.5 and 5.5 does not occur in CFD results. This may be due to the nonlinear effects shown in the previous section and is expected considering the excitation force results shown in Figs. 3.8 and 3.9. This is again the case for WEC separations S_s =1000mm, however the array benefit with array excitation forces ≥ 1 appear in the two WEC array.

The array surge excitation forces for each array separation are shown in Fig. 3.14. In general the CFD excitation forces particularly at high kh are distinctly below that predicted from linear models. The two WEC array at low kh however shows an array excitation for ≥ 1 for each WEC separation which is expected from linear theory. The square array however does not show any array benefit apart from the outlining case in the S_s =500mm array. This result combine with the trends in the heave case, would suggest that increasing the number of WECs in an array has the negative effect of reducing overall PTO potential through the increase of nonlinear interactions within the array. This is of great importance for the continuing development of WEC technology. The generation of nonlinear effects which diminishes the performance of WEC arrays would be largely device dependent and so further work is required to understand the generation and effect of nonlinear interaction within WEC arrays.

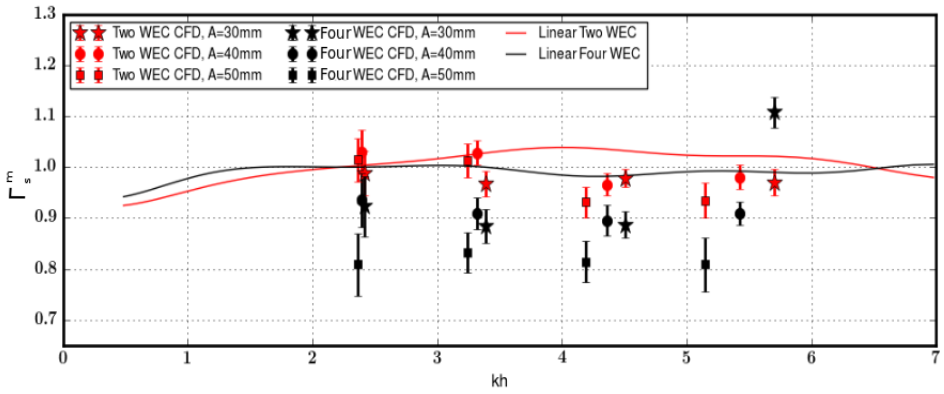

(a) Normalised surge excitation force for S_s =500mm.

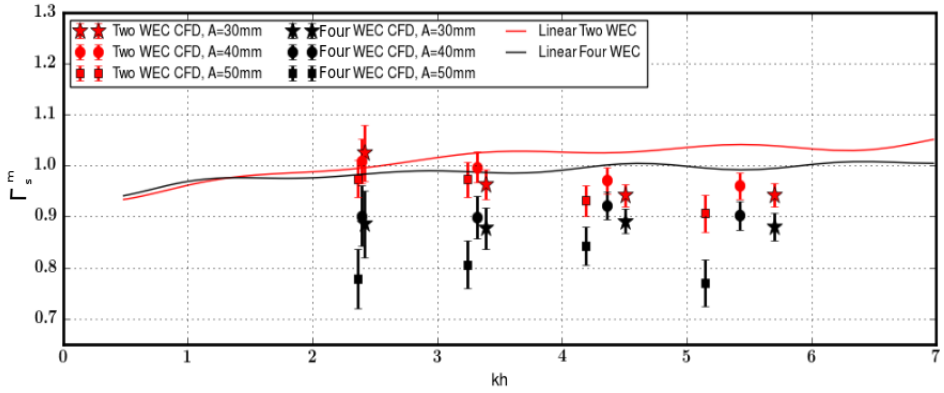

(b) Normalised surge excitation force for S_s =750mm.

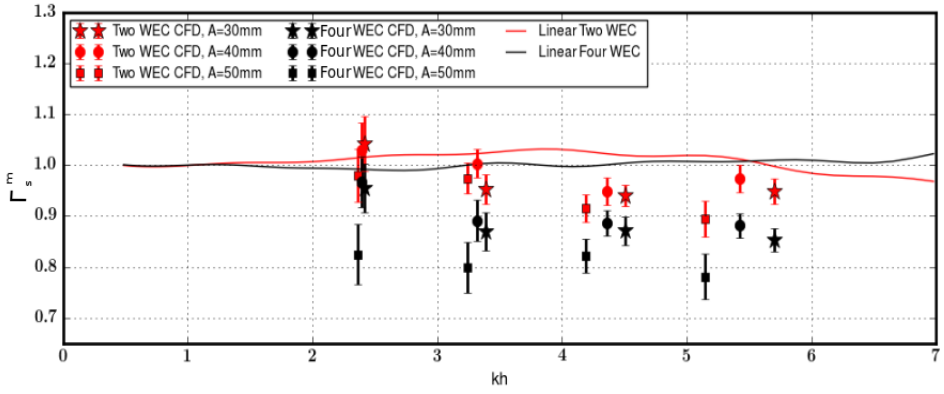

(c) Normalised surge excitation force for S_s =1000mm.

Fig. 3.14 Comparisons of the average WEC excitation forces for heave and surge from linear FEM and CFD models.

3.6 Conclusions

This work applies a 3D nonlinear, SST URANS VOF CFD model to simulate the diffraction problem for arrays of generic submerged spherical WECs. Arrays of two WECs in a row and four WECs in a square were used with three WEC separations of 500mm, 750mm and 1000mm with incident wave heights of 60mm, 80mm and 100mm and wave frequencies of 1.0Hz, 1.2Hz, 1.4Hz and 1.6Hz. A linear FEM model was adapted and used to validate CFD results. Applying a fully nonlinear modelling technique to study the diffraction problem for a WEC here gives valuable insight into the PTO potential of WECs operating in close proximity. Significant differences between linear model predictions and subsequent CFD results shown here suggest that nonlinear effects will greatly impact a WEC array.

Chapter 4

Nonlinear Modelling of the Radiation within Arrays of Generic Wave Energy Converters

This chapter is under review for publication and is in press for the Journal of Renewable Energy at the time of writing. The journal publication here has been edited, altering the introduction, theory and conclusion sections but is otherwise unchanged from the original article.

4.1 Abstract

The nonlinear interaction between a single WEC and the environment can have a detrimental effect on it's overall performance. These effects from a single device propagating further into an array of WECs is a question that is as yet not well understood. Linear modelling has been used successfully to demonstrate the benefits of WECs operating in array configurations showing significant increases in power capture versus that from isolated devices however, these models neglect or simply linearise nonlinear processes which are prominent in real ocean environments. The present study aims to address this issue by implementing a fully nonlinear turbulent CFD model to study the WEC array problem. In combination with previous work focussing on the diffraction problem, the present study investigates the heave and surge radiation forces for WEC arrays of two and 4 generic spherical devices. This work demonstrates the q-factors from CFD results against established linear results and highlight the variations causing the major discrepancies between the two approaches.

4.2 Introduction

This chapter investigates the radiation problem for arrays of generic WECs and represents the completion of the work in Chapter 3 which investigated the diffraction problem on arrays of two and four generic spherical WECs. Here the radiation problem is solved using a fully nonlinear computational fluid dynamics (CFD) shear stress transport (SST) unsteady Reynolds averaged Navier-Stokes (URANS) model to determine the hydrodynamic coefficients which are important to the characterisation of a WEC array in the linear regime. The radiation impedance coefficients described in Section 1.2.2 for a heaving and surging active WEC are modeled in CFD and verified against the established linear model given by Nader *et al.* [50, 47, 45] which has been adapted to the diffraction and radiation problems for a heaving and surging generic submerged spherical WEC. The implementation of the linear model is discussed in detail in [9, 10].

The work that follows here discusses the hydrodynamic forcing on an array of devices occurring from the radiation motions in both heave and surge from an active model. Results shows the comparisons of the findings from both linear and nonlinear approaches to the problem. The free surface behaviour due to the radiating sphere is presented and discussed prior to a comparison of the q-factor values for each configurations. The outcomes of this work will show the variation of the array performance of WECs when incorporating nonlinear effects.

4.2.1 The CFD Numerical Wave Tank

For the nonlinear component of this study, an incompressible SST RANS VOF CFD model was used. The commercial code CD-Adapco Star-CCM+ version 10.02.012 was used for all CFD simulations, built as an extension of the model described in [9, 10]. The VOF method allows this model to resolve the nonlinear effects occuring between the free surface and WECs shown in [9, 10] and the present study investigates these effects on surround WECs.

The numerical wave tanks (NWT)s used in this study investigate two WEC array configurations of two in a row and four in a square with WEC separations (S_s) of 500, 750 and 1000mm with the minimum distance between each WEC to the closest wall being 16 sphere diameters (SD). Examples of these two configurations are given in Fig. 4.1. Unlike the study of the diffraction problem in previous work [8] a symmetry plane is not included to reduce the size of the computational domain. Thus the tank bottom and all four walls are no-slip wall boundaries with top boundary set as a pressure outlet. To simulate a radiating sphere, the overset meshing capabilities of Star-CCM+ were used in order to prescribe the necessary WEC motions required. Simulation times were then set

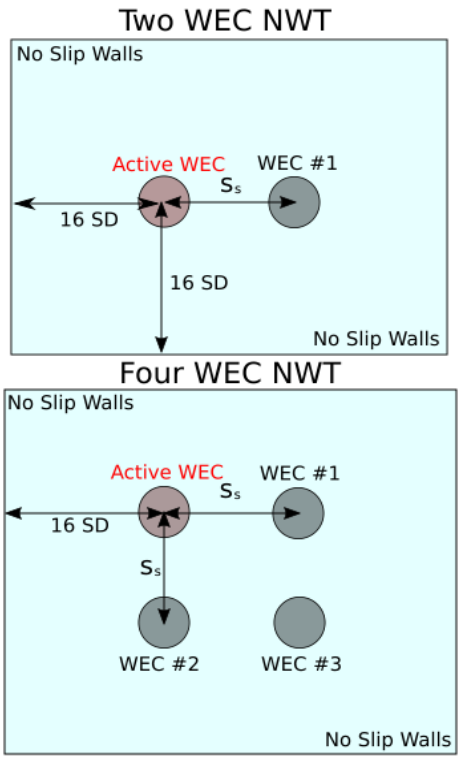

Fig. 4.1 Examples of the NWT setups used in this study.

to ensure a minimum of three radiated wave reflections between each WEC before forcing data was considered usable for calculations. This was done in order to ensure a stable order of interaction between each device and wave damping was applied on each sidewall boundary to ensure no wave reflections interfere with the arrays.

4.2.2 The Computational Meshes

The computational meshes used in this study are an extension of the radiation NWTs developed in [9, 10]. The mesh characteristic $M_c \leq 2.5$ for each condition is used to ensure accurate wave propagation. Here however the oscillation amplitude of the WEC does not translate to the radiating wave amplitude and so a maximum amplitude of 50mm is used to apply M_c chosen based on previous results. As mentioned previously the overset meshing technique is used to allow for the radiating WEC motion. Following previous work the background mesh and overset mesh resolution are kept consistent allowing for accurate interpolation across the overset boundary. In Bharath *et al.* [10] applying these meshing constraints RMSE values between CFD and experimentally measured results were calculated to be $\leq 10\%$ and $\leq 5\%$ for heave and surge oscillations respectively. At a

maximum, radiation computational meshes contained ≈4 million cells in the four WEC array.

4.3 Results and Discussion

4.3.1 Radiation Impedance Coefficients for the Oscillating WEC

In this section we investigate the radiation impedance Z^k_{mAnA} on the active WEC in both the two and four WEC arrays. The spherical WECs all have a diameter of d = 250mm with separations of S_s =1000mm, 750mm and 500mm. The water depth in each tank is 600mm and the mean WEC depth is 205mm for each. The oscillating frequencies for both heave and surge conditions are 1.0Hz, 1.2Hz, 1.4Hz and 1.6Hz. CFD oscillation amplitudes are 30mm, 40mm and 50mm. In each figure, the CFD results of the respective forcing are compared against those calculated through the linear FEM model [8, 10]. Z^k_{mAnA} results from CFD are calculated via the phase averaging method [25], applied after a minimum of two wave periods have been allowed to propagate through the arrays.

Two WEC Array

Here the array configuration of two WECs in a row is considered. In Fig. 4.2 we can see the results for both the Z^2_{xAzA} and Z^2_{zAzA} forcing experience by the active heaving WEC. Z^2_{zAzA} shows excellent agreement to the linear model while at high oscillation frequencies we begin to see a drop with increased amplitude. This is expected and agrees with finding found previously in [10] and can be attributed to interactions between the WECs and the free surface. Z^2_{xAzA} calculated in both CFD and linear modelling constitute ≈ 1% that Z^z_{zAzA} and can therefore be neglected. The large variability in Z^z_{xAzA} results from CFD would indicate that much of this force can be attributed to periodic shear force imbalances which would be largely dependent on the WEC design and the complex flows generated between the WEC and free surface. Mean RMSE values over each WEC separation are given in Appendix B.2.

In Fig. 4.3, we have Z^2_{xAxA} and Z^2_{xAzA} experienced by the active surging WEC. Z^2_{xAxA} follows the linear model again very well and shows little deviation with oscillation amplitude. This is again expected as previous results show that the Z^1_{xAxA} tends to remain linear as the WEC does not come into close proximity with the free surface. Of interest in the surging active WEC results are Z^2_{zAxA} values. It can be seen in Fig. 4.3a, 4.3b and 4.3c, that the surging motion is generating significant Z^2_{zAxA} values on the WEC. For an oscillating frequency of 1.0Hz, Z^2_{zAxA} is ≈ 10% of Z^2_{xAzx} and in all cases has a distinctive

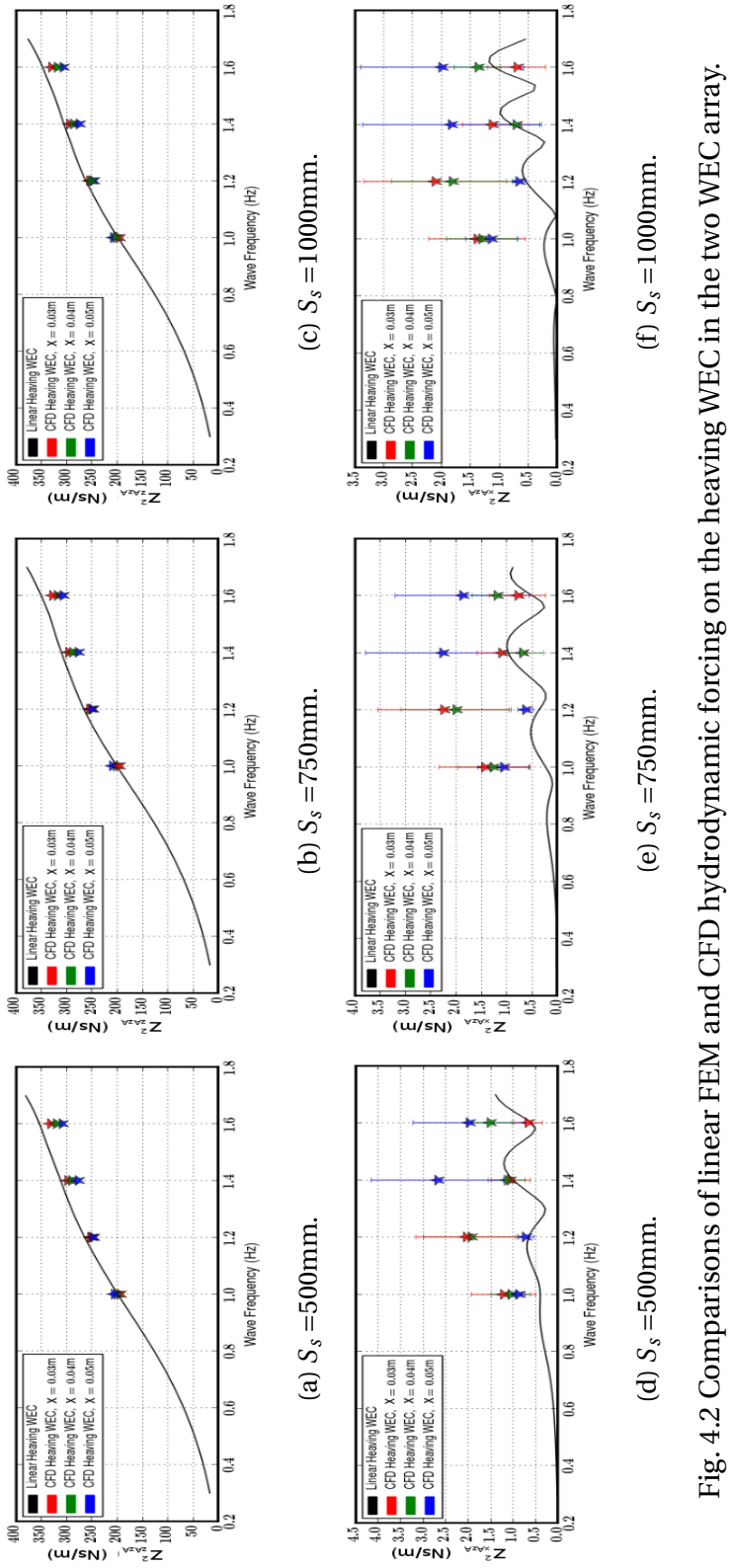

(a) S_s =500mm. (b) S_s =750mm. (c) S_s =1000mm.

(d) S_s =500mm. (e) S_s =750mm. (f) S_s =1000mm.

Fig. 4.2 Comparisons of linear FEM and CFD hydrodynamic forcing on the heaving WEC in the two WEC array.

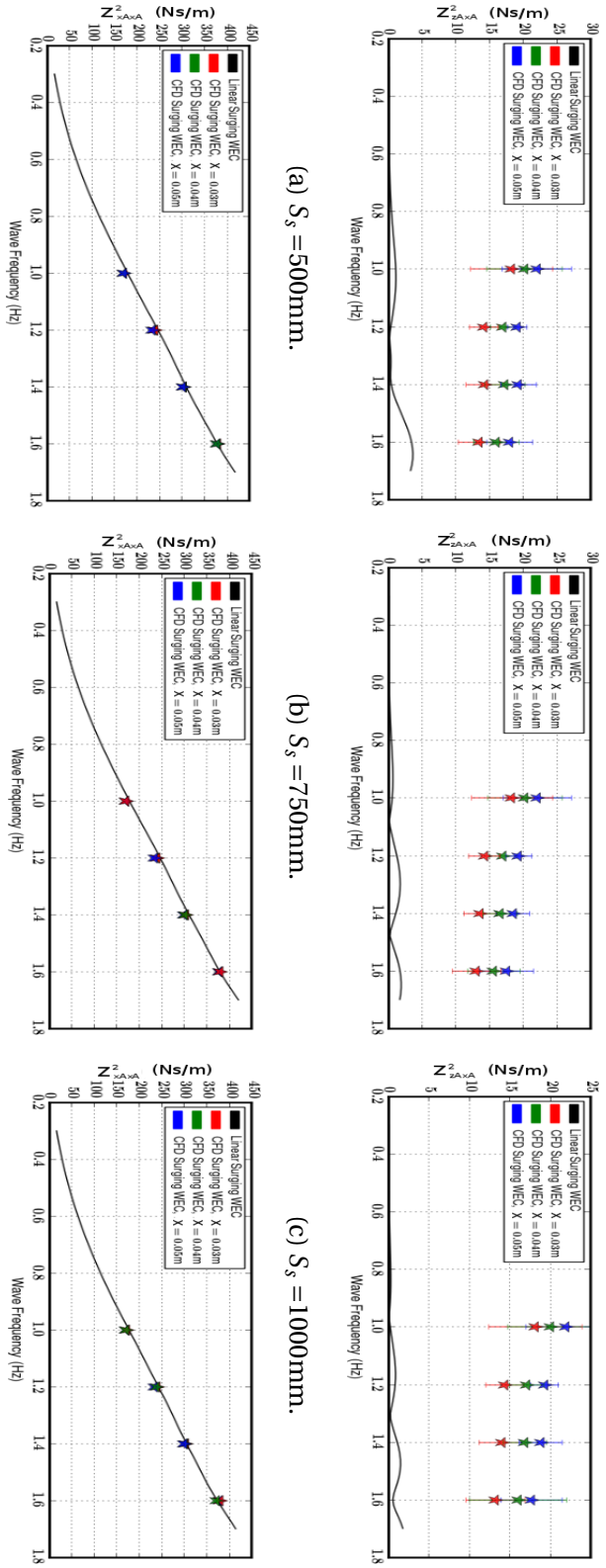

(a) $S_s = 500$mm. (b) $S_s = 750$mm. (c) $S_s = 1000$mm.

(d) $S_s = 500$mm. (e) $S_s = 750$mm. (f) $S_s = 1000$mm.

Fig. 4.3 Comparisons of linear FEM and CFD hydrodynamic forcing on the surging WEC in the two WEC array.

relationship to oscillation amplitude. This can be attributed to the subtle difference in modelling techniques. In the linear FEM case, velocity boundary conditions are placed on the WEC surface which represent the fluid motions that would occur if the body was indeed in motion. For infinitesimal motions, which is a basis of potential flow modelling this is acceptable. In the CFD approach however, the WEC itself is physically moving a finite amount creating the fluid velocities and therefore moves away from the centre of the dipole radiation field which would maintain relatively neutral values of Z^2_{zAxA} across the surface of the WEC. This result indicates that a surging device would induce significant values of Z^2_{zAxA} on itself which are not represented in linear models. Since the magnitude of Z^2_{zAxA} is a significant fraction of Z^2_{xAxA} it would be expected that this would effect the motions of an operating WEC.

Four WEC Array

The results for heaving (Z^4_{xAzA}, Z^4_{yAzA} and Z^4_{zAzA}) and surging (Z^4_{xAxA}, Z^4_{yAxA} and Z^4_{zAxA}) active WECs are shown in Figs. 4.4 and 4.5 respectively. The results Z^4_{izA} are similar to Z^2_{izA}. Z^4_{zAzA} diminishes with amplitude at high frequencies and Z^4_{xAzA} is again negligible. In the square array however it would be expected that WECs along the y-axis have the potential to generate sway forces, Z^4_{yAzA}. These however are again negligible for precisely the same reason as the surge forces. This would be expected due to the monopolar radiation field produced in this case, making Z^4_{xAzA} and Z^4_{yAzA} equivalent.

The results for Z^4_{ixA} are again comparable to Z^2_{ixA} values. Z^4_{xAxA} results again compare very well to the linear model and we again see that there is significant values for Z^4_{zAxA}. Here however we see that there appears to be a peak in Z^4_{zAxA} for an oscillation frequency of 1.4Hz for all amplitudes and WEC separations. The increased values for Z^2_{zAxA} for 1.0Hz oscillation appear to diminish for Z^4_{zAxA}. Values for Z^4_{yAxA} are also quite low as very little energy is radiated along direction perpendicular to the WEC motion.

Summary

Summarising Z^k_{iAjA} on the active WEC for $k = 2,4$, we can conclude that the values are in accordance with expectations from the results in [10] and in good agreement with linear models in the direction of oscillation. Deviations, particularly for Z^k_{zAzA} at high oscillation frequencies can be attributed to the interaction between the WEC and the free surface and are discussed further in later sections. The major discrepancy found through CFD modelling appear in Z^k_{zAxA}. These results may stem from the subtle differences in the modelling techniques however CFD does represent the more realistic results as it models

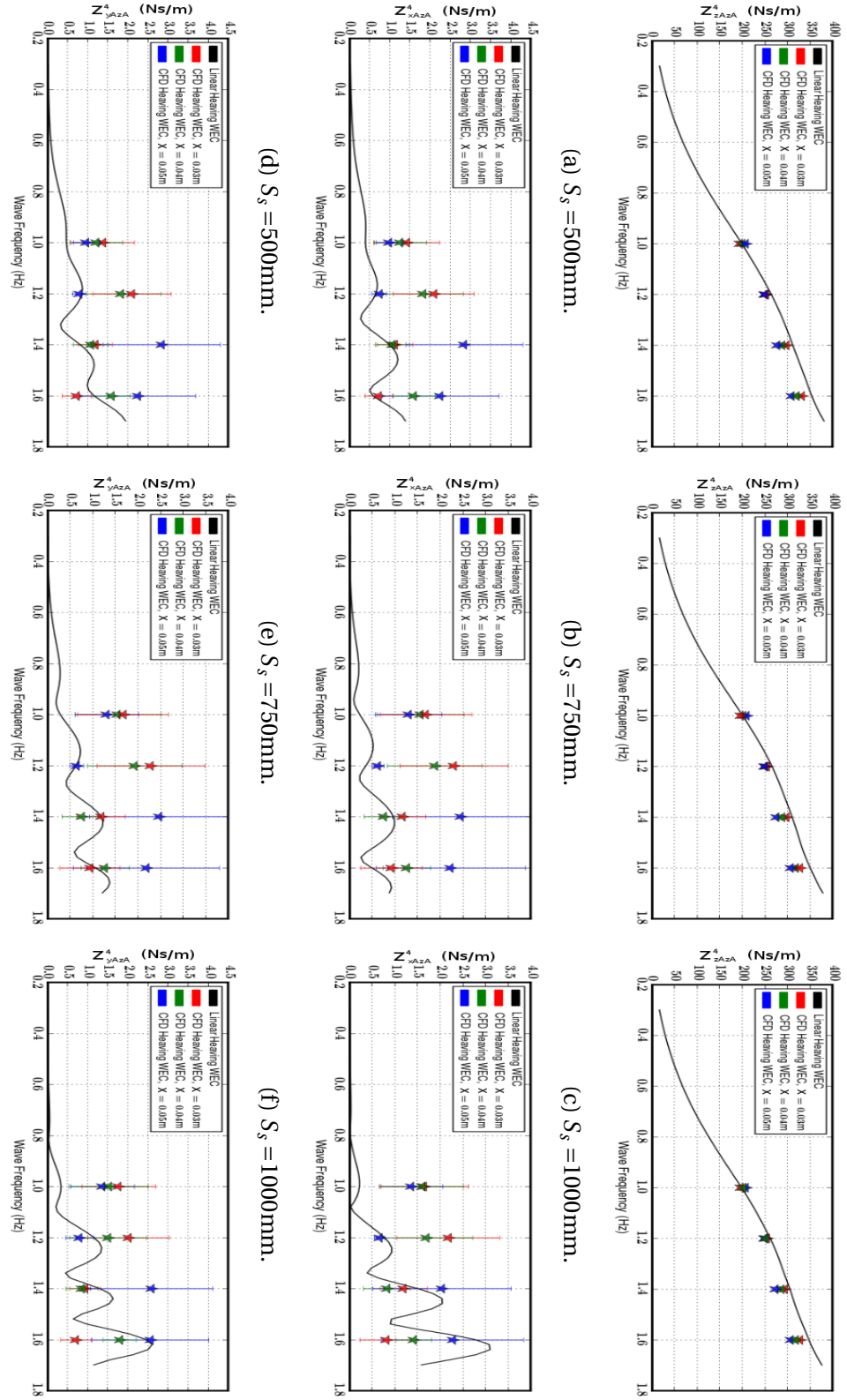

(a) S_s =500mm. (b) S_s =750mm. (c) S_s =1000mm.

(d) S_s =500mm. (e) S_s =750mm. (f) S_s =1000mm.

(g) S_s =500mm. (h) S_s =750mm. (i) S_s =1000mm.

Fig. 4.4 Comparisons of linear FEM and CFD hydrodynamic forcing on the heaving WEC in the Four WEC array.

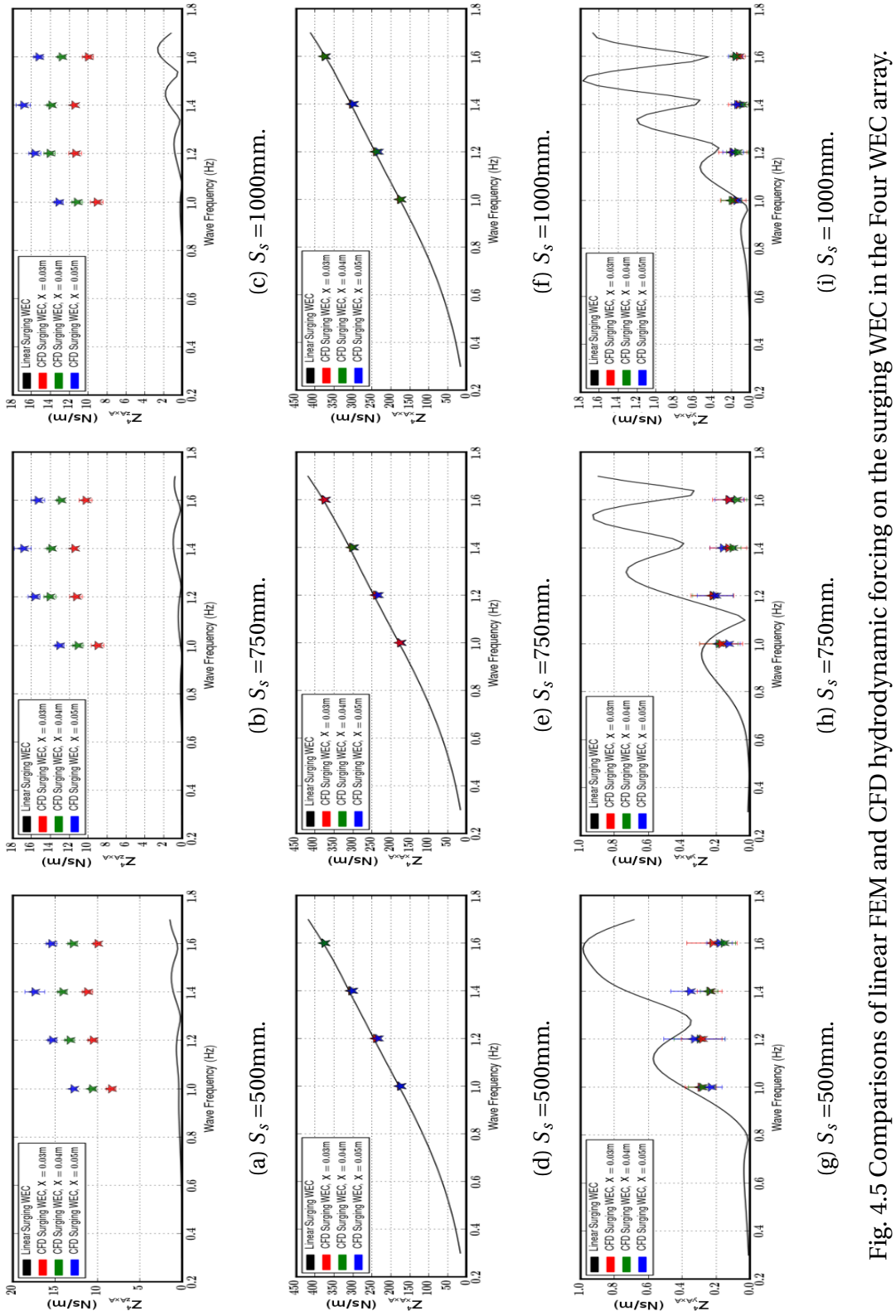

(a) S_s =500mm. (b) S_s =750mm. (c) S_s =1000mm.

(d) S_s =500mm. (e) S_s =750mm. (f) S_s =1000mm.

(g) S_s =500mm. (h) S_s =750mm. (i) S_s =1000mm.

Fig. 4.5 Comparisons of linear FEM and CFD hydrodynamic forcing on the surging WEC in the Four WEC array.

finite WEC motions. The next step in this analysis is to investigate the radiation impedance appearing on the stationary WECs in both array configurations.

4.3.2 Radiation Impedance Coefficients for the Stationary WECs

In the following section we aim to investigate the radiation impedance coefficients appearing on the stationary WECs in both array configurations due to the radiated wave from the active WEC. In the results that follow the array interaction becomes apparent as the strong forces stemming from WEC motions are not present.

Two WEC Array

In the two WEC array we have only to analyze the resulting forcing on a single WEC. For both Z^2_{i1xA} and Z^2_{i1zA} we have good agreement between linear and CFD results for both $i = x, z$ with RSME values given in Appendix B.2 Table B.7. In most cases we have consistent results at all amplitudes giving low variability with exception. Particularly cases shown in Figs. 4.6f, 4.7b and 4.7c we have high variability in the results consistently across each tested oscillation amplitude. The mean values however in general tend to agree with linear findings. From the results in Figs. 4.6 and 4.7 we can conclude that the interaction through the array is well represented in CFD.

Four WEC Array

The four WEC array contains significantly more interaction between each WEC. We however see excellent agreement between the calculated Z^4_{minA} in CFD and linear results for $m = x, y, z$, $i = 1, 2, 3$ and $n = x, z$. For a Z^4_{mizA}, Fig. 4.8 shows radiation impedance coefficients for each stationary WEC in the array. Values Z^4_{zizA}, for $i = 1, 2$ in this configuration are identical due to symmetry and both linear and CFD results give this relation. We see very little dependence on the oscillation amplitude of the active WEC and the variations and the frequency dependence of Z^4_{minA} are captured well in CFD with RMSE values given in Appendix B.2.

The reciprocity relation makes Z^4_{x1zA} and Z^4_{y2zA} equivalent and this can be seen clearly in the linear results as well at those calculated from CFD. We can infer from the general agreement between CFD and linear results that the nonlinear behaviour between the heaving active WEC and the free surface does not significantly propagate through arrays with the S_s values studied here. This would be an encouraging result giving that the nonlinear behaviour of one device has a negligible effect on another. However it should be noted that this CFD modelling approach has decoupled the nonlinear effects which

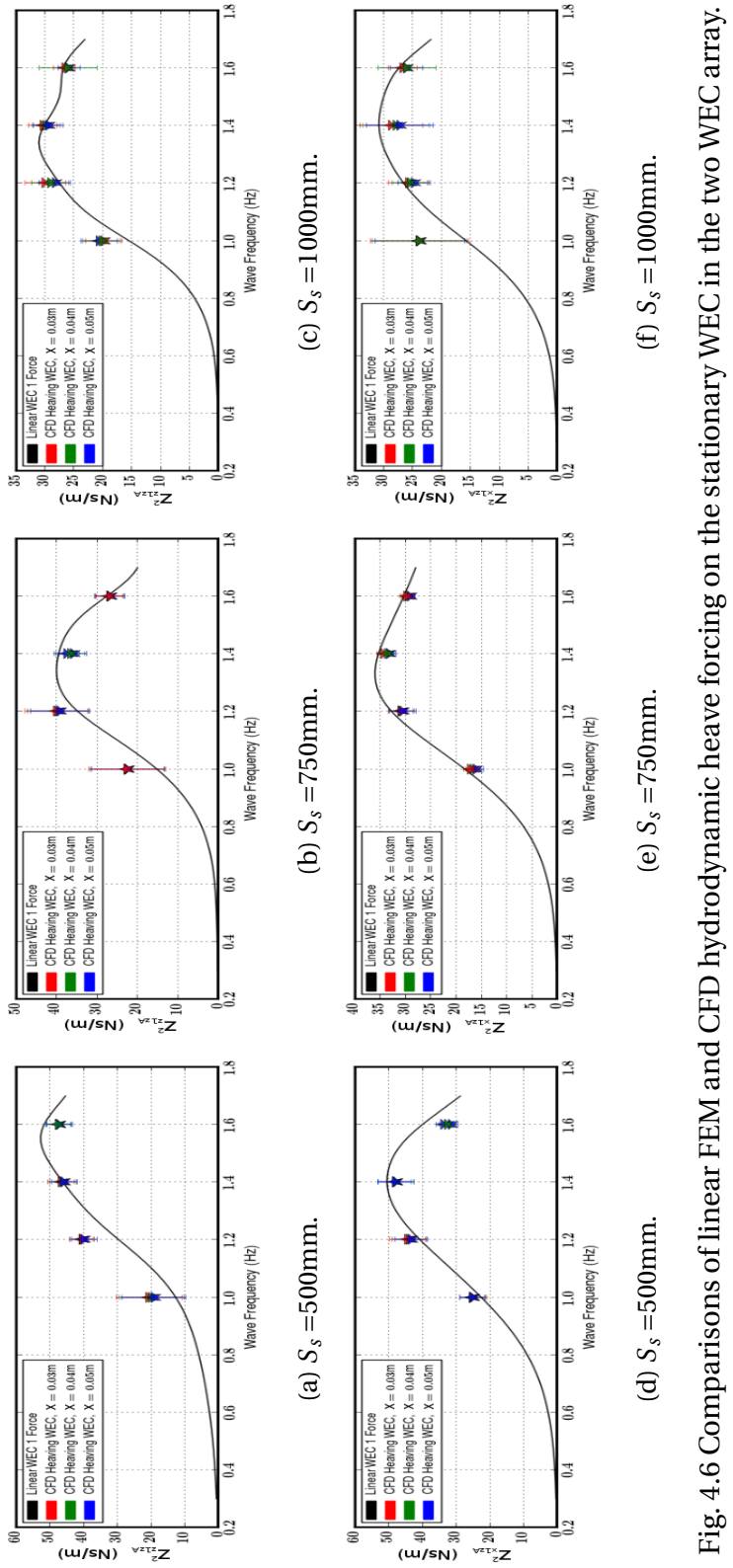

(a) S_s =500mm. (b) S_s =750mm. (c) S_s =1000mm.

(d) S_s =500mm. (e) S_s =750mm. (f) S_s =1000mm.

Fig. 4.6 Comparisons of linear FEM and CFD hydrodynamic heave forcing on the stationary WEC in the two WEC array.

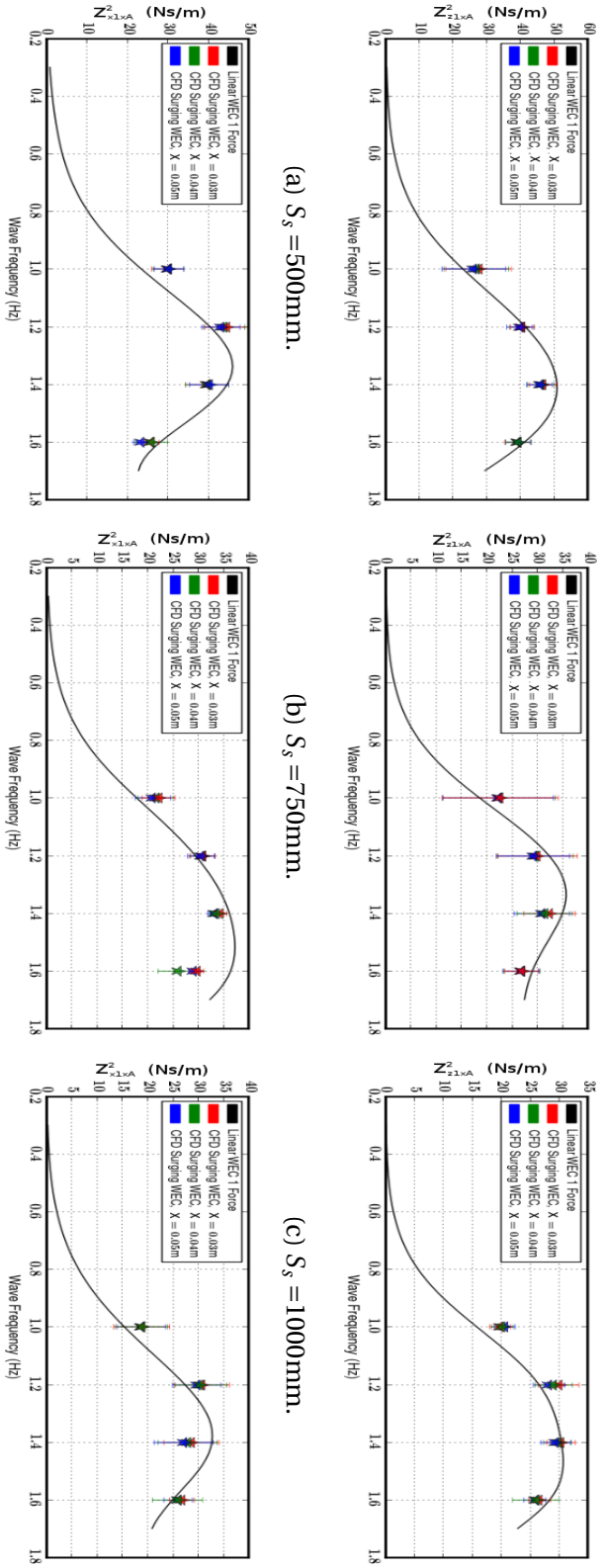

(a) $S_s = 500$mm. (b) $S_s = 750$mm. (c) $S_s = 1000$mm.

(d) $S_s = 500$mm. (e) $S_s = 750$mm. (f) $S_s = 1000$mm.

Fig. 4.7 Comparisons of linear FEM and CFD hydrodynamic surge forcing on the stationary WEC in the two WEC array.

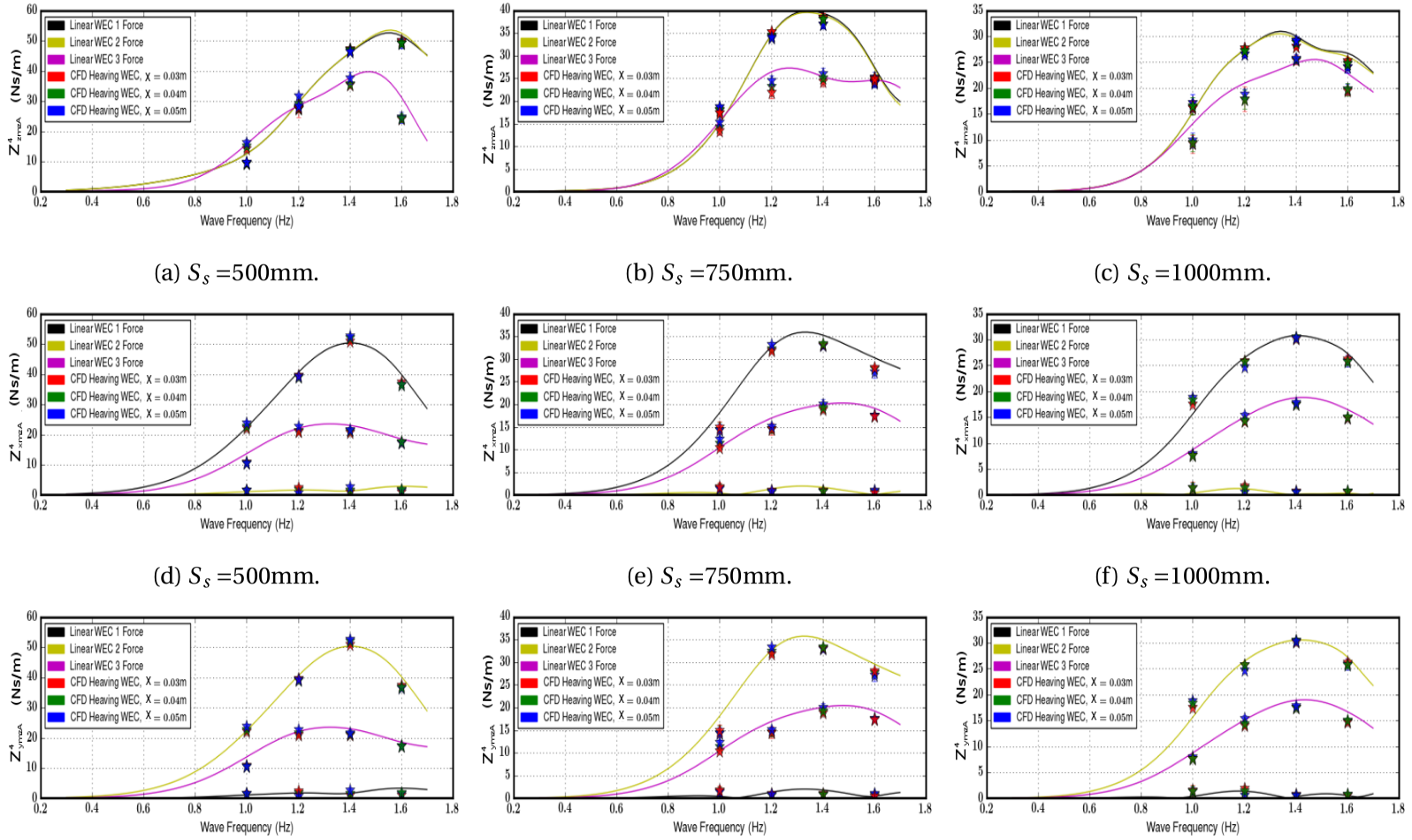

(a) S_s =500mm. (b) S_s =750mm. (c) S_s =1000mm.

(d) S_s =500mm. (e) S_s =750mm. (f) S_s =1000mm.

(g) S_s =500mm. (h) S_s =750mm. (i) S_s =1000mm.

Fig. 4.8 Comparisons of linear FEM and CFD hydrodynamic forcing on the stationary WEC in the four WEC array with a heaving active WEC.

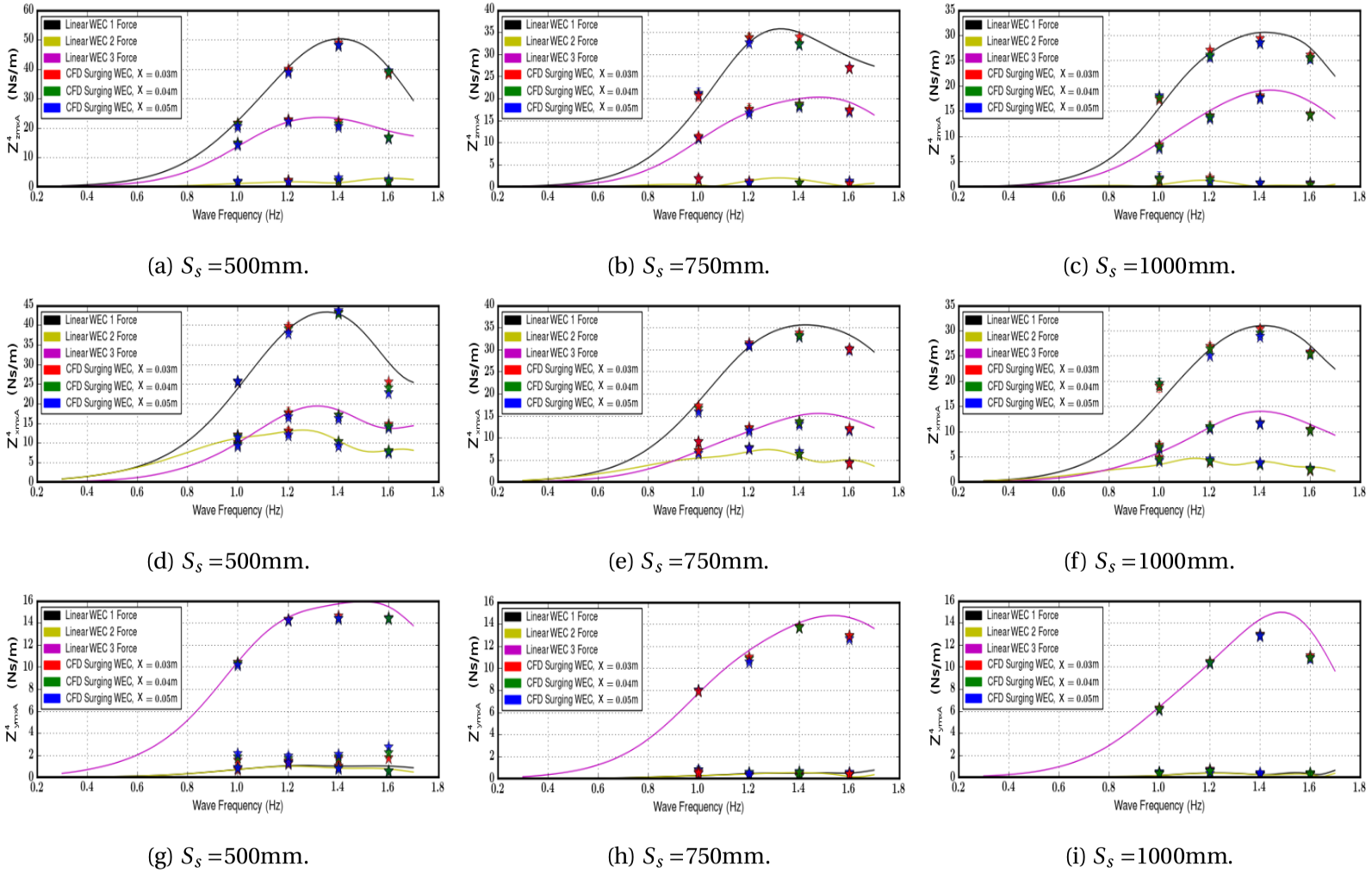

(a) S_s =500mm. (b) S_s =750mm. (c) S_s =1000mm.

(d) S_s =500mm. (e) S_s =750mm. (f) S_s =1000mm.

(g) S_s =500mm. (h) S_s =750mm. (i) S_s =1000mm.

Fig. 4.9 Comparisons of linear FEM and CFD hydrodynamic forcing on the stationary WECs in the four WEC array with a surging active WEC.

would be generated by multiple oscillating WECs, and will be discussed further in the following section.

Results shown in Fig. 4.9 we have no reciprocity relations however, from the symmetry in the problem we know that the Z^4_{z1xA} is equivalent to Z^4_{x1zA} and Z^4_{y2zA}. This relates Figs. 4.9a, 4.9b and 4.9c directly to Figs. 4.8d, 4.8e and 4.8f respectively. It is clear from the results that this relationship between the heaving and surging active WEC is valid in both the linear and CFD models. The results for the radiation impedance in this case follow the trends of linear modelling very well. There appears however to be a consistent discrepancy at high oscillation frequency in the sway forcing. The variance from the linear results is not large however but is one of the few notable deviations in the square array.

Summary

In general we see good agreement between linear model and CFD results for the forcing on the stationary WECs in the arrays. The nonlinear behaviour that is generated from the heaving WEC interacting with the free surface does not appear to impact the forcing results on the other WECs in the array. We can conclude from these results that the radiated waves coming from either a heaving or surging WEC at first order are well represented by linear models. The following section looks closer at the flows and wave fields generated by the radiating WEC in the arrays.

4.4 Free Surface Behaviour

This section aims to investigate the flows and wave fields which are created by the heaving and surging WECs in the two and four device arrays. From previous work in 2, [10] we know that the heaving WECs have a strong nonlinear interaction with the free surface as they begin their downward motion in their oscillation. From Section 4.3.2, we have seen that this nonlinear behaviour has a minimal impact on the forcing appearing on the stationary WECs in the arrays. In Fig. 4.10 we see a vertical slice of the free surface and fluid velocities in line with the two WEC array at a spacing of 1000mm. We can clearly see the jet of upward moving fluid forming as the WEC begins the downward motion. The large fluid velocities created by this process however do not appear to extend far from the active WEC itself and it is clear that this process has little effect on the adjacent WEC.

In Fig. 4.11 we see the same condition with the heaving WEC however with $S_s = 500$mm. Here we again see the fluid motions above the heaving WEC generated by the proximity of the free surface but we continue to see that these motions do not appear to interact dramatically with the WEC closer in. This lack of fluid velocity interaction between the

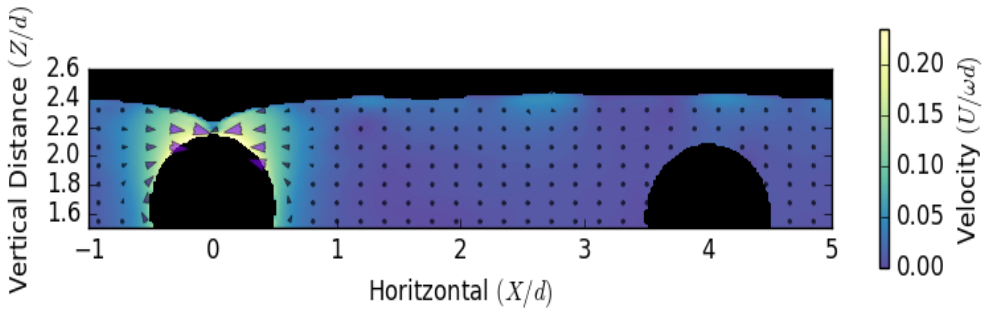

(a) Initial downward motion of the heaving WEC.

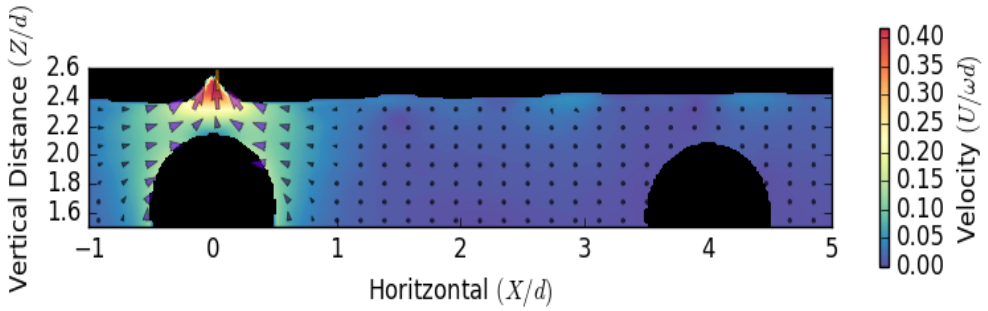

(b) Resulting vertical jet of fluid from the downward motion of the heaving WEC.

Fig. 4.10 The nonlinear free surface interaction between a heaving WEC with oscillation amplitude $x = 50$mm in the two WEC array with S_s =1000mm.

WECs is what we would expect given the forcing results from the previous section. If the sub surface velocities had a significant impact on the stationary WECs in an array we would expect there to be distinct variations in the forcing that would diminish with increasing S_s. From these depictions of the sub surface velocities however we know that there would be a point for the spherical WECs $S_s \lesssim 500$mm where the velocities from an oscillating WEC will effect the others in the array.

Now considering a surging active WEC, shown in Fig. 4.12. For the surging WEC we see from previous work, 2 and the active WEC forcing results from Section 4.3.1 that this device tends to perform very closely to what is predicted from linear models. Little free surface interactions occur to disrupt the wave field and we can see in Figs. 4.12a and 4.12c that the flows are equal and opposite at the points of larges WEC velocity in both fore and aft directions. At the turn around point of the oscillation closes to the stationary WEC, in Fig. 4.12b we can see that the flows around the active WEC have subsided with the dominant motions being attributed to the radiated wave itself close to the free surface.

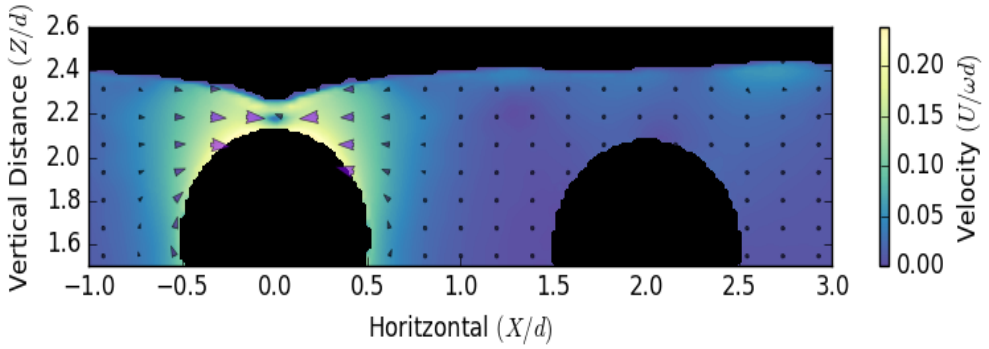

(a) Initial downward motion of the heaving WEC.

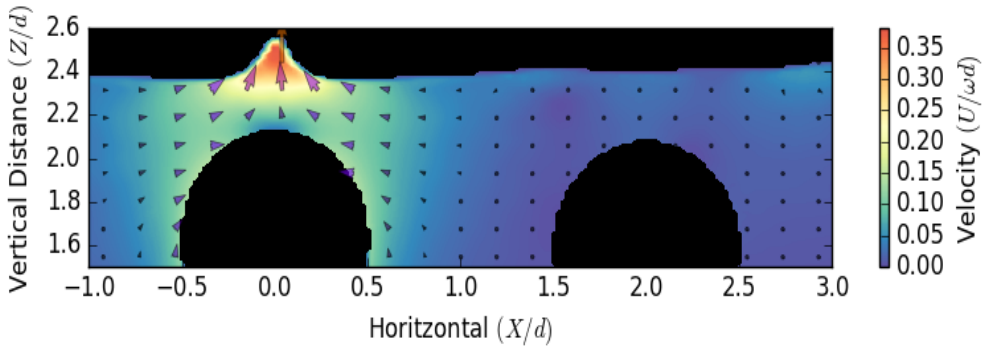

(b) Resulting vertical jet of fluid from the downward motion of the heaving WEC.

Fig. 4.11 The nonlinear free surface interaction between a heaving WEC with oscillation amplitude x = 50mm in the two WEC array with S_s =500mm.

This behaviour mirrors the implementation of the linear surge boundary condition which give validity to linear techniques operating under these conditions.

With the free surface time series data generated through CFD we can apply FFT analysis to investigate the wave fields within the WEC arrays. In Figs. 4.13 and 4.14 we can see the first and second order wave fields for both a heaving and surging WEC at 1.0Hz oscillating frequency an 50mm oscillating amplitude in the square array configuration. In Fig. 4.13a we see the monopolar radiated wave propagating from the active WEC. Subtle diffraction patterns can be seen near stationary WECs one and two which appear to create a small amount of destructive interference closer to WEC three. At second order, shown in Fig. 4.13b we see that the amplitudes of these wave diminish considerably before they reach the stationary WECs in the arrays. This is expected given the results from the previous section which did not capture significant effects on the force from high-order wave interactions. Form the dissipation of the second order wave we can again conclude that higher-order effects from the nonlinear free surface behaviour around a heaving WEC would become

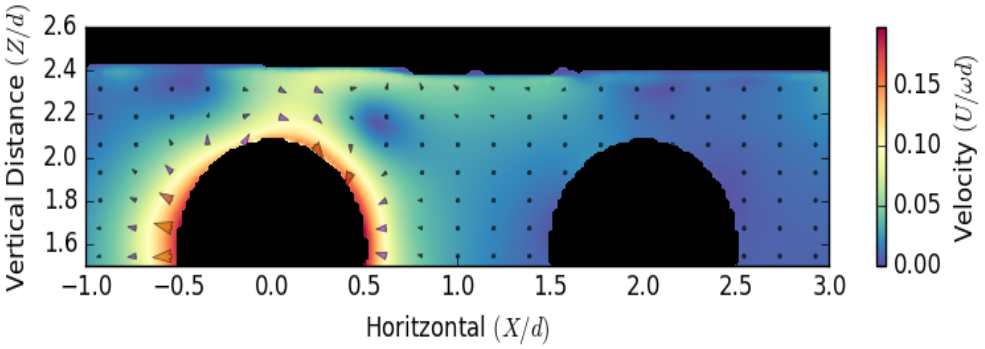

(a) Fluid velocities surrounding the surging WEC at peak positive velocity.

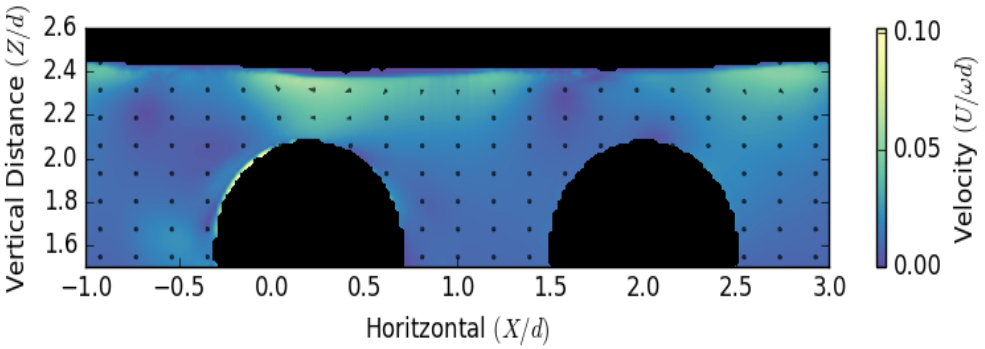

(b) Fluid velocities surrounding the surging WEC at peak positive displacement.

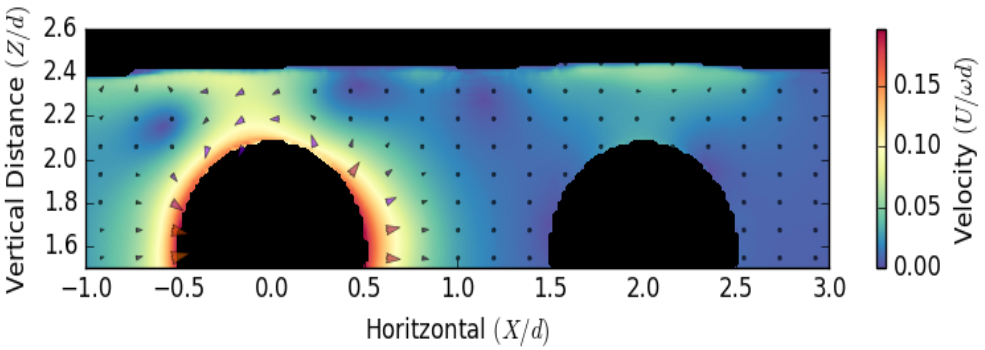

(c) Fluid velocities surrounding the surging WEC at peak negative velocity.

Fig. 4.12 Fluid velocities surrounding a surging WEC with oscillation amplitude $x = 50$mm and S_s =500mm

important is the WECs in these arrays were positioned closer together.

For a surging active WEC, Figs. 4.14a and 4.14b we can clearly see the dipolar radiation patter that is indicative of this type of WEC motion. At first order we can see an area perpendicular to the direction or oscillation where there is no radiating wave, however at

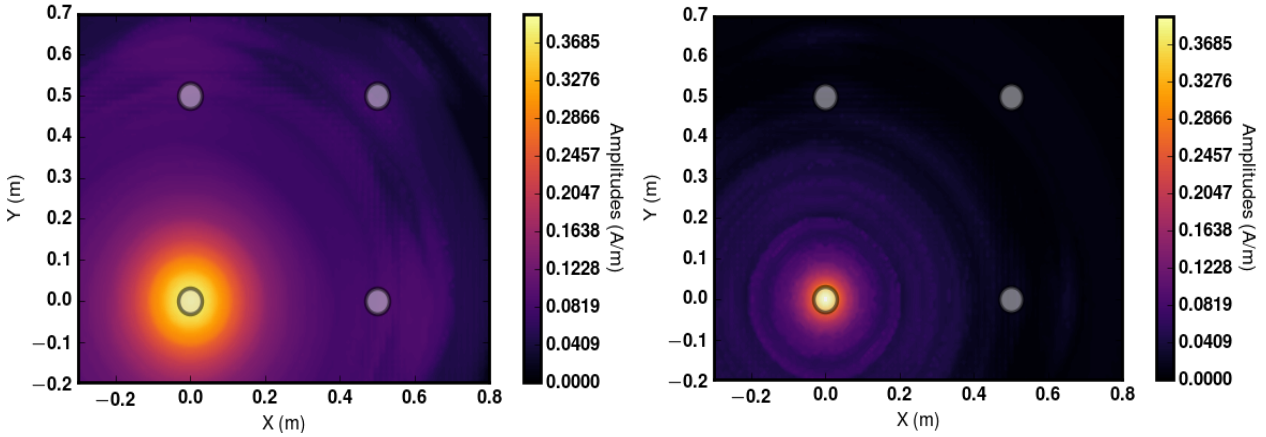

(a) First order normalised free surface amplitudes for a heaving WEC.

(b) Second order normalised free surface amplitudes for a heaving WEC.

Fig. 4.13 First and second order normalised free surface amplitudes for the square array with S_s =500mm.

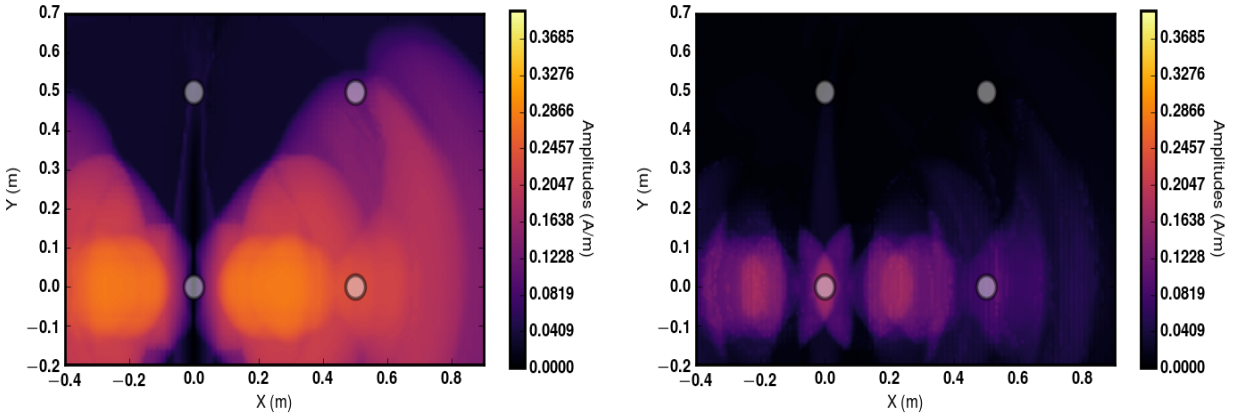

(a) First order normalised free surface amplitudes for a surging WEC.

(b) Second order normalised free surface amplitudes for a surging WEC.

Fig. 4.14 First and second order normalised free surface amplitudes for the square array with S_s =500mm.

second order we can see that there is a wave propagating along this channel. This would suggest that for a surging devices in a row perpendicular to their motions would interact with each other primarily through their second order radiated wave fields. The amplitude of this second order wave however is small next to the oscillating amplitude of the device and would have little impact on another device particularly in a real sea situation where the wave field is far more complex.

Summary

This section investigated the fluid velocities and wave fields surrounding the heaving and surging active WECs. The heaving motions, as seen in previous work, creates strongly nonlinear fluid motions as it oscillates near the free surface, but it has been shown that the sub surface velocities and second order radiated wave do not interact with the other WECs in the arrays tested here. These higher-order effects would become important however if the devices where positioned closer to each other. The surging device was seen to project a second order wave field perpendicular to the direction of oscillation indicating that surging devices along this line would interact more so through second order effects rather than at first order. This wave however is not large and so it's impact would be minimal particularly if the WECs are spaced far appear. The next phase of the analysis of the arrays tested here is to consider the q-factors and test their performance against isolated devices. That analysis following in the next sections.

4.5 Q-Factors

The q-factor is a common quantity used to assess the effects of interaction between WEC devices against that of a number of singular isolated devices. From the previous sections we have seen that the interactions due to radiation at first order calculated through CFD are quite comparable to that predicted from linear theory. Using results presented in [8] for the diffraction excitation force coefficients and single device values generated from the model presented in [10] we can calculate the q-factor values from the CFD array. The CFD calculated values for heaving and surging WECs are shown in Figs. 4.15 and 4.16 respectively along side the linear FEM calculated values.

In Fig. 4.15 we can see a clear sign of strong constructive interaction which appears at lower kd and slightly lower magnitude with a more separated array. The trends in CFD are similar to those from the linear model but in the cases where we expect significant gains in the q-factor we on average do not see this replicated in CFD. The benefits of the array however (q-factor> 1) are present in the CFD results. The fluctuations in excitation force amplitude along with losses due to free surface interaction, viscosity and turbulence would all contribute to variation in CFD away from linear results. With the general trends of the linear model appearing in CFD we can conclude that the constructive benefits of the array continue to persist even with the presence of nonlinear losses for a heaving device.

For an array of surging devices shown in Fig. 4.16 we see a similar outcome. From the linear model we do not have the distinct point of strong constructive interference over all array spacings but so however see considerable interaction when the array is closely

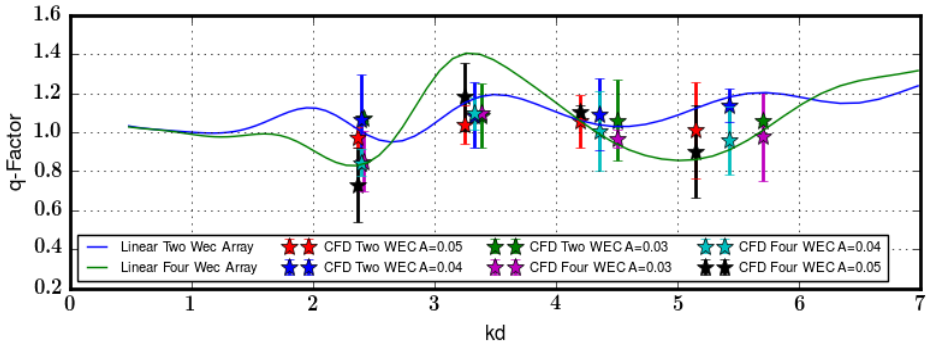

(a) S_s =1000mm.

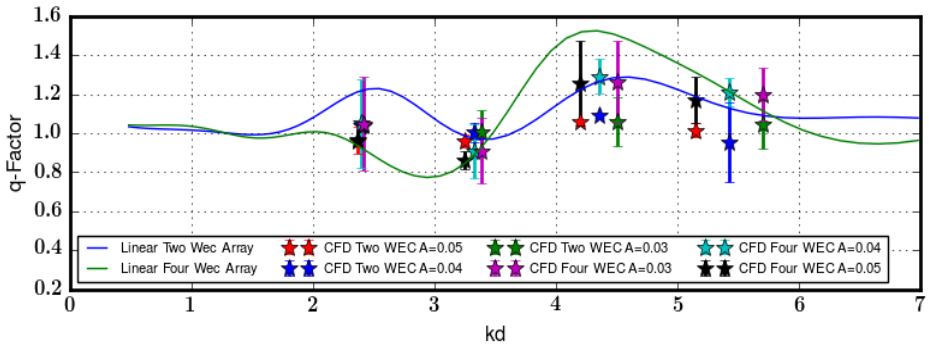

(b) S_s =750mm.

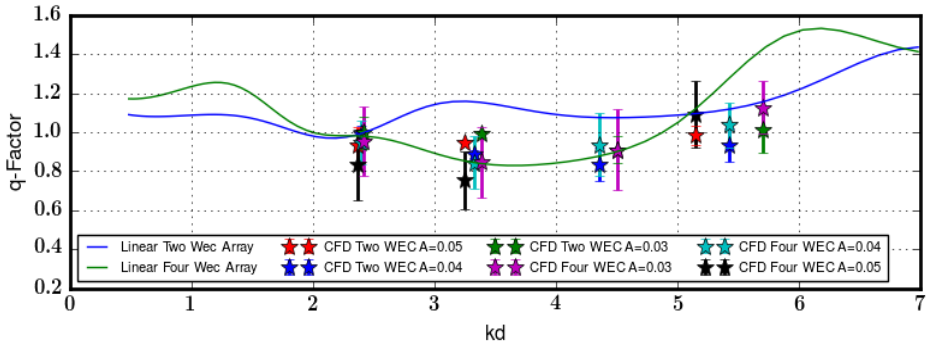

(c) S_s =500mm.

Fig. 4.15 q-Factors for an array of heaving WECs following eqn. 1.12.

spaced (Fig. 4.16c). CFD shows again the constructive benefit of the array at close spacing and low kd but again not to the extent predicted by the linear model. For larger spacings the trends given from the linear model are in general seen in CFD showing the interaction of the devices. However the variability of the WEC forcing suggests that the diffracted and radiated wave interaction leading to these interference benefits are not so clear or stable.

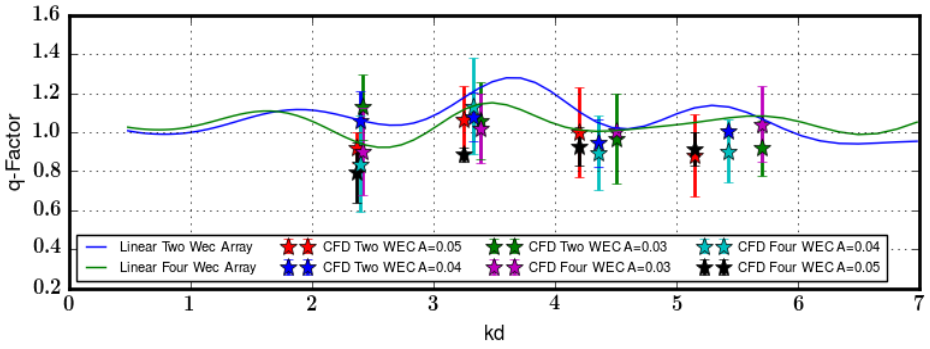

(a) S_s =1000mm.

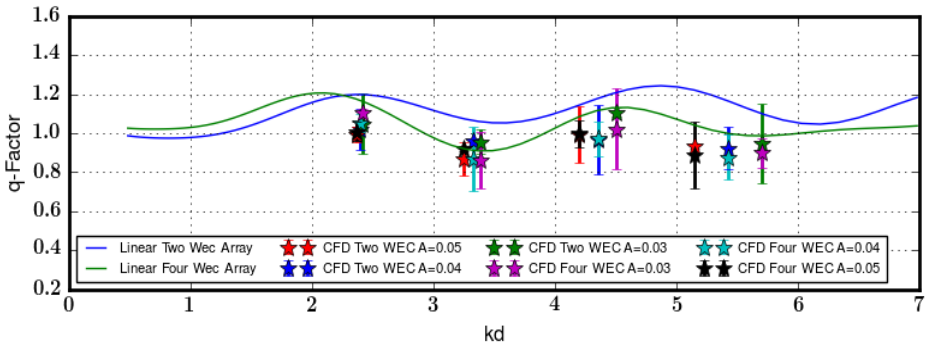

(b) S_s =750mm.

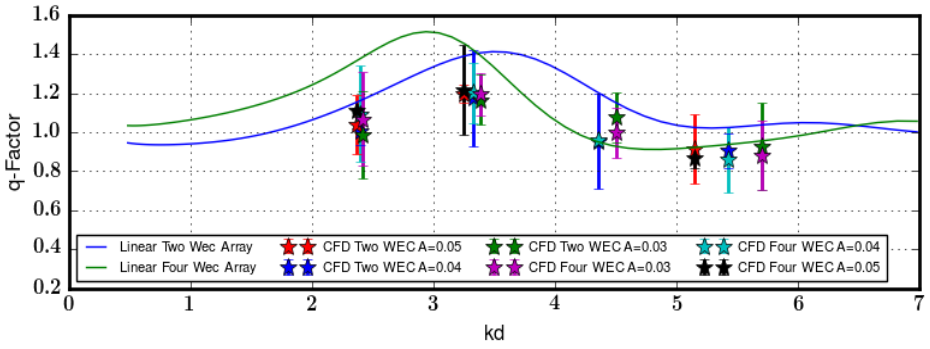

(c) S_s =500mm.

Fig. 4.16 q-Factors for an array of heaving WECs following eqn. 1.12.

In general however the linear interference benefits of a WEC array predicted in linear theory is seen in CFD with the inclusion of nonlinear free surface and viscous effects. From this we can conclude that there are considerable benefits to creating WEC arrays versus several singular isolated devices however this work has shown that their interaction is far more complicated compared to what is predicted from pure linear modelling.

4.6 Conclusions

This work applies a 3D nonlinear, SST URANS VOF CFD model to simulate the radiation problem for arrays of generic spherical WECs. The arrays tested here consist of two WECs in a row and four WECs in a square with sphere separations of 500mm, 750mm and 1000mm. The active WEC oscillation amplitudes used here were 30mm, 40mm and 50mm with frequencies of 1.0Hz, 1.2Hz, 1.4Hz and 1.6Hz. A linear FEM model was adapted to this problem and the results were used to characterises the validity of the outputs from CFD. Applying this fully nonlinear model to analyze the radiation problem for WECs gives valuable insight into the PTO potential and interaction of WECs operating in close proximity. It has been shown in this work that the forcing appearing on the oscillating and stationary WECs in each array compare well to the linear predictions and vary considerable only in cases where we have significant free surface interaction which is expected from previous work.

Chapter 5 has been removed for copyright or proprietary reasons.

Chapter 5

Nonlinear Modelling of a Damped Generic Wave Energy Converter in Resonance

This chapter consists of work that has been presented and published at the European Wave and Tidal Energy Conference 2017. The Conference publication here has been edited, altering the introduction, theory and conclusion sections but is otherwise unchanged from the original article.

Bharath, A., Nader, J-R., Penesis, I., Macfarlane, G. (2017). Nonlinear Modelling of a Damped Generic Wave Energy Converter in Resonance. In *12^{th} European Wave and Tidal Energy Conference.*

Chapter 6

Conclusions and Future Work

6.1 Conclusions

6.1.1 General Conclusions

The use of a VOF CFD approach to model a WEC has clearly shown the importance and subtlety of true nonlinear effects on flow dynamics. The aim of this study was to investigate the nonlinear effects that impact linear solutions. To that end, the separability of the diffraction and radiation problems was maintained eliminating nonlinear coupling. Specific dynamics such as wave breaking could then be attributed directly to each aspect of the full problem. This method allows for a greater understanding of how a device will operate in real ocean waves. In particular breaking waves are found to be a consistent factor for the generic WEC decreasing the overall excitation force on the device and dissipate the energy available in the waves. This method of WEC analysis has the potential to extend linear results to produce a better understanding of the power available to a PTO system.

In general, the use of CFD to study WECs is still a time consuming process. Combination with linear models is still necessary to determine the simplified performance of a device which can be used to find points where focussed studies can be done with CFD. CFD simulation meshes must be carefully tuned in order to resolve the desired effects. Through mesh development the largest contribution to mesh sizes is resolving the free surface. Many numerical methods, described in the previous chapters, are designed to reduce mesh sizes and therefore run times however introducing more complicated wave fields, such as irregular or superposed waves, care needs to be applied to ensure each frequency is resolved correctly. This work however has shown that modern CFD is capable of simulating WEC arrays in a reasonable time span. Given an understanding of

the conditions that are of interest to developers, it is feasible to complete a detailed study efficiently and quickly. What follows below is a detailed account of the findings from each study in this work.

6.1.2 Outcomes from the Single WEC

Chapter 2 applies the CFD VOF model to simulate a single generic WEC operating in both heave and surge. Four regular incident waves and oscillation amplitudes of 30-60mm with frequencies of 0.8-1.2Hz were considered. A linear FEM model [47, 45] was adapted to the problem and the hydrodynamic coefficients are presented against CFD and experimental results. Experiments performed at the AMC described in [53, 46] mirroring this case study were used to validate and quantify the uncertainty in numerical values. This novel approach to determine the hydrodynamics of a WEC by invoking linear separability of the diffraction and radiation problems has highlighted free surface effects as a key contributor to nonlinear characteristics of the hydrodynamic forcing. These effects have been seen in full scale numerical testing and could be predicted by applying Froude scaling for a spherical WEC, however would be largely dependent on a WEC design under consideration.

Linear results give the hydrodynamic coefficients across a large range of frequencies which were then used to choose frequencies of interest for CFD and validated by experimental results at low amplitudes. In the diffraction case 30mm (low) wave amplitude cases showed overall good agreement, Fig. 2.11 with experimental and CFD trends however experimental and CFD values were lower near resonance. With increasing wave amplitude, free surface interactions become important with the onset of visible breaking waves, Fig. 2.12 and skewness in the oscillating behaviour of the WEC forcing. An imbalance in the forcing transition times and amplitudes are seen which could impact the motion of a freely moving WEC and hence the PTO. This effect is not resolvable through linear modelling as it would vary with the geometry of the WEC and would be scale dependent.

For the heaving sphere radiation problem, FEM, CFD and experimental impedance results at low amplitudes agree well, Fig. 2.15. The interaction between the WEC and free surface however develop nonlinear breaking waves which contribute to repeatedly skewed upward forcing behaviour shown in Fig. 2.14 and 2.16. Downward forcing values for the radiation impedance are shown to be consistent with the amplitude independent nature of linear predictions. This result substantiates the importance of free surface impact on a WECs dynamics. For the surging sphere radiation problem, there was excellent agreement, Fig. 2.17 with linear FEM and experiments at all frequencies and amplitudes included in this study. The separation between the surging sphere and the free surface was large enough in this study to not induce nonlinear free surface effects and the problem

maintained linearity.

The study of the hydrodynamic coefficients on the generic spherical WEC considered here provides valuable insight into the nonlinear dynamics occuring on submerged point absorber type WECs. The results shown here provide visible data on the limitations for linear modelling techniques however with maximum and mean differences of 16% and 9% offer excellent, quick initial predictions of the overall performance of a WEC. Further investigations are needed to understand the coupling between diffraction and radiation nonlinearities and its impact on a WEC performance. This study shows that the need for more extensive, fully nonlinear CFD studies of WEC devices are necessary to fully understand the loading characteristics on a submerged WEC which are required for further development of the PTO and mooring systems.

6.1.3 Diffraction in WEC Arrays

Chapter 3 applies the CFD VOF model to simulate the diffraction problem for arrays of generic WECs. Arrays of two WECs in a row and four WECs in a square were used with three WEC separations of 500mm, 750mm and 1000mm with incident wave heights of 60mm, 80mm and 100mm and wave frequencies of 1.0Hz, 1.2Hz, 1.4Hz and 1.6Hz. The FEM model [47, 45] was extended with multiple WECs to quantify CFD results. By applying here a fully nonlinear modelling technique to study the diffraction problem for a WEC here gives valuable insight into the excitation force which provides usable energy to WECs operating in close proximity. Significant differences between linear model predictions and subsequent CFD results shown here suggest that nonlinear effects will greatly impact the performance of a WEC array.

The study of two WECs in a row showed that the upstream WEC has a direct impact on the excitation forces experienced by the downstream WEC. From Section 3.4.1, the upstream WEC excitation force for low incident wave heights of 30mm, are in close agreement with FEM predicted values. However, it is clear from the results that the excitation force values decrease with increasing incident wave amplitude. The downstream WEC however experiences large variations in excitation forces from wave to wave. This can be attributed to breaking waves generated by the upstream WEC acting on the downstream WEC. Also, the variations of the free surface affect the sub-surface flow fields which propagate downstream. This reduces the overall performance of the array but as shown in Section 3.5, it is still possible to gain the excitation force benefits of the array increasing PTO.

The study of four WECs in a square array is more susceptible to the nonlinear behaviour, hence reducing the overall performance of the array. The results presented in

Section 3.4.2 show the same variations on the downstream WEC as seen in the two in a row WEC array. The decreases in the mean excitation forces in both heave and surge however are considerably lower for this configuration. Similar breaking waves are produced by the upstream WEC and propagate downstream, however the perpendicular propagation of the diffracted wave shown in Fig. 3.10 acts to compound the nonlinear effects. The array excitation forces shown in Section 3.5 for the four WEC array show considerably lower results than linear models and the two array case. This suggests that introducing more WECs to increase interference effects and boost array performance might have an opposing outcome. These effects would also be strongly dependent on the geometry of the WEC itself but highlights the need for further nonlinear studies of the interaction between a WEC or array of WECs and the incident wave.

6.1.4 Radiation in WEC Arrays

Chapter 4 applies a 3D nonlinear, SST URANS VOF CFD model to simulate the radiation problem for arrays of generic spherical WECs. The arrays tested here consist of two WECs in a row and four WECs in a square with sphere separations of 500mm, 750mm and 1000mm. The active WEC oscillation amplitudes used here were 30mm, 40mm and 50mm with frequencies of 1.0Hz, 1.2Hz, 1.4Hz and 1.6Hz. The linear FEM model was adapted to this problem and the results were used to characterize the validity of the outputs from CFD. Applying this fully nonlinear model to analyze the radiation problem for WECs gives valuable insight into the PTO potential and interaction of WECs operating in close proximity. It has been shown in this work that the forcing appearing on the oscillating and stationary WECs in each array compare well to the linear predictions and vary considerably only in cases where we have significant free surface interaction which is expected from previous work.

The forcing results from both the two and four WEC array configurations show little susceptibility to the nonlinear wave behaviour generated from the heaving oscillating WEC. From Fig. 4.13 and 4.14 we can see that the second order radiated wave has dissipated to a negligible level within the CFD model before it could interact with the nearby WECs. This shows that most of the radiation interaction would be influenced by the first order wave action.

For a surging WEC, CFD results also show considerable heave forcing which is not represented in linear models. This would be due to the subtle difference in modelling techniques in that the motion of the WEC in CFD is not modelled with linear techniques. This heave forcing is strongly dependent on the oscillation amplitude and would impact

the motion of a real device. Considering a WEC with a PTO system operating mainly from the heave motion, if the device oscillates in surge and sway it would induce forces on the PTO which would not be accounted for through linear predictions. This result is thus important to the understanding of the loads on a WEC particularly a heaving point absorber.

The ultimate goal of this study was to calculate the q-factors associated with each array and are given in Figs. 4.15 and 4.16. The general trends from CFD calculated values follow those predicted through linear model results. The large gains expected from linear models are not seen in the phase averaged CFD values, but the construct benefit of the array configuration is still shown.

This study of generic WEC arrays combined with the work in [8] highlight many of the shortcomings of linear modelling techniques in terms of the complex interaction a device has with the environment and the variability of the excitation forces used to generate power. However, it has been shown that linear models do provide accurate representations of these arrays in the configurations studied here. The introduction of nonlinear components particularly through increasing wave heights produce flows around the device which change the form of the wave field in the diffraction case and for radiation produces fluid jets which would have a strong influence on the WECs added mass and ultimately how it travels through the water column. These flows are strongly dependent on the geometry of the device and should be under consideration in the WEC design phase. The modelling methods presented here have the capability of resolving this behaviour and would be an effective way of optimising a WECs design.

6.1.5 Outcomes from a Fully Active WEC

Chapter 5 aimed to help understand the dynamics of a WEC in real conditions will ultimately lead to significantly more detailed knowledge of the capabilities of a device in terms of performance and how a single WEC may influence an array. In this study we simulated a neutrally buoyant generic submerged spherical WEC subject to various incident wave frequencies and restoring force coefficients each with linearly optimised PTO radiation damping. This study aimed to better understand the dynamics and performance of a WEC in real, regular wave conditions. The CFD model used here simulates the motions a WEC would undergo as it begins to move as well as the time taken to settle into regular, linear oscillations.

The WECs with large restoring force coefficients k_h tend to settle into regular oscillations quickly, while a lower value see the WEC drift through the water column reaching points close enough to induce breaking waves (Fig. 5.10). Irregular forcing characteristics

appear on the WEC for large restoring force coefficients due to the proximity of the free surface and the resistance against fluid motion. This irregular forcing increases for large k and lower incident wave frequencies. It can be suggested that this type of behaviour is caused due to the resistance of the WEC to move with the incident waves. This would be consistent with previous findings from [10] which shows strong WEC-free surface interaction with $k_h \to \infty$ at all incident wave frequencies included in the study.

The impact of the WEC on the propagating wave is shown in Section 5.5.2. The proximity of the WEC to the free surface has a discernible impact on the propagating wave as well as the relative velocity produced around the WEC. This interaction would be strongly dependent on the design of the WEC but is not something that can be predicted using a linear modelling approach. The disruption to the incident wave would also have a significant impact on the performance of a WEC array as less incident wave energy is available to subsequent WECs.

6.1.6 Summary

In culmination this work highlights many of the dynamics brought on by nonlinear interaction which impact the performance of a single or array of WECs. In many ways we have seen that linear modelling methods are adequate in predicting the potential performance of WEC arrays. With the added benefit of being able to generate large datasets of results in a short amount of time, linear models will continue to be used heavily to study WEC performance. The general behaviour can be well represented by linear modelling but it is clear from this work that geometrical details nonlinear behaviour which effect the linear solutions can lead to significant hydrodynamic deviations. In the case of an isolated device it was shown that for large (70mm) amplitude waves which break over the device, lead to variations in the sinusoidal nature of the excitation forcing. Given the potential complexity of a PTO control system it may be beneficial to minimise this effect so that it can be excluded in the control system. This could be achieved in many ways, for example, carefully modifying the geometry or positioning the WEC deeper in the water column would limit free surface interactions. When considering deployments in low energy sites having a greater understanding of the dynamics of a WEC could mean the difference between viability or not.

Extending to arrays of WECs we have seen that the breaking wave behaviour has a large impact on the downstream WECs. This is clear when considering that the energy defused from the wave via turbulent breaking drives directional velocities through the system. Having a non-reciprocating flow acting on a device, from the results present here

have a dramatic impact on the excitation force on the downstream devices in an array, particularly in the surge orientation. For larger arrays this loss of wave energy would also result in very little energy available to WECs last in line to the propagating wave. From linear modelling this can occur if the array is large enough to diffract the wave energy away from the last in line WECs but CFD here suggests that energy would be lost in other ways. For larger arrays the effect of energy lost due to wave breaking could compound, resulting in performance values substantially different to those predicted through linear means which shows the need to further examinations of these effects through CFD modelling.

6.2 Recommendation for Future Work

As with all research, specific questions arise which are outside the scope of the current project. Throughout the course of this work many dynamics arose which would be interesting for future studies to extend the capabilities of CFD and progress the understand of WEC arrays. Keeping with a generic type device more detailed investigations of the propagating wave could be done. These points are listed below:

- Propagation and distribution of wave energy over a WEC array.
  - We have seen that wave breaking is a major contributor to the overall nonlinear effects on the WECs. What is unclear is the wave order that looses the most energy when the wave breaks. For the high amplitude work here a Stokes 5^{th} order incident wave was used implying that there are 5 modes oscillating within the wave. It is supposed that the high order components contribute energy to the breaking wave disproportionately to lower orders which could have a nonlinear wave filtering effect. A complete understanding of the wave energy dissipation through an array of WECs could be invaluable when designing a commercial scale wave farm.
- Formation of currents within a WEC array.
  - With energy being lost from the waves, results presented here suggest that directional currents are being driven within the arrays. A better understanding of these currents would assist in WEC performance predictions and also in environmental studies of shorelines and sea floors. In the scope of this study it was not possible to perform a detailed analysis of the progression of these currents as there would require a substantial increase in computational time.

An understanding of the wave energy lost and the currents formed by the presence of a WEC would have a dramatic impact on how an array configuration is chosen. Applying CFD for this would be computationally expensive however is the only computational method to study these problems. If we turn to look at specific WECs currently under development more questions arise which need further research.

- Variable bathymetry and it's effect on WEC dynamics.
  - If we begin to look away from idealised studies and the performance of real devices in intermediate or shallow water, the bathymetric effects become and important an open question. The placement of WECs near continental shelves where we have relatively quick depth changes may have unpredicted consequences which linear modelling methods cannot capture.
- Direct modelling of a PTO control.
  - In this work we modelled a PTO control as only a simple linear damper. This is not an accurate representation of real control system and using CFD methods available within CD-Adapco StarCCM+ it is possible to create a more accurate PTO representation. This would not be a simple task however with the challenge of validation being a large concern. The benefits of understanding the real properties of a PTO system would be an enormous benefit to any WEC developer.

The areas of further investigation identified (not limited to only those above) can help to provide further understanding of the detailed dynamics of a WEC and it's impact on the immediate environment. With the more detailed and complicated models required to achieve the necessary results there will be a large increase in the computational expense however with improvements in technology these will quickly become accessible studies.

References

[1] Agamloh, E. B., Wallace, A. K., and Von Jouanne, A. (2008a). Application of fluid–structure interaction simulation of an ocean wave energy extraction device. *Renewable Energy*, 33(4):748–757.

[2] Agamloh, E. B., Wallace, A. K., and von Jouanne, A. (2008b). Application of fluid–structure interaction simulation of an ocean wave energy extraction device. *Renewable Energy*, 33(4):748 – 757.

[3] ANSYS (2013). *Academic Research User Guide*.

[4] ApS, W. D. (2017). Wavedragon. Available at https://energy.gov/eere/articles/calming-waters-impact-turbulence-tidal-energy-systems.

[5] Bai, W. and Taylor, R. E. (2006). Higher-order boundary element simulation of fully nonlinear wave radiation by oscillating vertical cylinders. *Applied Ocean Research*, 28(4):247–265.

[6] Balitsky, P. (2013). Modelling controlled arrays of wave energy converters. Master's thesis, National University of Ireland Maynooth.

[7] Berggren, L. and Johansson, M. (1992). Hydrodynamic coefficients of a wave energy device consisting of a buoy and a submerged plate. *Applied Ocean Research*, 14(1):51–58.

[8] Bharath, A., Nader, J.-R., Macfarlane, G., and Penesis, I. (2017). Nonlinear modelling of a generic spherical wave energy converter. *Journal of Renewable Energy-Under Review*.

[9] Bharath, A., Nader, J.-R., Penesis, I., and Macfarlane, G. (2016). Non-linear CFD modelling of a submerged sphere wave energy converter. In *3rd Asian Wave and Tidal Energy Conference*, pages 1–10.

[10] Bharath, A., Nader, J.-R., Penesis, I., and Macfarlane, G. (2018). Nonlinear hydrodynamic effects on a generic spherical wave energy converter. *Renewable Energy*, 118(Supplement C):56 – 70.

[11] Bhinder, M. A., Mingham, C. G., Causon, D. M., Rahmati, M. T., Aggidis, G. A., and Chaplin, R. V. (2009). A joint numerical and experimental study of a surging point absorbing wave energy converter (wraspa). In *ASME 2009 28th International Conference on Ocean, Offshore and Arctic Engineering*, pages 869–875. American Society of Mechanical Engineers.

[12] Brito-Melo, A., Hofmann, T., Sarmento, A., Clément, A., Delhommeau, G., et al. (2001). Numerical modelling of owc-shoreline devices including the effect of surrounding coastline and non-flat bottom. *International Journal of Offshore and Polar Engineering*, 11(02).

[13] Budar, K. and Falnes, J. (1975). A resonant point absorber of ocean-wave power. *Nature*, 256:478.

[14] CD-Adapco (2013). *CD-Adapco Star CCM+ User Guide*.

[15] Chenari, B., Saadatian, S. S., and Ferreira, A. (2014). Wave energy systems: An overview of different wave energy converters and recommendation for future improvements. In *INTED2014 Proceedings*, pages 6266–6272. IATED.

[16] Child, B., Cruz, J., and Livingstone, M. (2011). The development of a tool for optimising arrays of wave energy converters.

[17] Child, B. and Venugopal, V. (2010). Optimal configurations of wave energy device arrays. *Ocean Engineering*, 37(16):1402–1417.

[18] De Andrés, A., Guanche, R., Meneses, L., Vidal, C., and Losada, I. (2014). Factors that influence array layout on wave energy farms. *Ocean Engineering*, 82:32–41.

[19] Delauré, Y. and Lewis, A. (2003). 3d hydrodynamic modelling of fixed oscillating water column wave power plant by a boundary element methods. *Ocean engineering*, 30(3):309–330.

[20] Delauré, Y. M. (2001). *A hydrodynamic investigation of oscillating water column wave energy converters*.

[21] Eriksson, M., Isberg, J., and Leijon, M. (2005). Hydrodynamic modelling of a direct drive wave energy converter. *International Journal of Engineering Science*, 43(17):1377–1387.

[22] Falnes, J. (2002). *Ocean Waves and Oscillating Systems: Linear Interactions Including Wave-Energy Extraction*. Cambridge University Press.

[23] Ferrant, P., Touzé, D. L., and Pelletier, K. (2003). Non-linear time-domain models for irregular wave diffraction about offshore structures. *International journal for numerical methods in fluids*, 43(10-11):1257–1277.

[24] Fleming, A., MacFarlane, G., Hunter, S., and Denniss, T. (2017). Power performance prediction for a vented oscillating water column wave energy converter with a unidirectional air turbine power take-off. In *The 12th European Wave and Tidal Energy Conference (EWTEC)*, pages 1–7.

[25] Fleming, A. N. (2012). *Phase-averaged analysis of an oscillating water column wave energy converter*. PhD thesis, University of Tasmania.

[26] Giorgi, G. and Ringwood, J. V. (2017). Computationally efficient nonlinear froude–krylov force calculations for heaving axisymmetric wave energy point absorbers. *Journal of Ocean Engineering and Marine Energy*, 3(1):21–33.

[27] Gunn, K. and Stock-Williams, C. (2012). Quantifying the global wave power resource. *Renewable Energy*, 44(Supplement C):296 – 304.

[28] Harris, R. E., Johanning, L., and Wolfram, J. (2004). Mooring systems for wave energy converters: A review of design issues and choices.

[29] Hemer, M. and Griffin, D. (2010). The wave energy resource along australia's southern margin. *Journal of renewable and sustainable energy*, 2(4):043108.

[30] Hirt, C. W. and Nichols, B. D. (1981). Volume of fluid (vof) method for the dynamics of free boundaries. *Journal of computational physics*, 39(1):201–225.

[31] ITTC (1999). International towing tank conference recommended procedures and guidelines - cfd user's guide.

[32] ITTC (2017). Specialist committee on hydrodynamics modelling of marine renewable energy devices. In *Proceedings of 28th International Towing Tank Conference - Volume 1*.

[33] Le Mehaute, B. (2013). *An introduction to hydrodynamics and water waves*. Springer Science & Business Media.

[34] Letournel, L., Ferrant, P., Babarit, A., Ducrozet, G., Harris, J. C., Benoit, M., and Dombre, E. (2014). Comparison of fully nonlinear and weakly nonlinear potential flow solvers for the study of wave energy converters undergoing large amplitude motions. In *ASME 2014 33rd International Conference on Ocean, Offshore and Arctic Engineering*, pages V09BT09A002–V09BT09A002. American Society of Mechanical Engineers.

[35] Li, Y. and Yu, Y.-H. (2012). A synthesis of numerical methods for modeling wave energy converter-point absorbers. *Renewable and Sustainable Energy Reviews*, 16(6):4352–4364.

[36] Liang, C. and Zuo, L. (2017). On the dynamics and design of a two-body wave energy converter. *Renewable Energy*, 101:265–274.

[37] Linton, C. (1991). Radiation and diffraction of water waves by a submerged sphere in finite depth. *Ocean Engineering*, 18(1):61–74.

[38] Luo, Y., Nader, J.-R., Cooper, P., and Zhu, S.-P. (2014). Nonlinear 2d analysis of the efficiency of fixed oscillating water column wave energy converters. *Renewable Energy*, 64:255–265.

[39] Ma, Q., Wu, G., and Eatock Taylor, R. (2001). Finite element simulations of fully nonlinear interaction between vertical cylinders and steep waves. part 2: numerical results and validation. *International Journal for Numerical Methods in Fluids*, 36(3):287–308.

[40] Mann, L. D. (2011). Application of ocean observations & analysis: The ceto wave energy project. pages 721–729.

[41] Martinelli, L., Ruol, P., and Cortellazzo, G. (2012). On mooring design of wave energy converters: the seabreath application. *Coastal Engineering Proceedings*, 1(33):3.

[42] Mavrakos, S. and Kalofonos, A. (1997). Power absorption by arrays of interacting vertical axisymmetric wave-energy devices. *Journal of Offshore Mechanics and Arctic Engineering*, 119(4):244–251.

[43] Mehaute, B. (1976). *An Introduction to Hydrodynamics and Water Waves*. Van Nostrand Reinold.

[44] Menter, F. R. et al. (1994). Two-equation eddy-viscosity turbulence models for engineering applications. *AIAA journal*, 32(8):1598–1605.

[45] Nader, J.-R. (2015). Hydrodynamic analysis and performance of a single fixed circular owc device. In *11th European Wave and Tidal Energy Conference*, pages 1–7.

[46] Nader, J.-R., Fleming, A., MacFarlane, G., Penesis, I., and Manasseh, R. (2017). Novel experimental modelling of the hydrodynamic interactions of arrays of wave energy converters. In *Special Issue: Australian Ocean Renewable Energy Symposium*. International Journal of Marine Energy [Under Review, Submitted 02/05/2017].

[47] Nader, J.-R., Zhu, S.-P., and Cooper, P. (2014). Hydrodynamic and energetic properties of a finite array of fixed oscillating water column wave energy converters. *Ocean Engineering*, 88:131–148.

[48] Nader, J.-R., Zhu, S.-P., Cooper, P., and Stappenbelt, B. (2011). A finite element model for efficiency of a moored floating owc device in regular waves. In *ASME 2011 30th International Conference on Ocean, Offshore and Arctic Engineering*, pages 511–519. American Society of Mechanical Engineers.

[49] Nader, J.-R., Zhu, S.-P., Cooper, P., and Stappenbelt, B. (2012). A finite-element study of the efficiency of arrays of oscillating water column wave energy converters. *Ocean Engineering*, 43:72–81.

[50] Nader, J.-R. P. (2013). Interaction of ocean waves with oscillating water column wave energy convertors.

[51] Payne, G. S., Taylor, J. R., Bruce, T., and Parkin, P. (2008). Assessment of boundary-element method for modelling a free-floating sloped wave energy device. part 1: Numerical modelling. *Ocean Engineering*, 35(3):333–341.

[52] Penalba Retes, M., Mérigaud, A., Gilloteaux, J.-C., and Ringwood, J. (2015). Nonlinear froude-krylov force modelling for two heaving wave energy point absorbers. In *Proceedings of the 11th European Wave and Tidal Energy Conference*. European Wave and Tidal Energy Conference 2015.

[53] Penesis, I., Manasseh, R., Nader, J.-R., De Chowdhury, S., Fleming, A., MacFarlane, G., and Hasan, M. (2016). Performance of ocean wave-energy arrays in australia. In *Proceedings of the 3rd Asian Wave and Tidal Energy Conference*, volume 1, pages 246–253. Asian Wave and Tidal Energy Conference.

[54] Rafiee, A., Wolgamot, H., Draper, S., Orszaghova, J., Fievez, J., and Sawyer, T. (2016). Identifying the wave energy group for the extreme response of a point absorber wave energy converter. In *3rd Asian Wave and Tidal Energy Conference*, pages 1–8.

[55] Rahman, M. (2001). Effects of diffraction and radiation on a submerged sphere. *International Journal of Mathematics and Mathematical Sciences*, 28(9):499–515.

[56] Şentürk, U., Özdamar, A., and Bornova, I. (2011). Modelling the interaction between water waves and the oscillating water column wave energy device. *Mathematical and computational applications*, 16(3):630.

[57] Sergiienko, N. Y., Cazzolato, B., Ding, B., and Arjomandi, M. (2016). Frequency domain model of the three-tether wecs array.

[58] Wagner, G. (2016). Paris agreement. Available at https://treaties.un.org.

[59] Wu, G. (1995). The interaction of water waves with a group of submerged spheres. *Applied ocean research*, 17(3):165–184.

[60] Wu, J., Shekh, S., Sergiienko, N. Y., Cazzolato, B. S., Ding, B., Neumann, F., and Wagner, M. (2016). Fast and effective optimisation of arrays of submerged wave energy converters. In *Proceedings of the 2016 on Genetic and Evolutionary Computation Conference*, pages 1045–1052. ACM.

[61] Yeung, R. W. (1981). Added mass and damping of a vertical cylinder in finite-depth waters. *Applied Ocean Research*, 3(3):119–133.

[62] Yu, Y.-H., Li, Y., et al. (2011). A rans simulation of the heave response of a two-body floating-point wave absorber. In *The Twenty-first International Offshore and Polar Engineering Conference*. International Society of Offshore and Polar Engineers.

[63] Zheng, C., Shao, L., Shi, W., Su, Q., Lin, G., Li, X., and Chen, X. (2014). An assessment of global ocean wave energy resources over the last 45 a. *Acta Oceanologica Sinica*, 33(1):92–101.

Appendix A has been removed for copyright or proprietary reasons.

Appendix A

Nonlinear CFD Modelling of a Submerged Spherical Wave Energy Converter

This Appendix present the work presented and published at the Asian Wave and Tidal Energy Conference in 2016. The conference publication here is presented unaltered from the original article. This work is left out of the main body of the thesis owing to the similarities with the work given in Chapter 2.

Bharath, A., Nader, J-R., Penesis, I., Macfarlane, G. (2016). Nonlinear CFD Modelling of a Submerged Spherical Wave Energy Converter. In 3^{rd} *Asian Wave and Tidal Energy Conference*

Appendix B

RMSE Values

B.1 RMSE Values for the Diffraction Problem

B.1.1 Two WEC Array RMSE Values

Table B.1 RMSE between the linear model and CFD heave results for the upstream and downstream WECs.

		RMSE (N/m)		
S_s	**WEC**	**30mm**	**40mm**	**50mm**
500mm	**Upstream**	2.270	4.476	8.030
	Downstream	8.264	10.911	21.644
750mm	**Upstream**	1.021	2.980	8.882
	Downstream	7.484	7.990	18.819
1000mm	**Upstream**	2.360	2.992	9.301
	Downstream	7.216	6.483	21.937

Table B.2 RMSE between the linear model and CFD surge results for the upstream and downstream WECs.

		RMSE (N/m)		
S_s	**WEC**	**30mm**	**40mm**	**50mm**
500mm	**Upstream**	2.270	4.476	8.030
	Downstream	8.264	10.911	21.644
750mm	**Upstream**	12.350	10.137	18.053
	Downstream	23.248	18.314	31.337
1000mm	**Upstream**	10.769	7.788	17.740
	Downstream	19.822	17.076	29.275

Table B.3 RMSE between the linear model and CFD heave results for the upstream and downstream WECs.

		RMSE (N/m)		
S_s	**WEC**	**30mm**	**40mm**	**50mm**
500mm	**Upstream**	7.983	6.659	10.456
	Downstream	8.264	10.911	21.644
750mm	**Upstream**	3.096	4.241	11.996
	Downstream	4.715	6.654	14.712
1000mm	**Upstream**	4.627	5.609	11.067
	Downstream	9.932	7.026	20.109

Table B.4 RMSE between the linear model and CFD surge results for the upstream and downstream WECs.

		RMSE (N/m)		
S_s	**WEC**	**30mm**	**40mm**	**50mm**
500mm	**Upstream**	9.485	6.928	26.439
	Downstream	14.485	18.282	31.439
750mm	**Upstream**	11.169	10.149	20.705
	Downstream	17.443	15.005	33.105
1000mm	**Upstream**	12.252	9.029	22.473
	Downstream	26.473	24.158	39.380

Table B.5 RMSE between the linear model and CFD surge results for the upstream and downstream WECs.

		RMSE (N/m)		
S_s	**WEC**	**30mm**	**40mm**	**50mm**
500mm	**Upstream**	2.861	1.985	2.064
	Downstream	1.6252	2.224	4.663
750mm	**Upstream**	0.738	1.9173	2.400
	Downstream	5.650	5.645	6.488
1000mm	**Upstream**	1.533	2.315	2.358
	Downstream	6.622	6.587	6.626

Table B.6 RMSE between the linear model and CFD heave results for the upstream and downstream WECs.

		Mean RMSE (N/m)	
Amplitude (m)	**WEC Motion**	**Heave**	**Surge**
30mm	**Heave**	15.748	1.290
	Surge	12.354	4.290
40mm	**Heave**	18.093	1.309
	Surge	16.484	3.971
50mm	**Heave**	24.360	1.798
	Surge	19.216	4.872

B.1.2 Four WEC Array RMSE Values

B.2 RMSE Values for the Radiation Problem

B.2.1 Two WEC Array

Mean RMSE Values on the Active WEC

Mean RMSE Values on the Stationary WEC

Table B.7 RMSE between the linear model and CFD heave results for the upstream and downstream WECs.

		Mean RMSE (N/m)	
Amplitude (m)	**WEC Motion**	**Heave**	**Surge**
30mm	**Heave**	4.594	3.392
	Surge	4.290	6.290
40mm	**Heave**	4.932	3.642
	Surge	4.809	7.971
50mm	**Heave**	5.192	3.786
	Surge	5.342	6.822

B.2.2 Four WEC Array

Mean RMSE Values on the Active WEC

Table B.8 RMSE between the linear model and CFD results on the active WEC.

		Mean RMSE (N/m)		
Amplitude (m)	**WEC Motion**	**Heave**	**Surge**	**Sway**
30mm	**Heave**	15.267	10.290	1.354
	Surge	1.543	3.560	0.218
40mm	**Heave**	19.533	12.709	1.908
	Surge	1.484	3.971	0.295
50mm	**Heave**	26.309	14.058	1.054
	Surge	1.216	4.872	0.310

Mean RMSE Values on the Stationary WECs

Table B.9 RMSE between the linear model and CFD results on stationary WEC 1.

		Mean RMSE (N/m)		
Amplitude (m)	**WEC Motion**	**Heave**	**Surge**	**Sway**
30mm	**Heave**	2.431	3.281	1.910
	Surge	3.543	2.560	1.594
40mm	**Heave**	2.307	3.391	2.109
	Surge	4.484	2.171	1.695
50mm	**Heave**	2.973	4.012	1.832
	Surge	4.216	2.342	2.010

Table B.10 RMSE between the linear model and CFD results on stationary WEC 2.

		Mean RMSE (N/m)		
Amplitude (m)	**WEC Motion**	**Heave**	**Surge**	**Sway**
30mm	**Heave**	3.647	2.183	1.819
	Surge	3.943	2.593	1.244
40mm	**Heave**	3.298	2.301	1.908
	Surge	3.884	2.876	2.095
50mm	**Heave**	4.839	2.058	1.054
	Surge	3.716	2.782	3.114

Table B.11 RMSE between the linear model and CFD results on stationary WEC 3.

		Mean RMSE (N/m)		
Amplitude (m)	**WEC Motion**	**Heave**	**Surge**	**Sway**
30mm	**Heave**	4.721	1.903	2.501
	Surge	1.543	3.560	4.200
40mm	**Heave**	5.019	1.709	2.908
	Surge	1.484	3.971	4.291
50mm	**Heave**	5.309	2.058	2.054
	Surge	1.216	4.872	4.423